國立中山大學材料科學研究所

碩士論文

利用磁控濺鍍合成鎂銅金屬薄膜及其特性分析

Preparation and Characterization of Mg-Cu Binary Metallic Thin Film

研究生：周鴻昇 撰

指導教授：黃志青 博士

中華民國 九十六 年 六 月

Content

Tables List

Figures List

Abstract

In this study, Mg-Cu thin film metallic thin films were fabricated via two ways, the co-deposition and post-annealing of the multilayered thin films. Amorphous $Mg_{1-x}Cu_x$, where x is from 38 to 82, thin films with nanocrystalline particles are able to be fabricated via co-sputtering. The mechanism of formation is different from the rapid quenching process.

For the Mg-Cu co-sputtering system, the mechanical properties of the Mg-Cu co-sputtered films were tested via MTS nanoindenter. $Mg_{23.5}Cu_{76.5}$ exhibits a higher Young's modulus than $Mg_{17.7}Cu_{82.3}$ and $Mg_{40.4}Cu_{59.6}$ due to the partial amorphous structure. Moreover, the pop-in effects with a smaller size occurs of the $Mg_{23.5}Cu_{76.5}$ sample in a higher frequency than of the $Mg_{17.7}Cu_{82.3}$ and $Mg_{40.4}Cu_{59.6}$ samples. The small pop-in effects in the $Mg_{23.5}Cu_{76.5}$ sample approximate match the width of amorphous matrix via the HRTEM observation.

Another process to form the amorphous thin film is via the post isothermal annealing process of the multilayered thin films. However, for the specimens of 20T32 consisting of 150-nm Mg and 50-nm Cu individual layers, the Mg individual layers would react to the Cu individual layers during the annealing at a temperature of 413 K owning to the slight negative heat of mixing. Due to the localized diffusion near the interfaces, Mg_2Cu gradually form during the isothermal annealing since Mg_2Cu is the most stable phase below 548 K [62]. Localized interdiffusion near the interfaces between Mg and Cu individual layers induced the formation of Mg_2Cu rapidly. For the 40T32 specimens consisting of 15 nm Mg and 5 nm Cu individual layers, Mg_2Cu rapidly form at 413 K due to the high interface energy. Then, the similar result exhibits in the 20T14 and 40T14 specimens annealed at 363 K.

摘要

近幾十年來，具有獨特的物理特性及化學特性之非晶質合金受到眾多學者的研究及探討。目前合成非晶質合金的方法為常見的為由液相至固相之液態激冷法。在 2000 年後，藉由物理氣相層積製備非晶質合金薄膜由於其應用潛力，因此越來越受到廣泛注意。

本實驗分別利用共濺鍍及多層膜兩種不同之製程來製備鎂銅金屬薄膜，接著再利用真空熱處理並藉由 XRD 觀察其結構之轉變。藉由 XRD 觀察可以發現，鎂銅共濺鍍薄膜，銅含量從 38~82 at%，呈現為奈米鎂銅介金屬化合物及鎂銅非晶質之奈米複材。在 423 K 真空熱處理後，發現其結晶相會隨著成分所在之共晶區域有所差異。在 $MgCu_2$-Cu 區域中，熱處理後以奈米 $MgCu_2$ 為主；在 Mg_2Cu-$MgCu_2$ 區域中則是以 Mg_2Cu 及 $MgCu_2$ 為主。然而，鎂銅多層膜中，在經由 413 K 熱處理後發現其結晶相與其成分無關，均為 Mg_2Cu，這是由於擴散僅發生在介面附近以及鎂銅之介金屬化合物在低溫時，其最穩定相為 Mg_2Cu。

在此研究中，發現僅有利用共濺鍍製程有可能形成鎂銅非晶質合金薄膜，接著利用奈米壓痕技術量測 $Mg_{17.7}Cu_{82.3}$, $Mg_{23.5}Cu_{76.5}$, 及 $Mg_{40.4}Cu_{59.6}$ 之楊氏模數及硬度，可以發現到 $Mg_{23.5}Cu_{76.5}$ 具有最高之楊氏模數及硬度為 118 GPa 及 4.6 GPa，再利用 TEM 觀察 $Mg_{23.5}Cu_{76.5}$ 共濺鍍薄膜，發現到其微結構呈現以 $MgCu_2$ 為強化相之鎂銅非晶質合金複材，因而表現出較高之楊氏模數及硬度。

Chapter 1   Introduction

1-1   Amorphous metallic alloys

The amorphous metallic alloy is a disordered material without the periodicity of crystalline structure. The structure of amorphous metallic alloys displays as a random structure which consists of a short-range order structure in contrast to the structure of crystalline materials which show a long-range order in repeating unit cells, as shown in Figure 1-1 [1]. In fact, the random atomic arrangement of the amorphous alloy is not completely disordered but exists a short-range order in a very small localized area, as shown in Figure 1-2 [1]. According to the appearance and thermodynamic characteristics of these materials, amorphous metallic alloys are also called as liquid metals, glassy metals, non-crystalline metals, or metallic glasses.

As people know, the rapidly quenching method from the liquid to solid phase is the most popular way to synthesize amorphous alloys in forms of ribbons, bulks, or powders. This principle is based on the solidification through a sufficiently high cooling rate in order to prevent from crystalline-phase nucleation. At the initial stage, it is considerably difficult to reach such a high cooling rate about 10^7 K/s. However, a better method that can reduces effectively the critical cooling rate (lower than 10^3 K/s) to fabricate bulk metallic glasses was discovered during 1980s by adding the third element into the original binary system. The amorphous alloys are very suitable for the increased demand to resist the severe environmental situations because of their particular properties.

The disordered structure is different from the crystalline structure with the same construction in repeating unit cell. The interval between atoms to each other is called the free volume. Due to a large mount of free volume in the disordered structure, amorphous alloys exhibit the shear band deformation mechanism, lower Young's modulus, higher tensile strength, higher electric resistance, and excellent gas absorption ability, etc.

Recently, in order to achieve the ultimate goal of the light and tough engineering application, the amorphous alloy is considered to be a potential material. Inoue's group [2] produced ternary and multi-component bulk metallic glasses for functional applications, such as protective coating. The outshape of Vertu, the famous cellphone of Nokia, is coated by liquid-metal alloys, as shown in Figure 1-3 [3]. Owing to the trend of microminiaturization in the electronic industry, high strength and tough thin films metallic glasses with an excellent superplastic formation ability are very suitable for the enclosures of electrical parts. Up to now, the Pd-based and Zr-based metallic glass thin film is developed as a microactuator and nanopatterning, as shown in Figures 1-4 [4] and 1-5 [5], respectively. The functional properties and application fields are listed in Table 1-1 [6].

1-2 Characteristics of bulk metallic glasses (BMGs) and thin film metallic glass (TFMGs)

During the last decade, bulk metallic glasses (BMGs) were developed popularly. Because metallic glasses exhibit many properties different from crystalline metals, research fields were focused on the fabrication of metallic glasses, as well as the rheological behavior, mechanical, thermodynamic, thermal, electric and magnetic properties, especially for the fabrication and mechanical properties. BMGs exhibit many excellent advantages for engineering applications, such as a high elastic energy, a high yield strength, a small elastic limit, a low Young's modulus, as well as good wear and corrosion resistances.

Besides, many metallic glasses have a large supercooled liquid region with the crystallization resistance. It implies BMGs have an excellent superplastic formation ability. However, the biggest problem of the fabrication in using the rapidly quenching method is to achieve an enough cooling rate (higher than 10^6 K/s). However, Inoue [6] announced the empirical rules for the synthesis of amorphous alloys:

(1) Multicomponent systems consisting of more than three elements,
(2) Significant difference in atomic size ratios above 12% among the three main constituent elements,
(3) Negative heats of mixing among the three main constituent elements.

The third element replacement for partial or complete substitution by Gd, Ni, or Y in the Mg-Cu system is an important and valid way to solve the problem in fabrication and the diameter enlargement of BMGs [2,7]. In addition to the advantages mentioned above, adding the third or more elements into an alloy system is able to adjust the properties of BMGs for some particular applications.

It is well known that the thin film technology is widely applied in the development of the semiconductor industry. According to the types of interfaces, the five main interfaces and interface reactions (IRs) pointed by Zhu et al. [8] play important roles in this field. They are listed below:

(1) Oxide/silicon interfaces － metal-oxide-semiconductor (CMOS),
(2) Oxide/metal interfaces － gas sensor and giant magnetoresistence spin valve.
(3) Metal/metal interfaces － magnetic storage media,
(4) Metal/semiconductor interface － metal-semiconductor field-effect transistor,

(5) Semiconductor/semiconductor interface — short-wavelength laser diode.

In the films with several micrometers even nanometers in thickness, the interface reactions become very important in the thin-film field. To utilize interface reactions is able to produce different kinds of intermediate layers, such as the diffusion barrier. However, since thin film metallic glasses were discovered from 1950s, a lot of related properties were researched extensively.

Compared with TFMGs, the rapidly quenching method for bulk or ribbon of metallic glasses is mainly limited to the intrinsic nature of materials and the cooling rate in process. Sputter and evaporation are the main methods for the fabrication of TFMGs. Two main ways for the fabrication of TFMGs are listed below:

(1) Direct methods: co-sputtering and alloy sputtering,

(2) Indirect methods: annealing-induced and stress-induced amorphization.

The direct methods are similar to the liquid quenching method for BMGs. In the co-deposition process, the TFMGs would be fabricated with an enough fast cooling rate (above 10^8 K/s), such as the success for the binary Al-Fe [9] and Au-La [10] systems. However, TFMGs can be produced in using the alloy deposition technique with a lower cooling rate by adding the third or more elements. The Zr-Cu-Al [11], Zr-Cu-Al-Ni [12] and Pd-Cu-Si [13] TFMGs are successful cases in using the alloy sputter process. The annealing-induced process is a potential method for a large mount of the continuous fabrication with lower cost and high reliability. Although the stress-induced phase transformation (amorphization) is a well-known way for the modification of materials, the mechanism and phenomena will not be discussed particularly because this is not the emphasis of this study.

As mentioned above, the composition and microstructure of the films can be well controlled for any shape materials. Furthermore, the surface modification used by the metallic glass coating is able to adjust the properties of the substrate and promote the smooth and shiny surface, even enhance the mechanical, thermal, and electrical properties. An intermediate layer between a film and substrate frequently forms after a post-treatment, such as annealing and plastic deformation. The intermediate layer usually forms and exhibits completely different nature from the film and substrate, such as the Fe-Hf system as shown in Figure 1-6 [14].

1-3 The development of Mg-based thin film

Mg-based thin films, such as $MgCl_2$, magnesia (magnesium oxide), MgF_2, and MgB_2, were studied popularly since 1980s. At the early stage of the development, most Mg-based thin films were synthesized by the chemical vapor deposition technique and the sol-gel method. In 1995, Magni and Somorjai [15] synthesized the magnesium chloride thin film which has widely been used as the Ziegler-Natta catalyst by chemical vapor deposition (CVD) in order to speed up the polymerization. Because the film exhibits good refractoriness, good corrosion resistance, high thermal conductivity, low electrical conductivity, and transparency to infrared, the magnesia thin film has been synthesized widely by the same method [16] and used as microelectronic devices, such as piezoelectric micro-actuators and sensors [17].

MgF_2, another magnesium halide compound, and magnesia exhibit high transparency, low refractoriness, chemical and mechanical durability, so it has been used as the anti-reflective coating on glass. Recently, the physical vapor deposition technologies, like the sputter, evaporation, and pulsed laser deposition (PLD) techniques may be used to fabricate MgO [17], MgB_2 [18], Pd-Mg [19,20,21] thin films.

Some magnesium alloys, such as pure magnesium, the Ln-Mg (La or Ce) alloys and the Mg-Ni metallic glass, were reported as suitable hydrogen-storage materials reported in a lot of references [22,23]. However, characteristics of Pd-Mg thin films have been popularly noticed. Higuchi et al. [20,21] reported a high-performance hydrogen-storage Pd-Mg alloys for future clean systems. Although the hydrogen-storage ability of magnesium is excellent, the high desorption temperature may decrease the value in its application. They introduced different thicknesses of the Pd layer with the opposite properties to magnesium in order to adjust the hydriding-dehydriding property.

Owing to the introduction of the Pd layer, the Pd-Mg thin film can not only store a large mount of hydrogen but also release them easily. In 2002, the tri-layer Pd-Mg-Pd thin film was fabricated. The tri-layer structure can control the hydriding/dehydriding property more and more easily.

1-4 The propose and motive of this research

The metallic glass is a potential material for the micro-electro-mechanical systems (MEMs) and other applications for some functional purposes, such as good wear and corrosion resistance, high hydrogen-storage ability, and antibiotic coating, etc. Inoue [7] have reported various BMG systems, such as Fe-, Co-, Zr-, Pd-, and Mg-based systems, and their applications since 1980. Reducing the critical cooling rate by the addition of alloy elements is able to modify the thermal, mechanical, electric or magnetic properties. Though BMGs have excellent properties, they might be hard to be made as micro- or even nano-components in MEMs. The thin-film technique for MEMs has been used in metallic glasses since 1980s. The large-area thin films with uniform-distribution of the composition and the structure are able to be fabricated. There are two kinds of thin films listed below:

(1) Bi- or multi-component monolayer thin film metallic glasses,

(2) Bi- or multi-component multilayer thin film.

In this study, the above two kinds of Mg-Cu metallic thin films are fabricated by the magnetron sputter deposition and post-thermal treatment. The first method is to utilize the co-sputtering technique to fabricate the Mg-Cu monolayer thin film metallic glasses. The second is to fabricate the Mg-Cu multilayer thin film and induce the amorphization by annealing.

It is intended to investigate the amorphization nature and mechanism, caused by interdiffusion through an annealing process at different temperatures. The microstructure, thermal, and mechanical properties of the resulting thin films will be examined.

Chapter 2 Background and Literature Review

2-1 Evolution of amorphous alloys

During 1960s, Klement et al. [24] developed firstly the splat quenching method to fabricate the Au-Si amorphous alloy in avoiding crystallization during solidification. Owing to the unique characteristics of the amorphous structure, this method generated wide interests of the new type alloy among scientists and engineers. In 1969, Chen and Turnbull [25] successfully synthesized an amorphous alloy of the Pd-Si-X (X=Ag, Cu or Au) ternary system. A few years later, Chen [26] fabricated the Pd-T-Si (T= Ni, Co or Fe) ternary amorphous alloy in using the die casting and roller-quenching method, and the maximum diameter of BMGs was 1 mm. They also analyzed effects of the alloy systems and compositions by the thermodynamic calculation. According to this report, as the replacement atoms increased, the arrangement of atoms was more random. The glassy metal was more easily to form.

Other potential processes for fabrication were published since early 1980s. In 1983, Schwarz and Johnson [10] fabricated first the La-Au TFMG by the solid-state reaction. Furthermore, he found the broad hump from 25^o to 45^o by X-ray diffraction (XRD) with Cu $K\alpha$ radiation, representing the formation of amorphous structure. After 1983, more alloy systems were fabricated by evaporation and sputtering. In 1986, Cotts et al. [27] successfully fabricated the Ni-Zr multilayer thin films by the magnetron sputter method, and observed the amorphization of crystalline metallic thin film by differential scanning calorimetry (DSC) at a constant temperature scanning rate of 10 K/min. The formation of amorphous phase means that it is the intermediate state from crystalline phase to intermetallic compound. In the beginning of 1980s, Kui et al. [28] produced firstly the Pd-Ni-P bulk metallic glass with 5 mm diameter by the heating and cooling cycle. They used this method which may decrease the homogeneous and heterogeneous crystalline nucleation rate, and successfully improved the BMG maximum diameter from 5 mm to 10 mm by processing the Pd–Ni–P melt in a boron oxide flux.

Chen et al. [29] rapidly fabricated the Al-Fe, Bi-Fe and Bi-Ti binary thin films in 1988. The thin film was quenched by liquid nitrogen while gas atoms were deposited on the NaCl substrate by evaporation or sputtering.

In the late 1980s, Inoue's group [7] in Tohoku University of Japan developed many new multicomponent metallic glass systems with the lower cooling rate in Mg-, Ln-, Zr-, Fe-, Pd-, Cu-, Ti- and Ni- based systems. Amorphous alloys started to be popularly noted due to their particular properties which can be applied to MEMs parts, hydrogen storage medium, and etc. In 1996, Dudonis et al. [30] produced the amorphous Zr-Cu TFMGs by co-sputtering. They first discussed the relation among deposition factors such as the working gas pressure, the substrate temperature and the microstructure of deposited thin films.

Near 2000, Akira's group [11,13] at Precision and Intelligence Lab developed Zr-Cu-Al and Pd-Cu-Si ternary TFMGs, fabricated by alloy sputter deposition, for MEMs application. Because of a large supercooled region, excellent three-dimension forming ability, good corrosion resistance and mechanical properties, the Zr- and Pd- based TFMG is an appropriate choice for the conical spring linear microactuator in MEMs. This report opened the TFMGs application in the micro-electro-mechanic industry.

Annealing-induced full amorphization in multi-component monolayer thin films was reported by Chu et al. [12] in 2004. The Zr-Al-Cu-Ni crystalline thin film was annealed under argon atmosphere at the heating rate of 40 K/min and the holding time of 60 s at the temperatures range from 550 to 950 K. The crystalline phase transferred to the meta-stable amorphous phase due to the atomic interdiffusion. Compared with direct fabrication methods of TFMGs, this method can save much energy and cost because this method does not need to maintain the very low temperature of the substrate. Thus, the post-treatment methods to fabricate TFMGs are potential processes with the convenience and low cost.

After one year, Inoue's group [4] fabricated the nano-device by the nano-scale pattering technique. The Zr-Al-Cu-Ni TFMGs were deposited by magnetron sputtering. The nano-pattern on Zr-based TFMGs was produced by the focus ion beam (FIB) technology. This nano-pattering technology may be applied to fabrication of nano-mold and high-density memories.

Many researchers have reported evolution and improvement of TFMGs fabrication by a wide margin since 1960s. Because of the application of TFMGs in MEMs, several important properties, such as the electric resistance [31], hardness [32], fracture phenomena [33], reliability [34] and mechanical properties [13,35], were noticed and researched. Due to the absence of defects, the size effect is the major factor which leads to different properties between bulk and thin-film specimens. When the dimension of a crystalline material becomes as small as they can in MEMs, the intrinsic length scales, such as a grain size and dislocation structure, are no longer small in comparison with the geometric dimensions of the material, which can cause reliability problems of the microcomponents. The research of Zhang et al. [36] reported the deformation behavior of free-standing Pd-based TFMGs in 2005. As the results of the bending test, as-deposited films revealed ductility due to the existence of shear

Bands. After annealing, ductility might transfer to the brittleness because of the absence of shear bands.

In conclusion, it is ready to enter a more mature stage since amorphous alloys started to develop in 1960. Multi-component bulk metallic glasses produced by Inoue's group in using the liquid-quench method have excellent mechanical properties, the superplastic formation ability and thermal stability. Due to these advantages, amorphous alloys can be used in bulk application easily. The outer shape of amorphous alloys is able to strength the resistance to severe circumstance. However, amorphous alloys made by deposition techniques are the potential materials as MEMs parts because it is fast, low-cost, and very easily to control the composition and morphology. Furthermore, all kinds and shapes of materials are easily to be coated with an amorphous thin layer for improvement of properties.

2-2 Systems of amorphous alloys

Up to now, many systems of amorphous alloys were discovered. Systems of amorphous alloys can be roughly divided into non-ferrous and ferrous alloy systems since 1980s. Table 2-1 [7] summarized the types of amorphous alloys. The non-ferrous systems are Mg-Ln-M (Ln = Lanthanide metal, M = Ni, Cu or Zn), Zr-Al-TM (TM = VI-VIII group transition metal), Zr-Al-TM, Zr-Ti-Al-TM, Ti-Zr-TM, Zr-Ti-TM-Be, Zr-(Nb, Pd)-Al-TM, Pd-Cu-Ni-P, Pd-Fe-Ni-P, Ti-Zr-Ni-Cu-Sn and Ti-Zr-Ni-Cu-(Si, B) systems. However, the ferrous alloy systems include Fe-(Al, Ga)-metalloid, (Fe, Co, Ni)-(Zr, Hf, Nb)-B, Fe-Co-Ln-B, Ni-Ti-P and Ni-Nb-(Cr,Mo)-(P, B) systems. The ferrous alloy systems have been developed during the last four years after the synthesis of the nonferrous alloy systems [7].

According to the features of the alloy components, systems of amorphous alloys are divided into five groups listed in Table 2-2 [7]. The first group consists of ETM, IVB ~ VIB group transition metal, (or Ln), Al and LTM, VIIB ~ VIIIB group transition metal, such as Zr-Al-Ni. The second group is composed of LTM, ETM and metalloid as indicated by Fe-Zr-B. The third group is LTM (Fe)-(Al, Ga)-metalloid systems. The fourth group is indicated to Mg-Ln-LTM and ETM (Zr, Ti)-Be-LTM system. The fifth system is composed only of two kinds of group element (LTM and metalloid), such as Pd-Cu-Ni-P.

When the fabrication techniques for bulk metallic glasses were widely developed, thin film metallic glasses produced by gas deposition processes were noted as another potential material for MEMs. Thin film metallic glasses are usually divided to bi- or multi-component monolayer thin films, and bi- or multi- component multilayer thin films.

Physics researchers utilized binary metallic thin films to analyze the phase transformation between the crystalline, intermetallic and amorphous phases [27,37] and diffusivities in amorphous alloys [38] in 1980s. Many references reported the phenomena of amorphization through different solid-state reactions. It is particularly noted that the report of Newcomb and Tu [39] which shows the Ni-Zr bilayer thin film by sputter deposition exhibited the amorphization after annealing. However, Liu's group [40] in Beijing Tsinghua University published a review paper in 1987 which is concerned with the binary systems of thin films by the ion mixing process. At least 54 alloy systems were found over the latest ten years, which is listed in Table 2-3 [40].

According to previous researches, binary equilibrium phase diagrams were usually used to predict the conditions under which the glassy phase can be formed. The formation enthalpy (H_f) and the alloy compositions are the two important parameters in consideration, reported by Liu [40]. Many systems with large negative H_f values frequently have a broad two-phase region and/or complicated intermetallic compounds. It may imply that systems with negative H_f might form amorphous phase easier.

There are two types of the binary alloy systems. The first type of the binary systems has a negative value of H_f. Al-X (X=Au, Co, Fe, Mn, Mo, Nb, Ni, Pd, Pt, Ta, and Ti), Au-X (X=Co, Fe, Ni, Ru, and W), Co-X (X=Gd, Mo, Nb, Tb, Ti, and Zr), Fe-X (X=Gd, Mo, Nd, Tb, Ti, W, and Zr) systems belong to this type. However, Another type with positive value of H_f reveals instability of amorphous phase implying the difficulty of the amorphous phase formation. Au-X (X=Co, Ru, Ti, and W), Ag-X (X=Co, Cr, Cu, Nb, and Ni), Cu-X (X=Cr, Fe, Os, Ta, and W) belong to this type. This empirical rule can roughly predict the formation of the amorphous phase or not.

At the same time of the expansion in the bulk metallic glass, Akira's group [11] reported the synthesis of Zr-Cu-Al and Pd-Cu-Si systems of multi-component monolayer TFMGs and its applications as microactuator near 2000. Until now, new binary alloy system are still found, such as the Zr-Ta [41], Ni-Mn [42] and Au-Cu [32] systems.

2-3 Evolution of fabrication methods for amorphous alloys

Fabrication processes of metallic glasses may be divided into three types of reactions:

(1) Solid-solid reaction which occurs only in solid phase: ion implantation, ion beam mixing, mechanical alloying (MA), accumulative roll bonding (ARB), and annealing,

(2) Liquid-solid reaction which occurs from liquid to solid phase: splat quenching, chill block melt spinning (CBMS), planar flow casting (PFC), spray forming, conventional metallic mold casting, and high pressure die casting,

(3) Gas-solid reaction which is from gas to solid phase: sputter and evaporation deposition [43].

Generally speaking, it is easily to form amorphous alloy through the rapidly quenching methods, such as the melting spinning, and sputter deposition. The sputter deposition process is strongly involved in the phase transition from gas to solid. However, many researches reveal that it is possible to form amorphous thin film by controlling the factors in the deposition process or post-treatment.

As noted, the production of amorphous films requires very high deposition rates and low substrate temperatures, usually below their crystallization temperatures. A low temperature can freeze the atoms on the substrate and prevent them from diffusing into equilibrium lattice sites. In order to reach a sufficient cooling rate, liquid nitrogen or helium is usually used. By mid-1950s, Buckel [44] fabricated amorphous films of pure metals, such as Ga and Bi, by thermal evaporation onto the substrate maintained at the liquid helium temperature with the fast cooling rate above 10^{10} K/s. Because the cooling rate was too hard to reach, other methods, which form metallic glasses more easily such as liquid quenching, gradually became popular after 1960s.

The splat quenching method was first announced by Klement et al. [24] in order to raise the cooling rate, as shown in Figure 2-1 [43]. An amorphous irregular die (area ~ 0.2 mm^2; thickness ~ 10 μm) can be fabricated under the cooling rate (~10^6 to 10^{10} K/s). Figure 2-2 [43] shows the two roller quenching method announced by Chen and Miller in 1970. This method broke the limitation of amorphous alloys. Hence, it caused wide attention because uniform long ribbons (width ~ 2 mm; thickness ~ 50 μm) can be fabricated continuously by this method. This method brought a wide tide to raise the cooling rate for fabrications of more tough, and light amorphous alloys.

However, the chill block melt-spinning process developed by Liebermann et al. in 1976 is to quench the melt jet on a high-speed rotating substrate wheel by inert gas, as shown in Figure 2-3 [43]. This method can largely promote the stability and quality of fabrication processes. Until now, other liquid quenching methods, such as the plannar flow casting process, are based on CBMS concept, as shown in Figure 2-4 [43].

Before 1980, the fabrication methods emphasize on how to increase the cooling rate in avoiding formation of the crystalline phase. However, Inoue et al. [2] develop the Mg-based ternary amorphous alloy by the copper mold casting method in 1991. Bulk metallic glasses of Mg-Cu-Y with 4 mm diameter were successfully synthesized. Addition of the third kind element cooperating with liquid quenching can effectively reduce the critical cooling rate (lower than 10^2 K/s). In 1992 [45], they successfully fabricate bulk metallic glasses with 7 mm in diameter by the high pressure die casting method.

The gas-solid reactions to form metallic glasses are well known as gas deposition techniques. The multi-component monolayer TFMGs can be fabricated by two methods: (1) co-sputter deposition process, and (2) alloy sputter deposition process, reported by Dudonis et al. [30] and Hata et al. [11], respectively. It is completely discussed in the later section 2-6.

2-4 Glass-forming ability (GFA)

As people know, the metallic glass can be synthesized by many methods, like ion beam mixing, melting spinning, die casting, and sputtering, etc. Since the first amorphous alloy fabricated in 1960, lots of alloy systems were reported by many researches. Due to the complication of multi-component alloy systems, many criteria were announced to assume the glass-forming ability (GFA) thermal stability. By using these criteria, the design of alloy system, and evaluation and prediction of properties can become easier, effective, and more economic. Three criteria were reported:

(1) Supercooled liquid range, ΔT_x (= T_x - T_g, where T_x and T_g are the onset crystallization temperature and the glass transition temperature, respectively) [45],

(2) Reduced glass transition temperature, T_{rg} (= T_g /T_l, where T_l is the liquidus temperature) [46],

(3) γ (= $T_x/(T_g + T_l)$) [47].

First, ΔT_x is the initial criterion of GFA and popularly used as an index of the thermal stability. During a supercooled liquid range, as shown in Figure 2-5 [47], amorphous alloys exhibit the nature of ideal Newtonian fluid which is very suitable for forming. The large ΔT_x value indicates that the disordered structure can exist in a wide temperature range without crystallization. This implied the resistance for crystallization and growth of crystalline phase [48]. However, ΔT_x is a rough parameter which does not consider any crystallization mechanism during cooling and heating process. Second, ratio of T_g/T_l was introduced for pure kinetic reactions associated with the need to avoid crystallization. T_{rg} (= T_g /T_l) is typically assumed to be less dependent on compositions, while T_l often decreases more strongly. The interval between T_l and T_g thus generally decreases and the value of T_{rg} increases with increasing alloying concentration so that the probability of being able to cool through this ‘dangerous’ range without crystallization is enhanced.

Therefore, a new parameter γ based on $T_x/(T_g + T_l)$ was announced by Lu and Liu [47] in 2002. As Lu and Liu mentioned in the article, γ is more suitable and accurate to evaluate glass-forming abilities of alloy systems because of completely consideration of thermal stability and resistance to crystalline, as shown in Figure 2-6 [49]. Besides, it also has a relation with the critical cooling rate (R_c) and critical specimen thickness (Z_c), and the relationship has been formulated as follows:

$$R_c = 5.1 \times 10^{21} \exp(-117.19\gamma), \tag{2-1}$$

$$Z_c = 2.80 \times 10^{-7} \exp(41.70\gamma). \tag{2-2}$$

2-5 Theory and phenomena of sputter deposition process

2-5-1 Introduction of sputtering

The sputter deposition, a physical fabrication process of thin films, utilizes ion bombardment and momentum transfer. The incident particles impact the surface or near-surface atoms of a target with enough energy which can break bonds and dislodge atoms by the bias between the anode and cathode. During this process, the collision between incident particles and atoms of a target can be viewed as elastic collision because the loss of momentum transfer is nearly zero. Sputtering occurs whenever any particle strikes a surface with enough energy to dislodge an atom from surface. The sputter yield is just the ratio of the number of emitted particles per incident particle [50]:

$$Y = (\text{\# of emitter particles/ \# of incident particles}). \tag{2-3}$$

Sputtering can occur for virtually all incident species, including atoms, ions, electrons, photons, and neutrons as well as molecules and molecule ions. Generally speaking, the plasma includes inert gas ions, such as Ar^+, Kr^+, or small molecule ions such as N_2^+, O_2^+, etc.

Sputter yield is independent on the particle charge but is dependent on the physical momentum transfer and kinetic energy from incident the particles to surface atoms.

When energetic particles bombard on the target, many reactions occur between the ionized gas particles and target atoms near the surface, as shown in Figure 2-7 [51]. Most of the transferred energy (>95 %) appear as heat in the surface region and near-surface region. Some of the bombarding particles are reflected as high energy neutrals and some are implanted into the surface. When an atomic sized energetic particle impinges on a surface, the particle bombardment effects can be classed as:

(1) Prompt effects ($<10^{-12}$ s) – lattice collisions, physical sputtering, reflection from the surface,

(2) Cooling effects ($>10^{-12}$ s to 10^{-10} s) – thermal spikes along collision cascades,

(3) Delayed effects ($>10^{-10}$ s to years) – diffusion, strain-induced diffusion and segregation,

(4) Persistent effects – gas incorporation compressive stress due to recoil implantation.

Incident particles, also called as plasma, are produced by glow discharge. In the ultra-high vacuum chamber, dilute gas, such as argon, is introduced into the chamber. Gas molecules can be ionized when the bias between cathode and anode is large enough. At this moment, argon atoms are divided to Ar^+ ions and electrons. Electrons produced at the initial of glow discharge are called primary electrons. However, plasma can not exist stably due to the unstable primary electron source. Actually, the stable plasma is maintained by stable secondary electrons source which are produced near the target surface by the collision between the ions and target atoms.

At the beginning of the discharge, the primary electrons from the cathode are accelerated by the electric field near the cathode to the anode. These energetic electrons collide with the gas molecules and generate positive ions before they travel to the anode. The positive ions bombard the cathode surface, which result in the generation of secondary electrons from the cathode surface. The secondary electrons increase the ionization of the gas molecules and generate a self-sustained discharge [52]. The advantages for sputter deposition include:

(1) Excellent film uniformity, particularly over large areas,

(2) Easy control of surface smoothness and uniform of films,

(3) Deposition of films with nearly bulk-like properties, which are predictable and stable,

(4) The sputtering deposition is essentially a kinetic process involving momentum exchange rather than a chemical and/or thermal process. Therefore, virtually any material can be introduced into a gas discharge or sputtered from solid,

(5) Good adhesion of films,

(6) Sputtering allows for the deposition of the films having the same composition as the target source.

2-5-2 Systems of sputter deposition process

According to types of power supply, systems of sputter deposition processes can be divided to four types: (1) direct current (DC) diode sputtering system, (2) radio frequency (RF) diode sputtering system, (3) magnetron sputtering, and (4) reactive sputtering.

The DC diode sputtering system is the simplest type of sputtering. Figure 2-8 [53] shows a pair of planar electrodes in a vacuum chamber. One electrode is a cold cathode, and the other is an anode. Glow discharge can occur with enough bias voltage. The top plasma-facing surface of the cathode is covered with a target material and the reverse side is water-cooled. The substrates are placed on the anode. After the glow discharge starts, Ar ions in the glow discharge are accelerated at the cathode fall and bombard the target resulting in the deposition of the film on the substrates. Near the cathode is a dark space or sheath in which may collect large mounts of primary and secondary electrons. The RF diode sputtering system is very similar to the DC sputtering system, but differ from power supply, as shown in Figure 2-9 [53]. The DC system is suitable for conductor targets, such as Fe, Cu, Zr, Ni, and Mg.

By substitution of an insulator target for a metal target in a DC diode sputtering system, the sputtering glow discharge can not be sustained because of the build-up of a surface charge of positive ions on the front side of the insulator target. To solve this problem, the RF power supply is substituted for the DC power supply. For a small part of the RF cycle, the cathode and anode are electrically reversed. This can eliminate the build-up charge on an insulating surface by providing equal number of ions, electrons, ions, and so on. The RF power supply is operated at high frequency about from 60 MHz to 80 MHz. However, the most common frequency is 13.56 MHz and its multiples (2× or 3×) [50].

A second key advantage of the RF diode system is that the oscillation of field in the plasma (at the driving frequency) resulting in additional electron motion with the plasma. This has been described in several ways, but the most interesting point is an analogy to the electron ”surfing” on the electric field waves in the plasma. The end result of this enhanced electron movement is that the probability of an ionizing collision is increased for a given secondary electron, and this results in an increase in the plasma density compared to DC diode. The density increase results in higher ion currents and a faster sputtering rate.

Although DC and RF sputter deposition process is a convenient, high reliability and continuous process, a slow deposition rate and charging are still the major disadvantages of these processes. In 1935, Penning’s study [52] first revealed the low pressure sputtering under a transverse magnetic field which was added on a DC glow discharge tube. A magnetron uses a static magnetic field configured at the cathode location, as shown in Figure 2-10 [53]. The magnetic field is located parallel to the cathode surface, as shown in Figure 2-11 [50]. Secondary electrons emitted from the cathode due to ion bombardment are constrained by this magnetic field to move in a direction perpendicular to both the electric field (normal to the surface) and the magnetic field. Figure 2-12 [50] shows an E×B drift, which is based on Hall Effect. This drift causes electrons to move parallel to the cathode surface in a direction 90 degree away from the magnetic field.

Basing on these issues mentioned, an additional magnetic field added can prolong the electron retaining time in the plasma and improve the probability of collisions. This enhances the efficiency of the simple diode sputtering, and also makes diode sputtering configuration operate under higher currents and pressures.

In reactive sputtering, thin films of compounds are deposited on substrates by the sputter deposition from metallic targets which react with reactive gas, such as oxygen, nitrogen with inert gas (invariably Ar). The types of compounds synthesized by reactive sputtering are oxides, nitrides, carbides, sulfides, and are briefly listed below [54]:

(1) Oxides (oxygen) – Al_2O_3, In_2O_3, SnO_2, SiO_2, and Ta_2O_5,

(2) Nitrides (nitrogen, ammonia) – TaN, TiN, AlN, and Si_3N_4,

(3) Carbides (methane, acetylene, propane) – TiC, WC, and SiC,

(4) Sulfides (H_2S) – CdS, CuS, and ZnS,

(5) Oxycarbides and oxynitrides of Ti, Ta, Al, and Si.

2-5-3 Thin film growth mechanism

The formation of thin films synthesized by the sputtering deposition process is related to gas-solid phase transformation which contains three stages:

(1) Nucleation,

(2) Growth,

(3) Coalescence.

At the initial stage of formation, energetic vapor atoms have some probability to condense on the substrate by forming bondings between vapor atoms and the substrate. An embryo composed of several adatoms forms on the substrate owing to stable bondings between atoms and the substrate. Based on thermodynamic theories, the form of embryos is usually assumed as sphere shape. Embryos with smaller than the critical size (r^*) are unstable and they may maintain the unstable situation or re-evaporation. Contrarily, embryos can transfer to stable nuclei while the size of embryos is larger than r^*. At this stage, nucleation is the main reaction, so this stage is also called the nucleation stage. The nucleation rate ($\dot{N}$) can be obtained by some thermodynamic calculations and simplification, as in the following equation:

$$\dot{N} = 2\pi r^* a_0 \sin\theta \frac{PN_A}{\sqrt{2\pi MRT}} N_s \exp\frac{E_{des} - E_s - \Delta G^*}{kT}. \tag{2-4}$$

The quantities N_s, E_{des}, E_s and, ΔG^* represent the total nucleation site density, the energy required to desorb it back into the vapor, the activation energy for surface diffusion, and critical free energy of nucleation, respectively.

After the nucleation stage, nuclei growth becomes the main reaction, which is called the growth stage. When a surface density of nuclei reaches a saturated situation, nuclei do not form any more but start to grow up. In fact, there is no clear demarcation between the end of nucleation and the onset of growth. In this stage the prior nuclei incorporate impinging atoms and subcritical clusters, and then grow in size while the island density saturates rapidly. Many observation have pointed to three basic growth modes, as shown in Figure 2-13 [52]:

(1) Island (or Volmer-Weber) mode,

(2) Layer (or Frank-van der Merwe) mode,

(3) Stranski-Krastanov mode.

The island growth occurs when the smallest stable clusters nucleate on the substrate and grow in three dimensions to form the inlands. This happens when bondings between molecules each other are more stable than those between molecules and the substrate. Some systems of metals on insulators, alkali halide, graphite, and mica substrates exhibit this mode of growth.

The layer growth is the opposite type to the island type. The extension of the smallest stable nuclei occurs overwhelmingly in two dimensions resulting in the formation of planar sheets. In this mode, the adatoms tend to form bonds with the substrate more likely than with each other. The most important example of the mode involves the single-crystal epitaxial growth of semiconductor films.

The layer plus island or Stranski-Krastanov (S.K.) growth mechanism is an intermediate combination of the aforementioned modes. In this case, after forming one or more monolayers, the subsequent layer growth becomes unfavorable. Although the transition from the two- or three- dimensional growth is not completely understood, the guessable cause that disturbs might be the binding energy characteristic of layer growth. The growth mode is fairly common and has been observed in metal-metal and metal-semiconductor systems.

At the last stage of thin film formation, it is called coalescence containing three basic mechanisms, as shown in Figure 2-14 [52]:

(1) Ostwald ripening,

(2) Sintering,

(3) Cluster migration.

Prior to coalescence there is a collection of islands with varied sizes and with time. The larger ones grow or “ripen” at the expense of the smaller ones, with the assumption of no contacts between islands each other. In order to minimize the free energy of the island structure, islands have a tendency to grow up or ripen by inter-diffusion.

The sintering mechanism is similar to the ripening mechanism but with the contacts between two islands. The driving force of this mechanism for neck growth is simply the natural tendency to reduce the total surface (or area) of the system. This results in the observed mass transport into the neck controlled by surface diffusion. It is clearly that diffusion is a thermally activated reaction. The adatoms with higher energy not only move from the target to the substrate, but diffuse on the substrate. Hence, the thin film has a smooth surface and fewer defects.

However, excess kinetic energy is not only provided by adatoms but also substrates. An insufficient temperature can not support overall adatoms or clusters to migrate but a part of the adatoms to diffuse around to near islands. Ostwald ripening and sintering mechanisms predominate over the coalescence stage under a lower temperature environment. Cluster migration, a high-temperature coalescence mechanism, occurs as a result of collisions between separate island-like crystallites (or droplets) as they execute random motion. Cluster migration has been directly observed in many systems, such as Ag and Au on MoS_2, Au and

Pd on MgO.

It is well known the three mechanisms play important roles in the formation of thin films. Different types of mechanisms can lead to different microstructures which would immediately affect the properties of thin films.

2-5-4 Zone model for sputtered coatings

As described above, the microstructure of thin films is a critical key for its mechanical, electric, thermal, and magnetic properties. Film growth, especially the nucleation stage, determines the film natures such as film density, surface area, surface morphology and grain size. Important aspects of the film growth are listed below:

(1) Angle-of-incidence of the adatom flux effects – geometrical shadowing,

(2) Ratio of deposition temperature (degrees K) to the melting temperature (degree K) of the film material (T/T_m),

(3) Energy released on condensation,

(4) Adatom surface mobility on surfaces and different crystallographic planes,

(5) Substrate surface roughness – initially and as the film develops,

(6) Deposition rate,

(7) Reaction and mass transport during deposition – segregation effects and void agglomeration,

(8) Mass transport and grain growth during deposition.

Figure 2-15 shows that different microstructures under different predominately processes, nearby, the shadow process, surface diffusion process, and bulk diffusion process. Thornton [51] integrated these microstructures and announced structure zone model (SZM) to describe the microstructure of sputtered and evaporated films, as shown in Figure 2-16.

Roughly speaking, the grain size varies with working gas pressure and T_s/T_m, where T_s and T_m are the temperature of the substrate and melting temperature of the film, respectively, as listed in Table 2-4 [51]. A low temperature or working pressure atmosphere would make thin films with Zone 1 structure but porous. In Zone 1, the surface diffusion is insufficient to overcome the geometrical shadowing by the surface features. In this situation, the film composing of tapered grains with a high surface area exhibits a mossy appearance. Since the growth is strictly a function of the surface geometry, angle-of-incidence and adatom surface mobility, amorphous as well as crystalline materials show the columnar growth mode.

In Zone 2, the growth in dominated by the adatom surface diffusion. In this region, the surface diffusion allows the densification of the intercolumnar boundaries. However, the basic columnar morphology remains. The grain size increases and the surface features tend to be faceted. In Zone T, the coating exhibits a fibrous morphology and is considered to be a transition from Zone 1 to Zone 2. The formation of the Zone T is due to the energetic bombardment from reflected high energy neutrals from the sputtering target at low gas pressures. In Zone 3, the bulk diffusion allows the recrystallization, grain growth and densification. Often each grain in Zone 3 can be considered as a single crystal in the highly modified columnar morphology.

2-6 Fabrication of TFMGs

In previous chapters, the fabrication methods have been discussed. In this portion, the topic focuses on evaporation and sputtering.

The gas-solid reactions to form metallic glasses are well known as gas deposition process. The bi- or multi-component monolayer TFMGs can be fabricated by two methods, listed below:

(1) Co-sputter deposition process,

(2) Alloy sputter deposition process.

In 1996, Dudonis et al. [30] successfully fabricated Zr_xCu_{1-x} TFMGs by the co-sputter deposition process. In their report, they discovered that the composition range of the formation is very wide ($x = 0.05 \sim 0.95$), and electrical conductance and reflectance vary with different compositions. Furthermore, Akira's group [11,55] in Precision and Intelligence Laboratory at Tokyo Institute of Technology reported the Zr-Cu-Al and Pd-Cu-Si TFMGs, which were directly produced by the alloy sputter deposition process near 2000. Zr-Cu-Al and Pd-Cu-Si alloy targets were fabricated by the arc melting process.

Phase transformation through thermal treatment is a popular method for particular properties such as diffusion barriers [56] and magnetic storage devices [57]. According to the idea of phase transformation, Chu et al. [12] announced a concept for the application of TFMGs, fabricated using annealing-induced full amorphization, to fabricate thin film metallic glasses. In the report, Zr-Cu-Al-Ni thin films were first deposited on the glass substrate. Then, the films were amorphized via low-temperature annealing.

The TEM image and the associated diffraction of the as-deposited film as shown in Figure 2-17 (a) [12], clearly indicate a typical sputtered nanocrystalline structure with a grain size of about 10~30 nm. After annealing at 650 K, the microstructure has transformed into a two-phase nanophase composite of an amorphous matrix containing uniformly dispersed nanocrystallines, as shown in Figure 2-17 (b). When the film was annealed at 750

K, about the onset of T_g, Figure 2-17 (c) indicates the amorphous matrix containing nanocrystalline phase. The uniform contrast TEM image, as shown in Figure 2-17 (d), suggests a fully amorphous structure formed at an annealing temperature of 800 K. However, Figure 2-17 (e) shows the crystalline phase formed again while the film is annealed at 850 K, above T_g.

Another type of thin films, bi- or multi- component multilayer thin films, usually utilize solid-state reactions as post-treatments. Two kinds of post-treatments are usually used for the modification of bi- or multi- layer thin films:

(1) Stress-induced amorphizaition process,

(2) Annealing-induced amorphization processes.

The main purpose of these processes is to modify thin films. Stress-induced phase transformation were discovered in 1995 by Bakker et al. [58]. However, through refinement of grain size by plastic deformation, nanocrystalline even amorphous Zr-based thin films were produced by Hsieh et al. [59].

In the past, amorphization of Zr-Ni multilayer thin films through post-thermal treatment first reported by Schwarz and Johnson [10] is popularly noted in 1983. Following this, Cotts et al. [27] announced a DSC analysis for amorphization in 1986. The sputtered multilayer $Ni_{68}Zr_{32}$ thin film was annealed in argon at the heating rate of 10 K/min. The multilayer thin film consists of alternative layer of 300 Å in thickness was deposited on cleaved NaCl substrates. In the DSC curve as shown in Figure 2-18 [27], two separate exothermic reactions exhibit the amorphization at 580 K and crystallization at 830 K, selected at the center of the reaction peak, respectively. The XRD scan profile of as-deposited Ni-Zr film reveals the Bragg peaks of α-Zr and Ni. However, Figure 2-19 [27] indicates the XRD scan of the film annealed at 670 K shows disappearances of elemental peaks and an appearance of a broad hump, an evidence for the formation of the amorphous phase. The residual (002) reflection of Zr corresponds to the thicker external Zr layers on the sample, which was not expected to react fully. While annealing temperature reaches 830 K, the XRD scan profile shows the occurrence of the crystallization.

At the same year, Newcomb and Tu [39] also utilized the annealing process to analyze metal-metal interfaces. The TEM bright-field image, as shown in Figure 2-20 [39], pointed out the appearance of the $Ni_{60}Zr_{40}$ bilayer thin film and its interface formed after $300^{o}C$ annealing for 60 min. Compared with the films annealed at $300^{o}C$ for 240 and 720 min, respectively, in all cases the voids were confined to the Ni/NiZr interface, as red circles marked in Figure 2-21 [39]. This presence of voids indicates that Ni is the dominant diffusion species in the formation of the amorphous layer. In other words, nickel has a high rate of diffusion in amorphous NiZr. The void appearance is similar to the Kirkendall effect in a diffusion couple.

From viewpoints discussed above, nature of thin films is strongly related to the growth condition, as shown in Figure 2-22 [53]. It becomes very important to understand two major parameters in the deposition process. They are listed below:

(1) Working gas pressure,

(2) Substrate temperature during deposition process.

Table 2-5 [13] points out the relation between the working pressure and microstructure. With decreasing oxygen content in the target, it is easier to form amorphous structure. If the 97% sintered target was used, at 0.2 Pa Ar pressure, films were crystallized. When the Ar pressure was increased to 0.4 Pa, films were amorphous and ductile. When the Ar pressure was increased to 2.0 Pa, the resulting films were partially crystallized and brittle.

To summarize the points mentioned above, lower working pressure would help the formation of the amorphous structure. However, the resistivity of Pd-TFMG also exhibits the increasing tendency with Ar pressure as shown in Table 2-6 [13]. The reason for the smallest resistivity at 0.2 Pa is due to the crystallization of the thin films. The thin films made at 2.0 Pa Ar pressure might be porous and contain more Ar inside, which causes a larger resistivity and a higher T_g than those of the thin films made at 0.4 Pa Ar pressure.

Another important parameter is the substrate temperature. Chen et al. [29] indicated that the quenching rate plays a most important role in the amorphization of binary alloys by magnetron sputter deposition. Heat remove by liquid nitrogen or helium from substrate can restrict adatoms to diffuse around the surface. A sufficient quenching rate is able to stop the nucleation of the crystalline phase and then help the formation of amorphous structure.

2-7 Properties of thin film metallic glass

2-7-1 Thermal properties

The thermal stability of the amorphous thin films is the most important key for the micro-forming application. The Pd-based ($Pd_{76}Cu_7Si_{17}$) monolayer thin film metallic glass appears to be a very suitable material for MEMs because of its excellent thermal stability. According to Figure 2-23 [13], Pd-TFMG exhibits an endothermic reaction due to the glass transition at about 637 K and an exothermic reaction due to crystallization at about 669 K. The glass transition temperature (T_g), crystallization temperature (T_x) and supercooled liquid region (ΔT_x) are 637 K, 669 K and 32 K, respectively.

Figure 2-24 [13] shows that the time-temperature-transformation diagram (TTT diagram) of Pd-TFMG. The incubation time of the glassy phase near the glass transition temperature (640 K) is estimated to be about 3000 s, while the retaining time of the glassy phase becomes shorter and is estimated to be about 100 s near the crystallization temperature (659 K).

2-7-2 Mechanical properties

As annealing time increases, the crystalline phase gradually precipitates from the amorphous matrix and gradually replaces the amorphous matrix. Finally, the films would exhibits the brittle nature as the ductility disappears. This is annealing-induced embrittlement reported by Yuan et al. [60]. The amorphous structure would transfer to the crystalline structure because the free volume decreased due to atomic interdiffusion. Less free volume means the arrangement of atoms is more close together. Larger stress was needed for deformation. The crystalline precipitate becomes the reinforcement.

Another related research of Zhang et al. [33] reported the mechanical properties of the Pd–based thin film near the glass transition temperature (T_g). Figure 2-25 [33] indicates the cantilever of the Pd-based thin film fabricated by focused ion beam (FIB) and annealed at 640 K for 90 s and 480 s. The decreasing trend of notch fracture toughness (K_C) means that a longer annealing time would increase the propensity for brittleness of the thin-film metallic glass, as shown in Figure 2-26 [33].

The fracture surface of the notch shows a phenomenon of the annealing-induced embrittlement, as shown in Figure 2-27 [33]. Figure 2-27 (a) shows a scanning electron microscopy (SEM) micrograph of the fracture mode showing that the thin-film metallic glass failed in mode I. The fracture surface of the as-deposited thin film exhibits a typical vein pattern, as shown in Figure 2-27 (b). It is interesting that the average size of the vein is approximately several tens of nanometers, which is much smaller than that of bulk metallic glasses. The vein pattern gradually transferred to the river-like pattern which exhibits the brittleness of the thin-film metallic glass as annealing time increased up to 90 s and 480 s shown in Figure 2-27 (c) and (d), respectively.

At the same year, the evidence of plastic deformation instability in the Au/Cu multilayer thin film was discovered by continuous stiffness measurement (CSM) [32]. Au/Cu multilayers with equal total thickness of 1 μm but with different individual layer thickness of 25, 50, 100, and 250 nm were deposited by RF sputtering. All films were indented to 1 μm under the continuous measurement by the nanoindenter. Plastic deformation would occur with the applied stress on the film.

It is well known that the main mechanisms of plastic deformation for crystalline metals are slip, twinning, and grain boundary sliding. However, the microstructure of deformed materials with micrometer to nanometer scale exhibits plastic deformation instability, also called the shear band, as shown in Figure 2-28 [32]. Zhang's report points out that shear bands partake in the plastic deformation of the multilayer Au/Cu thin film. In the plastic deformation occurs, the movement of the dislocations in the film is limited by the boundaries, such as extrinsic boundaries and grain boundaries. The reason why shear band formed is the boundaries, would impede the common mechanism of the plastic deformation.

Figure 2-29 [32] indicates that the hardness decreases as individual thickness (λ) increases due to the smaller individual thickness which can restrict the movement of dislocations. In other words, in order to overcome the obstacle, such as grain boundaries, the larger load is needed for plastic deformation. The direct evidence is the decrease of the pile up height (h_{pu}) as decrease of the individual thickness as shown in Figure 2-29 [32]. While λ reduces, shear bands take part during the deformation process, even become the predominate mechanism.

In Figure 2-30 [32], the Au/Cu interfaces of the λ = 250 nm multilayer were slightly kinked toward the extrusion direction and the deformation mainly occurred within Au and Cu layers. When λ is reduced to 100 nm, the Au/Cu interfaces close to the indents began to be strongly kinked toward the shearing direction but still remained fully intact, as shown in Figure 2-30 (b). No delamination and voids were found at any of the interfaces. Similarly, Figure 2-30 (c) revealed the kinked interfaces along the shearing direction also appeared in the λ = 50 nm multilayer. Especially, when λ drops to 25 nm, a few narrow shear bands could develop from the surface into the multilayer, and are well correlated with the circular shear bands at the film surface, as indicated by arrows in Figure 2-30 (d).

When the Au/Cu interface is close to the multilayer surface, the interface kink angle, which is defined as the angle between the kinked interface and the unkinked interface, gradually increases from 0° toward the direction that is nearly parallel to the shear banding direction. These results make it clear that shear banding becomes more prevalent with the decrease of individual layer thickness of the metallic multilayers.

Compared with the Pd-based BMGs and TFMGs, they have the similar process of the fabrication, so they have the similar properties. Table 2-7 [13] shows that the Pd-based TFMGs and BMGs both have the same temperature expansion coefficient, almost the same densities, and the same glass transition temperatures, but a obvious difference in Young’s modulus. The higher cooling rate in the sputtering process results in the microstructure consisting with columnar nano-grains. The particular nature may be the cause which leads to a smaller Young's modulus for the TFMGs.

2-7-3 Electric and magnetic properties

As mentioned above, the PdCuSi thin film metallic glass is a suitable material in MEMs [13]. However the application of PdCuSi TFMGs as microinductors and microprobes is quite difficult, because the electrical resistance of materials used in electrical devices needs to be as low as possible. According to Table 2-8 [31], thin film metallic glasses all have higher electrical resistance than Cu and W films. Annealing is able to make the nanocrystalline phase precipitate, but must avoid an occurrence of annealing-induced embrittlement. Pd-Cu or Pd-Si nanocrystalline phase which precipitated from the amorphous matrix after annealing can effectively lower the electrical resistance. Figure 2-31 [31] shows the electrical resistance of Pd-TFMG was reduced to about 50 μΩcm without inducing embrittlement which was proved by bending test.

In 2005, Chu et al. [12] has reported the influence of electrical properties by annealing-induced amorphization. In his report, it is indicated that the magnetic property of the Fe-based thin films is also influenced by amorphization. Annealing-induced amorphization takes place in the sputtered $Fe_{65}Ti_{13}Co_8Ni_{17}B_6Nb_1$ film at 773~823 K, while nanocrystallization of various phases evolves with increasing annealing temperature, yielding alterations in electrical resistance, hardness, and magnetic properties. The induced anisotropy at 923-973 K is originated from the positive magnetostriction and the compressive stress due to the large FeNi lattice phase present in the small Fe(Ni) lattice matrix, as shown in Figure 2-32 [61].

Chapter 3 Experimental Procedures

Interface reactions in the Mg-Cu thin films may be referred from the Mg-Cu equilibrium phase diagram, as shown in Figure 3-1. The Mg-Cu amorphous and intermetallic phases might form in the binary thin film.

The binary metallic thin films were fabricated using sputtering deposition. The microstructure was examined by X-ray diffraction (XRD), scanning electron microscopy (SEM) with energy dispersive X-ray spectrometry (EDS), and transmission electron microscopy (TEM). The thermal stability of the Mg-Cu metallic thin films was examined using a differential scanning calorimeter (DSC). The mechanical properties of the Mg-Cu metallic thin films were evaluated by nanoindentater. The flow chart of the experimental procedure is shown in Figure 3-2.

3-1 Materials

Mg and Cu targets used in this study were purchased from Well Being Enterprise Co., Ltd, Taipei, Taiwan. The purity level of the magnesium and copper targets are 99.99%, 99.99%, respectively.

3-2 Sample preparation

3-2-1 Substrate preparation

In this experiment, films were deposited on is P-type (100) silicon wafer. In order to avoid some other impurities and greasy dirt adhering to the substrates, the following surface cleaning procedure was adopted.

(1) With deionized (DI) water, an ultrasonic cleaner was used to clean the substrates for 10 minutes to remove the dust and impurities on the surface of substrate.

(2) An ultrasonic cleaner was used to clean the substrates in alcohol for 10 minutes to remove the greasy on the surface of substrate.

(3) After rinsing in alcohol, an ultrasonic cleaner was used to clean it in acetone for 10 minutes.

(4) After rinsing in acetone, we used an ultrasonic cleaner is used to clean the substrates in DI water for 10 minutes.

(5) Air was used to dry the substrates.

3-2-2 Film preparation

In this study, monolayer and multilayer thin films were prepared by DC and RF magnetron sputtering with a target of 50.8 mm in diameter at a working pressure of 3×10^{-3} torr. There were two kinds of procedures which are listed below:

(1) Mg-Cu monolayer thin films using cosputtering,

(2) Multilayer thin films composing of alternative Mg and Cu layers with the atomic ratios of 3(Mg): 2(Cu) and 1(Mg):4(Cu).

The first type can be fabricated using the co-sputtering deposition process with magnesium and copper targets. A rotary pump was used to achieve medium vacuum, and a cryo-pump was used to achieve a base pressure less than 1×10^{-6} torr. There was a load-lock chamber, for quick and convenient exchanging of substrates without venting the main chamber.

After achieving the base pressure, Ar was introduced into the chamber, and targets were pre-sputtered by inserting a movable shutter for one minute. During sputtering, the magnesium target was set up on the RF gun with 100 and 50 W, and the copper target was set up on the DC gun with 150, 100, 50, 25, and 15 W, respectively. The substrate is set on the sample holder, 80 mm higher than the target. Working gas was pure argon. Argon flow rate was fixed at 30 standard cubic centimeters per minute (sccm). During deposition, the substrate was rotated with an average speed of 15 rpm for the uniform distribution of the film thickness.

The second type can by fabricated using layer-by-layer deposition with alternative magnesium and copper. The details of the monolayer and multilayer sputtering conditions are summarized in Tables 3-1 and 3-2, respectively. During deposition, the substrate was rotated with an average speed of 15 rpm for the uniform distribution of the film thickness.

The multilayered specimens with the different atomic ratios are named as 20T32, 40N32, 20T14, 40T14, respectively, as shown in Table 3-3. The front numbers of the names represent that the specimens consist of 20 or 40 layers, respectively. Then, the latter numbers of the names mean the calculated compositions of the multilayer. Then, T mean the multilayered films consisting of thick Mg and Cu individual layers, and N mean the multilayered films consisting of thin Mg and Cu individual layers. The co-sputtered specimens of the 100 series under different conditions are named as 100-150, 100-100, 100-50, 100-25, and 100-15. The front part was the power of Mg gun set at 100 W. However, the latter represents the set power of DC Cu gun, 150, 100, 50, 25, and 15 W, respectively. Then, the co-sputtered films of the 50 series under the different conditions are named as 50-150, 50-100, 50-50, and 50-25. The front part represents the power of Mg set at 50 W. The latter numbers mean the power of Cu, as shown in Table 3-4.

3-2-3 Post-deposition treatments

According to the DSC curves of 100-150, the temperature of the post heat-treatment was set at 423 K for the 100-150, 100-100, 100-50 and 100-25 specimens. By using the isothermal heat-treatment, the structural transformation can be understood in different compositions of Cu. Moreover, thermal stabilities at this temperature of these specimens can also be evaluated qualitatively. The process of the heat treatment under a base pressure below 10^{-3} torr was divided into five steps listed below, and is also shown in Figure 3-3:

(1) 298 K to 343 K at 20 K/min

(2) Isothermal at 343 K for 5 minutes

(3) 343 K to 423 K at 60 K/min

(4) Isothermal at 423 K for 60 minutes

(5) The XRD data were collected per hour after the specimens were cooled down.

In the multilayered case, owning to the discrepancy between the melting points of Mg and Cu, it can be expected that Mg atoms can diffuse into individual Cu layers at about $0.2T_m$ (403 K). According to the research of Arcot et al. [62], the diffusion between individual 50-nm-thick Mg and Cu layers would occur around 363 K, much lower than 403 K, due to the large different free energy of Mg_2Cu than the Mg-Cu amorphous phase. Hence, the multilayered films were annealed under the low temperature of 363 K, in an attempt to avoid the formation of intermediate phase between the metal and compound phases.

The temperature of the heat treatment in this study was set to be at 363 or 413 K, judged from the DSC curve of the Mg-Cu multilayered thin films [63]. First, the process of the post heat-treatments of 20T32 and 40N32 at 413 K under a base pressure below 10^{-3} torr was divided to five steps, as shown in Figure 3-4:

(1) 298 K to 343 K at 20 K/min

(2) Isothermal at 343 K for 5 minutes

(3) 343 K to 413 K at 60 K/min

(4) Isothermal at 413 K for 30 minutes

(5) The XRD data were collected per hour after the specimens were cooled down.

In order to remove H_2O in the chamber and the specimens, the temperature was first hold at 343 K for 5 minutes. Then, the temperature was raised to the set point, and held for a period of time.

For the specimens of 20T14 and 40N14, another process of the heat treatment at 363 K under a base pressure below 10^{-3} torr, omitting the isothermal step for remove H_2O, were applied, as shown in Figure 3-5:

(1) 298 K to 363 K at 60 K/min

(2) Isothermal at 363 K for 30 minutes

(3) The XRD data were collected per hour after the specimens were cooled down.

3-3 Property measurements and analyses

3-3-1 X-ray diffraction

The nature of the Mg-Cu binary thin film fabricated by the magnetic sputtering deposition was examined by X-ray diffraction (XRD). The SIEMENS D5000 X-ray diffractometer with Cu K_α radiation (λ = 1.5406 Å), operated at 40 kV and 30 mA, and equipped with 0.02 mm graphite monochrometer, was utilized. The ranges of the diffraction angle 2θ of co-sputtered and multilayered specimens were within 20^o to 60^o and 17^o to 55^o, respectively, at the scanning rate of 0.1^o per four seconds.

3-3-2 Preparation of TEM specimens of co-sputtered and multilayered thin films

In order to understand the microstructure of Mg-Cu metallic thin film, plane-view TEM specimens of co-sputtered 100-150 and 100-100 samples were prepared via ion-thinning technique. Then, to prepare the plane-view TEM specimen, free-standing 100-150 and 100-100 samples were bound on a 3-mm slot grid and thinned until the thickness is lower than 100 nm using an ion miller (GATAN PIPS-691 Ion-Miller). Finally, the plane-view specimens were examined using the JOEL 3010 analytical scanning transmission electron microscope (AEM) at 300 kV.

To prepare the cross-section TEM (XTEM) specimens of 20T32 and annealed 20T32, at 413 K under a base pressure below 10^{-3} torr for 120 min, advanced focus-ion-beam (FIB) technique was employed. The focus ion beam instrument (SMI 3050) belongs to the dual-beam type of FIB, where one beam can provide a second-electron image to observe the appearance of the sample, and another can provide the etching function by Ga^+ ion for the XTEM specimen, cross-section image, and patterns, and so on. First, these specimens, fixed on an aluminum holder and cleaned by nitrogen, were moved into the FIB chamber. As shown in Figure 3-6, the approximate 1 μm × 3 μm area was deposited with a carbon film to protect the damage from the Ga^+ ion during the process of preparation. Then, the slope-etching was employed at the upper and under areas. At this moment, the archetype of the XTEM specimen in the trapezoid shape was fabricated. The XTEM archetype was retouched two parallel planes, and the thickness of the XTEM specimen was thinned out less than 100 nm. Finally, bottom cutting was employed, and both sides of the XTEM specimen were cutted. The finished XTEM specimens were moved on a carbon-coated Cu grid, as shown Figure 3-7 (a) and (b). The plane-view specimens were examined using the JOEL 3010 AEM at 200 kV.

3-3-2 Qualitative and quantitative constituent analysis

In order to identify the constituent component and confirm the composition percentage of the binary metallic thin films, the samples were characterized by a scanning electron microscopy (SEM) with energy dispersive X-ray spectrometry (EDS). The film surface was selected to examine the quantity of the designed compositions by EDS.

3-3-3 Thermal analysis using differential scanning calorimetry (DSC)

The Perkin Elmer, Pyris Diamond DSC was used for thermal analysis to determine the temperatures of the phase transformation. The as-deposited films were first peeled off, avoiding the effect of the substrate. In DSC analysis, for the non-isothermal heating course, the binary thin films were heated to 523 K at the heating rate of 5 K/min.

3-3-4 Nano-mechanical analysis using nanoindenter

The MTS XP nanoindenter was used to evaluate the nanomechanical properties of the 4-μm-thick Mg-Cu metallic thin films coated on the Si (001) wafer. During the process of indentation, the deeper penetration depth, the higher effect of the substrate. Generally speaking, the examined nano-mechanical properties without the substrate effect were tested within about 10% thickness of the film. Hence, 100-150, 100-100, 100-50 with the Si substrate were tested by the nanoindenter operated in the continuous stiffness measurement (CSM) mode, which involves the application of a very small oscillation force, equal to 45 Hz, to the loading force at a high frequency. From the oscillation of the resulting depth signals one can continuously measure the contact stiffness and calculate the hardness and modulus values [64]. In this study, the 100-150, 100-100, and 100-50 specimens were indented into 10% thickness (400 nm) under a constant strain rate of 5×10^{-3} s^{-1}.

Chapter 4 Results

4-1 EDS analysis of co-sputtered Mg-Cu thin films

The compositions of the Mg-Cu co-sputtered thin films are identified by energy dispersive X-ray spectrometry (EDS), as shown in Table 4-1. In comparison of the EDS results for the 100 series, the 100-150, 100-100, 100-50, 100-25, and 100-15 specimens, the Cu content gradually decreases with decreasing Cu power. Moreover, as the Cu power is lower than 25 W, the predominant Mg would lead to the oxidation of Mg, and the compositions are abnormal to the decreasing trend with the Cu power. According to the EDS result of 100-15, the film contains about 15 at% oxygen, meaning a large part of contribution was originated from the oxides, mainly MgO.

For the 50 series, it reveals the same tendency as the 100 series. The Cu content decreases with decreasing Cu power. Similarly, the oxidation of Mg would occur and the compositions are abnormal as well. According to the EDS result of 50-25, the film also contains about 15 at% oxygen like 100-15, meaning a large part of contribution was originated from the oxides, mainly the MgO.

4-2 X-ray diffraction analyses

4-2-1 XRD analysis of Mg-Cu co-sputtered thin films

Figure 4-1 exhibits the XRD patterns of the as-deposited 100 series. Compared with the spectrums of 100-150 ($Mg_{17.7}Cu_{82.3}$), 100-100 ($Mg_{23.5}Cu_{76.5}$), 100-50 ($Mg_{40.4}Cu_{59.6}$), 100-25 ($Mg_{61.9}Cu_{38.1}$) and 100-15 ($Mg_{39.9}Cu_{43.5}O_{16.6}$), the locations of hump center are related to the composition. The centers of the humps shift to the right with increasing Cu content. In addition, 100-150 and 100-25 seem to contain some minor nano-particles.

Figure 4-2 presents the XRD spectrums of the 50 series. In comparing with these specimens, the peaks at 43.4^{o} and 50.6^{o} are referred to the Cu (111) plane and (200) plane, respectively, meaning 50-150 and 50-100 consist of almost pure Cu and no Mg. Next, comparing 50-150 and 50-100, 50-100 exhibits the same Cu crystalline peaks of Cu (111) and (200) as 50-150, but the peaks are more broadened implying that the 50-100 specimen consists of smaller Cu grains. This would be resulted from that a lower Cu power leads to a lower kinetic energy of Cu incident atoms, implying the Mg and Cu could not mix well.

As Cu power decreases, the Cu contents of 50-50 and 50-25 decrease with decreasing Cu power, implying the re-sputtering effect is unapparent. Figure 4-2 shows that the 50-50 and 50-25 specimen exhibit broadened weak Mg peaks consisting of a mixture of (0002) and ($10\bar{1}1$) planes at 33^{o} to 39^{o}, Cu (111) and (200) planes at 43.4^{o} and 50.6^{o} meaning that the mixing effect is also more and more unapparent during deposition. Due to the occurrence of the specific Mg and Cu structures, it is reasonable to suggest that the two specimens consist of separated nano-grains of Mg and Cu, not like the 100 series. Besides, the nano-domains of Mg and Cu are much more reactive to oxygen in air, meaning the oxide would form on the surface of the films.

4-2-2 XRD analysis of Mg-Cu multilayered thin films

The structures of the as-deposited multilayered thin films are identified by X-ray diffraction, as shown in Figures 4-3 and 4-4. According to the XRD patterns of 20T21 and 20T14, there exhibits a very strong texture of the (0002) plane of Mg at 34.5^o, compared with the XRD pattern of the pure Mg film, as shown in Figure 4-5. Meanwhile, the as-deposited Cu film exhibits the similar occurrence with the strong plane textures of the (111) plane at 43.3^o and minor (002) at 50.5^o, compared with the pure Cu film, as shown in Figure 4-5. In these results, it can be inferred that individual Mg and Cu layers grow along the close-packed crystalline planes, irrespective of the structure of the Si substrate.

In addition, the XRD patterns of 40N32 and 40N14 which are the same texture as those of 20T32 and 20T14, as shown in Figures 4-3 and 4-4, exhibit broadening crystalline peaks of Mg and Cu is due to the thinner thicknesses of individual layers.

4-3 TEM observation of co-sputtered Mg-Cu thin films

4-3-1 Microstructure of co-sputtered 100-150 ($Mg_{17.7}Cu_{82.3}$) and 100-100 ($Mg_{23.5}Cu_{76.5}$) thin films

In order to understand the influence of the microstructure on the mechanical properties, the microstructures of 100-150 and 100-100 are examined using TEM. Figure 4-6, the plane-view bright-field image (BFI) of 100-150, exhibits many particles (~10 nm) dispersed in the matrix. The selected area diffraction patterns (SADP) of 100-150, as shown in Figure 4-7, indicated that the 100-150 film consists of the mixture of the $MgCu_2$ nanocrystalline and Mg-Cu amorphous structure.

Similarly, in another case of 100-100, Figure 4-8 shows that the 100-100 specimen consists of many fine $MgCu_2$ particles, which particle size is about 10 nm. The dark-field image (DFI) of 100-100, as shown in Figure 4-9, exhibits the amorphous-nanocrystalline structure [65]. Moreover, Figure 4-10 shows the microstructure around the $MgCu_2$ particles (about 20 nm) with several nanometer diameter. Supposedly, the structure consist of Mg-Cu amorphous and smaller $MgCu_2$ nanoparticles, as shown in Figure 4-11. It will be discussed in the next section.

4-3-2 High-resolution TEM observation of co-sputtered 100-100 thin films

According to the TEM BFI and DFI, the contrast of the DFI can not provide the sufficient information for the $MgCu_2$, Cu, and Mg-Cu amorphous phases. Hence, it is necessary to identify the phases in the 100-100 specimen using the high-resolution TEM (HRTEM) technique. In addition to the 10~20 nm $MgCu_2$ particles, as shown in Figure 4-12, the specimen seems to exhibit a different structure in the localized area, such as the marked region by the circle. The high-resolution TEM image exhibits many $MgCu_2$ nanocrystals and amorphous particles, as shown in Figures 4-12, 4-13 and 4-14.

Around the $MgCu_2$ particles, there exhibits an irregular amorphous particle about 15 nm surrounded by the $\{1\bar{1}0\}$ $MgCu_2$ crystalline phases as shown in Figure 4-12. In a localized area, Figures 4-13 and 4-14 show different structures: one consists of about 5-nm amorphous particle in the $MgCu_2$ matrix; another exhibits 2-nm amorphous particles in the $MgCu_2$ $\{1\bar{1}0\}$ matrix.

4-4 Thermal analysis

4-4-1 DSC analysis of Mg-Cu co-sputtered thin films

For the 100 and 50 series, the thermal properties must be compared under the same condition, such as the same substrate and background pressure, etc. However, only the specimens of 100-150 and 100-100 can be peeled off from the Si substrates. Hence, the thermal properties of other specimens can not be measured, and the thermal properties are evaluated based on the composition difference. The modified heating DSC curve of the 100-150 ($Mg_{17.7}Cu_{82.3}$) specimen is shown in Figure 4-15 with a heating rate of 5 K/min. The glass-transition temperature (T_g) is located at 428 K, and the onset of crystallization temperature is located at 460 K.

4-4-2 Structural transformation of the 100 series thin films at 423 K

According to the heating DSC curve of 100-150, the partial amorphous Mg-Cu thin film, the glass transition temperature is located at 428 K. Due to the partial amorphous structure, existed nuclei would make the Mg-Cu crystallization occurs at a lower temperature. Hence, the temperature of the isothermal heat-treatment for 100-150 ($Mg_{17.7}Cu_{82.3}$), 100-100 ($Mg_{23.5}Cu_{76.5}$), 100-50 ($Mg_{40.4}Cu_{59.6}$) and 100-25 ($Mg_{61.9}Cu_{38.1}$) is evaluated at 423 K, about 40 K lower than the onset of the crystallization at 460 K.

Figure 4-16 shows the change of the XRD patterns of 100-150, showing the structural transformation due to crystallization. The smooth hump gradually transfers to a sharp peak with increasing time of the isothermal heat-treatment. According to the Mg-Cu phase diagram, the $MgCu_2$ phase, with the FCC structure and a lattice constant a = 7.034 Å, would form in the Cu-$MgCu_2$ region. Compared with JCPDS, the large peak appears to reflect the formation of the compound phase, suggesting the Mg-Cu amorphous phase transfers to the $MgCu_2$ phase. The small humps at around 21^o and 50^o correspond to the formation of $MgCu_2$ in (111) and (400) planes, respectively. In the case of 100-100, it exhibits the similar occurrence but another peak forms at about 34° possibly owning to the contribution of the $MgCu_2$ (220) plane, as shown in Figure 4-17.

While the Cu content decreases, a different structural transformation occurs in the 100-50 and 100-25 specimens. Figure 4-18 shows the transformation of 100-50, showing that the hump between 36° to 48°, suggesting a mixture of Mg_2Cu (260), (331), (080), (351), (440), (191) planes and $MgCu_2$ (220), (311), (222), (400) planes gradually sharpens, and the range of sharpening hump increases with time. In the case of 100-25, the structure of as-deposited film already exhibited a minor dispersed nano-crystalline Mg_2Cu phase, as shown in Figure 4-19. As the heat treatment time increases, the peak shifts to the left compared to the original structure, and the strong peaks at 24.1°, 37.1°, 39.6°, and 44.5° formed which correspond to the Mg_2Cu (131), (331), (080), and (440), respectively. Besides, during isothermal annealing, the small intermediate hump from 33° to 40°, such as the ellipses shown in Figure 4-19, appears in a short period, and disappears. In the meantime the peak of Mg_2Cu (331) appears, suggesting that the as-mentioned hump seems to correspond the transitional phase induced by thermal diffusion.

4-4-3 Formation of intermediate phase of Mg-Cu multilayered thin films at 413 K and 363 K

According to the research of Arcot et al. [62], diffusion would occur at temperatures higher than 363 K. In the case of specimens consisting of thicker individual layers, no evidence of the Mg-Cu metastable phase, such as Mg-Cu amorphous phase, was formed in the Mg-Cu multilayered system as isothermally annealed at 413 K and 363 K, implying the thickness of Mg and Cu individual layers would lead to the variation of the overall interface energy in the mass-conservation system. The structural transformation of the 20T32 specimens annealed at 413 K is shown in Figure 4-20. The peaks of Mg_2Cu at 19.5^o, 37.4^o, 39.6^o, 44.6^o, and 49.1^o, indentified as the planes of (040), (331), (080), (440), and (191), gradually form, and the intensites of the peaks at 19.5^o and 39.6^o become very strong. In other words, the peak intensities of Mg and Cu decrease with increasing time.

The 40N32 specimens with the thicknesses of the individual layers ten times lower than those in 20T32, are annealed under the same condition. In addition to a slight negative heat of mixing between Mg and Cu (-3 kJ/mol), the thickness effect also induces the greater driving force for the Mg and Cu atoms to mix together. According to Figure 4-21, Mg_2Cu rapid forms within 30 minutes during the isothermal annealing at 413 K owning to a large global interface energy. At 413 K, Mg_2Cu formed easily since the Mg atoms diffuse into the Cu layers and react with Cu atoms rapidly.

For the case at a lower temperature, 363 K, the diffusion rate of Mg at this temperature is very slow [62]. Considering the case of 20T14, the specimens annealed at 363 K, as shown in Figure 4-22, the peaks of Mg_2Cu still grow gradually with the time of the heat treatment, without the trace to support the formation of an amorphous phase. In the Cu-rich multilayered thin films, pure Cu peaks are left after annealing. Then, the phase transformation of 40N14 at 363 K, the formation of Mg_2Cu with the increasing annealing time is similar to that in 40N32 annealed at 413 K, as shown in Figure 4-23.

Compared with the multilayered film consisting of thick and thin individual layers, Mg and Cu layers in the thinner-layer multilayered films would react with each other at a lower temperature and at a faster reaction rate than that in the thicker-layer multilayered films. 40N32 and 40N14 exhibit the same occurrence. Comparatively speaking, the current experiment and previous researches all express the missing metastable amorphous phase during the thermal-induced diffusion between the Mg and Cu layers.

4-4-4 Structural transformation of 20T32 by TEM observation

According to section 4-4-3, the XRD results shows Mg_2Cu rapidly forms during annealing. Then, from the XTEM observation, as shown in Figure 4-24 (a), for a representative image for the Mg-Cu multilayer, the white layers and black layers represent Mg layers with nominal 150 nm in thickness and Cu layers with nominal 50 nm in thickness, respectively. After annealing in vacuum at 413 K for 2 hours, Figure 4-24 (b) shows the thickness of Mg and Cu individual layers decrease, and the intermediate gray layers, Mg_2Cu layers, rapidly formed within Mg and Cu layers due to a negative heat of mixing (-3 kJ/mol) and an increase of interfacial energy in the overall system. Moreover, according to the XRD result, as shown in Figure 4-22, the result in the 20T14 specimens annealed at 363 K is similar to that in the 20T32 specimen annealed at 413 K, implying that the Mg_2Cu formation in not related to the thickness of the individual layer (greater than approximately 50 nm). Also, the TEM observation proved the intermediate layers formed at the Mg-Cu interfaces

4-5 Mechanical analysis of co-sputtered 100-150 ($Mg_{17.7}Cu_{82.3}$), 100-100 ($Mg_{23.5}Cu_{76.5}$), and 100-50 ($Mg_{40.4}Cu_{59.6}$) using nanoindenter

Summarized sections 4-1 to 4-4, Table 4-2 shows the overall Mg-Cu specimens and their structural characteristics. Only three specimens, 100-150, 100-100, and 100-50, exhibit a structure consisting of the major Mg-Cu amorphous phase and the minor $MgCu_2$ phase. Hence, the mechanical properties would be focused on as-mentioned three specimens. For the cases of thin films, it is found that the detected hardness and Young’s modulus increase with increasing indentation depth, called as substrate effect, when the film is too thin, we would not get the true properties of the films. However, the substrate effect is different case by case for different films on the same substrate. It is generally acknowledged that the nano-mechanical properties tested within 10% film depth of the film is free from the substrate effect [66].

The hardness-displacement and modulus-displacement curves, with a penetration depth of 400 nm at the strain rate of 5×10^{-3} s^{-1}, are shown in Figure 4-25. It is obvious that the values of hardness almost maintain a constant over the displacement, and the value of Young's modulus, too. In the initial stage (<50 nm in displacement), the obtained value is very irregular due to the geometry of the Berkevich tip.

Furthermore, Figure 4-26 exhibits the Young's modulus and hardness of 100-150, 100-100, and 100-50 from the unloading curves. According to these results, the Young's modulus and hardness of the 100-100 specimen are higher than those of 100-150 and 100-50. Figures 4-27 to 4-29 are the load-displacement curves of 100-150, 100-100, and 100-50. In these curves, the "pop-in" effect appears during the indentation, showing the formation of many shear bands in the specimens.

Chapter 5 Discussion

5-1 Composition shift due to different powers

According to section 4-2, the compositions of the films are strongly related to the deposition rate and the competition between Mg and Cu. If the plasma of the two kinds targets do not interfere and react to each other, the compositions of the co-sputtered films ideally have to match the deposition rates of individual Mg and Cu. In fact, the ideal case does not exist due to the competition of deposition and chemical reaction of the Mg and Cu atoms in the mixed plasma. In this experiment, the deposition rate was determined to be nominally 40 nm/min at DC 150 W for Cu and 10 nm/min at RF 100 W for Mg, respectively. Hence, it can be suggested that the incident Cu atoms have a higher kinetic energy and momentum than Mg atoms. In another case, a large amount of deposited Mg atoms would be removed away by the incident atoms for Cu at the situation of DC 150 W for Cu and RF 50 W for Mg, where individual deposition rate is 40 nm/min and 10 nm/min, respectively.

According to Figure 5-1, based on the individual deposition rate of Mg and Cu, the Cu content of the as-deposited thin films are slightly higher than expectation at higher Cu powers, and much lower than expectation at lower Cu powers due to the re-sputtering of Cu, in both the 50 and 100 series. The expected values are extrapolated for the 100 series by the experimental values of deposition rates based on RF Mg 100 W/DC Cu 100 W and RF Mg 100 W/DC Cu 150W.

In this study, the condition of the deposition is under a fixed Ar pressure (3 mtorr), fixed working distance (80 mm) and rotation speed (15 rpm). In one-component system, many factors are involved in the change of the deposition rate. At a fixed Ar pressure, working distance and rotation speed, the form of power supply, and the setting power are the important factors in influencing the deposition rate. In addition, a higher deposition rate occurs using a DC power than a RF power. Furthermore, a different setting power would bring about the several variations between the plasma and the substrate, such as the quantity of the incident atoms, the mean free path of the incident atoms, the ratio of the adhesion of the incident atoms and desorption for the as-deposited atoms, during the deposition process.

First, the power of cathodes lead to the quantitative variation of the incident atoms and the change of average mean free path, directly proportional to the inverse probability of collision, as shown in Figure 5-2 [52]. The curve can be divided into three regions. Region I exhibits a low probability of collision, implying a low deposition rate due to a very low plasma density. In region II, the increasing plasma density would cause more and more incident atoms with the higher kinetic energy forms and the probability of collision increases with increasing volt, meaning that a higher deposition rate appears in this region. Then, the plasma density reaches a saturated situation in region III, but a higher power would give the incident atoms the more kinetic energy, implying the probability of the collision would decreases again. However, the adhesion and desorption of the incident atoms are strongly affected by the kinetic energy of the incident atoms. A very high power would lead the as-deposited atoms to be “re-sputtering” by the incident atoms. Hence, the deposition rate becomes lower again.

As mentioned above, the several important factors involved in the deposition rate in one-component have been discussed. In the binary co-sputtering system, the competition between two elements plays an important role during the co-sputtering process. Above all, compared with Mg and Cu, Mg exhibits a large radii (1.62 Å) and low atomic number (24), but Cu exhibits a small radii (1.28 Å) and large atomic number (64). According to these known data, it can be infer that Cu incident atoms, like small but heavy bullets, with a high deposition rate bombard the substrate at a high Cu power, leading to a loose structure, even micro-pores. Relatively, Mg incident atoms, like balloons, with a slow deposition rate land on the substrate, resulting in a compact structure. The average free path of Cu decreases owning to the participation of Mg incident atoms with a slow deposition rate. However the increased probability of collision between Mg and Cu would lead the transformation of the kinetic energy and momentum from Cu to Mg, leading to the overall increase of surface diffusion ability. During the co-sputtering process, the collocation of DC Cu and RF Mg deposition provides a good mixing between Mg and Cu, small Cu atoms with a high kinetic energy and momentum.

According to Figure 5-1, the irregular variation of composition occurs, suggesting it is mainly caused by "re-sputtering" between the Mg and Cu elements in the co-sputtering system. "Re-sputtering" means partial as-deposited atoms are re-sputtered from the substrate by the incident atoms. In the case of 100 series, the Cu contents are approximately close to the expectable values, calculated from the data of the isolated Mg and Cu depositions. Then, compared with the 100 series, the Cu content of the 50 series specimens are all higher than that of the 100 series since the large difference in the kinetic energy between Mg and Cu. The incident atoms of Cu with a relatively high kinetic energy would impact the surface of the film and make Mg atoms escape from the surface at low Mg powers, such as 50-150 and 50-100, showing the absence of Mg. Hence, the difference between the kinetic energy of Mg and Cu is the key which leads to the deviation of the composition.

The slight negative heat of mixing in the Mg-Cu system would lead to the Mg-Cu clusters while the incident atoms deposit on the substrate, as well as some Mg-Mg and Cu-Cu clusters, too. Incident atoms with high kinetic energy can break up the Mg-Mg and Cu-Cu clusters by implanting to form the more stable Mg-Cu clusters. In the case of low Mg and Cu powers, insufficient kinetic energy can not destroy the clusters of pure Mg and Cu, resulting in separated Mg and Cu nano-grains.

To summarize, the competition between the momentum and kinetic energy of different kinds of incident elements play a critical role in the co-sputtering procedure. The compositions of the 100 series obtained were close to expectation while the Cu power is higher than 25 W. However, a possible reason, re-sputtering, would make the abnormal variation of the compositions in the 50 series. Hence, the composition of the Mg-Cu thin films, from $Mg_{17.7}Cu_{82.3}$ to $Mg_{61.9}Cu_{38.1}$, can be easily controlled at RF target of Mg at 100 W and the DC target of Cu from 25 to 150 W.

5-2 Oxidation of Mg-Cu co-sputtered film

During the deposition process, the incident atoms with energetic energy and momentum continuously attach to the formed film on the substrate, and the kinetic energy and momentum transformation from incident atoms to as-deposited atoms would make the surface diffusion to find the most stable atomic sites as the residual kinetic energy is enough. In other words, sputtering is a special process with surface diffusion, meaning a real-time heat-treatment occurs at a relatively low temperature near the free surface, compared with melt-spinning. Then, in the Mg-Cu co-sputtering process, the content of oxygen contained in the sputtered films suddenly rises about 15 at% while the Cu power is lower than 25 W, as shown in Table 4-1, suggesting that predominant Mg atoms react with oxygen in the air.

In the case of the 100 series, the proper excess energy causes some Mg-Cu crystalline clusters to overcome the energy barrier to transfer to the amorphous clusters or to form the Mg-Cu compounds. However, in the case of low Cu powers, such as 100-25 and 100-15, as shown in Figure 4-1, the as-deposited specimens contain the separated nano-grains of Mg and Cu with their specific structure respectively. A possible kinetic reason is suggested as the formations of intrinsic Mg-Mg, Cu-Cu, and Mg-Cu clusters, while Mg and Cu atoms adhere to the surface of the film during sputtering. The clusters of Mg-Mg, Cu-Cu, and Mg-Cu should disperse in random. At this moment, with insufficient kinetic energy and momentum, most of as-deposited atoms freeze on the free surface. In this case, Mg would rapidly react with oxygen while the film is exposed to air.

From the thermodynamic aspect, the heats of mixing among Mg, Cu, and O are the major factors influencing the formation of oxide or intermetallic compounds. Compared with the heats of mixing of MgO, Cu_2O and the Mg-Cu solid solution, the heats of formation of MgO, Cu_2O, and the heat of mixing of Mg-Cu solid solution are equal to -601.6, -167.5 and -3 kJ/mol at 298 K, respectively, meaning that the formation of oxide in the atmosphere with sufficient oxygen is very easy, especially for MgO. In other words, it is reasonable to suggest that the bonding between Mg and O is very easy to form comparatively.

According to the measured oxygen content, Cu atoms around Mg atoms can reduce the activity of Mg, avoiding oxidation of Mg in air. The reason for incomplete mixing is the incident atoms with the insufficient kinetic energy can not cause the surface diffusion to mix well, even induce the nanocrystalline Mg and Cu which can rapidly react to oxygen.

5-3 Diffusion-induced phase transformation in multilayered thin films

In the Mg-rich multilayered case, the diffusion starts at a relatively low temperature about 363 K. Before this experiment, Arcot et al. [62] and Rodriguez-Viejo et al. [63] have done the related research on the Mg-Cu multilayered films. In their researches, the composition ratio were set to 1(Mg):2(Cu) and 2(Mg):1(Cu). Regardless of the temperature (370 to 773 K) and composition in their studies, the first intermediate phase is always Mg_2Cu. Nevertheless, Mg_2Cu does not form rapidly but step by step. The lateral growth occurs as the initial stage of the diffusion of Mg. Then, the perpendicular growth occurs with a continuous Mg_2Cu layer. Hence, an experiment of Mg-Cu multilayered thin films is designed to compare the thickness effect in the individual layers.

First, the heat treatment of 20T32, consisting of 10 layers of 150-nm-thick Mg layer and 10 layers of 50-nm-thick Cu layer, was subjected to annealing at 423 K under 5×10^{-2} torr. According to the XRD result, as shown in Figure 4-17, the Mg_2Cu phase formed after 30 minutes. As the time of the heat treatment increases, the content of Mg_2Cu increases greatly. Then, another multilayered film designed as the Cu content shift to about 70%, or the 20T14, was annealed at 363 K. However, the interaction between Mg and Cu layers still exhibits the similar result of 20T32 mentioned above, as shown in Figure 4-18. Mg_2Cu gradually forms as the annealing time increase.

Generally speaking, the metastable phases fabricated by the rapid quenching process is the amorphous phases. However, the different occurrences of the metastable phases in the multilayered system after post-annealing have been discovered, such as the formation of the FeB amorphous phase in the Fe/B multilayered structure after post-annealing [67] and the absence of the $NiMn_2$ and Ni_2Mn compounds during the Ni-Mn diffusion couple [57].

The possible reasons that diffusion-induced metastable phase in Mg-Cu multilayer system does not form during low-temperature heat treatment are summarized below. According to previous researches [62,68,69], the dominant factors of the formation of Mg_2Cu are the element with a lower melting point and the structure of the compound. In other words, Mg with a lower melting point should dominate the diffusion. At an enough temperature, Mg atoms near the interface start to diffuse. However, the solubility of Cu atoms in the Mg matrix or Mg atoms in the Cu matrix is almost zero. Hence, the thin Mg_2Cu layers form near the interfaces at the initial stage of the annealing. Once the intermediate layers of Mg_2Cu form, more Mg_2Cu nucleate and crystallize along these layers.

Also, Arcot et al. [62] reported that the transformation from Mg_2Cu to $MgCu_2$ at temperatures higher than 548 K in the Cu-rich alloy. In other words, $MgCu_2$ is the high-temperature phase. Moreover, they also pointed out the first phase formed in the Cu-rich alloy is still Mg_2Cu. With increasing temperature close to the liquidus line of Mg_2Cu equal to 758 K, another transformation occurs from Mg_2Cu to $MgCu_2$ by adding three Cu atoms. The overall reaction sequence in films with an atomic concentration ratio of 2(Cu):1(Mg) is shown below,

$$2Mg+4Cu \rightarrow Mg_2Cu+3Cu \xrightarrow{548K} 2MgCu_2 . \tag{5-1}$$

In the thick film, the thicknesses of the individual layers do not affect the formation of the intermediate phase due to the poor solubility of Mg in Cu and Cu in Mg. However, while the thicknesses of the individual layers are lower than a critical value, the reaction in the multilayer would accelerate due to the increase of the interface energy of Mg-Cu multilayer films. Figures 4-19 and 4-20 exhibit the results of the heat treatment of 40N32 and 40N14. It is obvious that Mg and Cu peaks of 40N32 vanish after 30 minutes at 423 K, as well as

Mg_2Cu formed much rapidly, suggesting that size effect accelerates the reaction of Mg and Cu. Then, 40N14, the Cu-rich multilayer, annealed at 363 K, exhibits the similar occurrence. If the thickness of the individual layer is lower than 5 nm, it can be postulated that the microstructure would be similar to 50-50. Due to very high interface energy, the diffusion-induced reaction between Mg and Cu would occur at the temperature lower than 363 K.

Concluding the previous research and these experiments, the first intermediate phase of the Mg-Cu multilayered film is always Mg_2Cu due to the localized diffusion around the interface. No other Mg-Cu intermediate phase, such as the Mg-Cu amorphous phase, was found during low-temperature annealing.

5-4 Comparison between Mg-rich and Cu-rich amorphous alloys fabricated by sputtering and liquid-quenching process

According to previous researches of Detendler et al. [70], the glass-forming composition of Mg-Cu amorphous alloy were calculated using the thermodynamic theory. In their study, Mg_2Cu with a complex orthorhombic structure is assumed not to compete with the Mg-Cu amorphous phase to simplify the difficulty in calculation during liquid-quenching. However, $MgCu_2$ with a simple face-centered cubic structure would compete with the Mg-Cu amorphous phase to induce the crystallization during liquid-quenching. Hence, the Mg-Cu amorphous alloy is believed to be different to form for a Cu-rich composition. Finally, the calculated glass-forming composition range is located $Mg_{1-x}Cu_x$ ($0.14 < x < 0.23$) [70], for example $Mg_{20}Cu_{80}$. Moreover, in addition to $MgCu_2$, the major reason why Cu-rich amorphous alloy is hard to form via liquid-quenching is that the solidus line in a Cu-rich composition is much higher than in a Mg-rich composition, leading to a higher processing temperature which implies the Cu-rich amorphous alloys need a much higher cooling rate. A large difference between the melting points of Mg and Cu is the key influencing factor for the formation of amorphous alloy via liquid-quenching. Experimentally, Mg-Cu metallic glasses can be fabricated using melting-spinning in $Mg_{1-y}Cu_y$ ($0.11 < y < 0.22$) [71], for example, $Mg_{85}Cu_{15}$.

However, the above argument becomes unsuitable for the sputtering system. There are some points different from the liquid-quenching process:

(1) Sputtering is a low-temperature process near room temperature compared with the quenching process, meaning that the process temperature in sputtering is much lower than melting-spinning.

(2) The heat gradient for the active region of the gas-solid phase transformation in sputtering is almost zero, compared with for the liquid-solid phase transformation in melt-spinning.

(3) Incident atoms are mixed with the deposited atoms near the surface continuously during sputtering, unlike atoms in the melting state freeze within the very short time during melt-spinning.

(4) The structure of the substrate influences the structure of the as-deposited films.

Due to the four different points, the properties of the specimens fabricated using the sputtering would differ from the specimens fabricated using the liquid-quenching process. It is discussed below for the discrepancy between the Mg-rich and Cu-rich amorphous alloy via the sputtering and liquid-quenching processes.

In the study of Ong et al. [72] in 2001, the XRD pattern of the as-spun $Mg_{79}Cu_{21}$ fully-amorphous ribbon by melt-spinning exhibits a hump from 33^o to 43^o as shown in Figure

5-3. Then, the XRD pattern of the as-deposited $Mg_{61.9}Cu_{38.1}$ thin film by sputtering exhibits a hump from 33^o to 44^o containing Mg_2Cu particles, as shown in Figure 4-19, which structural transformation during vacuum annealing is very similar to $Mg_{79}Cu_{21}$. In short, Mg-rich as-spun and as-deposited specimens exhibit a similar transformation of Mg_2Cu during annealing.

As mentioned above, the Cu-rich amorphous alloy is hard to form due to a necessary high cooling rate. Hence, the Cu-rich amorphous alloy via the liquid-quenching method has not been reported. Kaya and Smith [73] fabricated the $Mg_{9.7}Cu_{91.3}$ alloy via rapid quenching with an insufficient cooling rate in 1992, resulting in a Cu-$MgCu_2$ lamellar structure, as shown in Figure 5-4. However, sputtering with a high cooling rate indeed makes a possibility to form the Cu-rich amorphous alloy in this study, as shown in Figure 4-1. The high-resolution image of the $Mg_{23.5}Cu_{76.5}$ film deposited on the Si (100) wafer, as shown in Figure 4-12, reveals the $MgCu_2$ nanoparticles embedded in the Mg-Cu amorphous matrix. Additionally, Table 5-1 exhibits the thermal properties of Mg-Cu binary and Mg-Cu-X (X = Y and Gd) ternary metallic glasses. Compared with the Mg-Cu-X (X = Y and Gd) amorphous alloys, a low ΔT_x value of the $Mg_{23.5}Cu_{76.5}$ alloy represents the ability to resist crystallization during heating due to the lack of the third element to suppress the formation of $MgCu_2$ with a simple FCC structure.

Concluding speaking, sputtering is a potential process to fabricate thin film metallic glasses. However, two points of conclusions can be reached about the reasons for the difficulty in forming fully amorphous thin films using co-sputtering, as listed below.

(1) In addition to the mentioned factors during sputtering, such as the working pressure, working temperature, power of cathode, etc, the structure of the substrate plays a very important role in inducing the variation of the as-deposited film structure. The

Cu-rich co-sputtered films deposited on Si (100) wafers exhibit a partially amorphous structure. To improve the co-sputtering process, amorphous substrates, such as glass or polymer would promote the formation of fully amorphous Mg-Cu films.

(2) During co-sputtering, another important key is the power adjustment between Mg and Cu cathodes, avoiding the occurrence of the re-sputtering effect, the formation of $MgCu_2$ with the simple FCC structure and the freezing of incident atoms with insufficient residual kinetic energy.

5-5 Nano-mechanical properties of 100-150 ($Mg_{17.7}Cu_{82.3}$), 100-100 ($Mg_{23.5}Cu_{76.5}$), and 100-50 ($Mg_{40.4}Cu_{59.6}$)

For metallic glasses, the specific characteristic pop-in effect is considered to reflect the plastic deformation contributed by shear bands. As shown in Figure 5-5 [74], the load-displacement curve refers that one pop-in of three parts, as shown below,

$$\Delta h = \Delta h_{fast} + \Delta h_{slow} + \Delta h_{e}, \tag{5-5}$$

where Δh, Δh_{fast}, Δh_{slow}, and Δh_e is the overall displacement in one pop-in, the shear-band formation, the progressive plastic deformation, and the elastic deformation, respectively. In order to determine the correct pop-in size, the load-displacement curves , as shown in Figures 4-27, 4-28, and 4-29, must be modified to remove the influence of the elastic deformation (Δh_e) by Oliver-Pharr relation [64], as expressed by,

$$P = B(h - h_f)^m, \tag{5-6}$$

where P is the load applied to the test surface, h is the resulting penetration, B and m are empirically determined fitting parameters, and h_f is the final displacement after complete unloading. Then, the unloading stiffness, S, is established by analytical differentiation, as shown below.

$$\frac{dP}{dh}\Big|_{h-h_{\max}} = S = mB(h-h_f)^{m} . \tag{5-7}$$

Finally, the contact depth can be estimated using the following equation, as shown below,

$$h_c = h_l - \eta \frac{P}{S} , \tag{5-8}$$

where h_c and h_l are contact depth and the displacement in the loading part, respectively, and η is a constant depending on the indenter geometry. For Berkovich and Vicker indenters, η is 0.75.

As people know, the mechanical properties are influenced by the variation of the composition in the alloy systems, which would lead to the difference of the microstructure, especially in BMGs and the composites consisting of glassy and crystalline phases. For the co-sputtered specimens of 100-150, 100-100, and 100-50 indented at the strain rate of 5×10^{-3} s^{-1}, the modulus-displacement and hardness-displacement curves are shown in Figure 4-25.

General speaking, the deviation of the composition in a binary system, such as the Cu-Zr system, would affect the microstructure due to the variation of the glass-forming ability[75]. Then, the difference of the microstructure also affects the mechanical and thermal properties. However, in a simple binary system, such as Mg-Cu, is not suitable completely. In a simple system, the deviation of the alloy composition maybe leads to the different quantity of Mg-Cu amorphous phase and $MgCu_2$. Hence, the 100-150 and 100-100 samples exhibit similar thermal properties but dissimilar mechanical properties in the nanoindentation test.

According to Figure 4-25, the values of Young's modulus and hardness in the initial stage show a few irregular points due to the geometry of the indenter. 100-100 exhibits a higher Young's modulus and hardness in different indented depths, suggesting that the high Young's modulus is majorly contributed by $MgCu_2$. Similarly, the off-eutectic composition of the 100-50 specimen, locating in the Mg_2Cu-$MgCu_2$ eutectic region, lowers the value of the Young's modulus. Figure 4-26 presents the comparison of Young's modulus and hardness among the 100-150, 100-100, and 100-50 specimens.

It is known that an intermetallic compound typically exhibits the hard and brittle characteristics, possessing a very high Young's modulus and hardness. In the 100-100 specimens, $MgCu_2$ particles suggested be the major source provides the obstacle to constrain the movement of the shear band and finally lead to enhance the Young's modulus. As-mention above, in a simple binary Mg-Cu system, assuming that the amorphous structure of 100-150 and 100-100 is very similar, the composition difference would lead to the different quantity of the $MgCu_2$ phase in the Mg-Cu amorphous matrix. In other words, the higher Young's modulus of 100-100 than 100-150 could be due to the 100-100 specimen contains the more $MgCu_2$ phase than the 100-150 specimen, implying 100-150 is more amorphous than 100-100. Then, the plastic deformation caused by shear bands would be contributed by the sub-structure, which will be discussed below.

Figure 5-6 exhibits the different "pop-in" effects in the 100-150, 100-100 specimens. The size of the "pop-in" effect in 100-100 is smaller than those in 100-150 but more compact, suggesting the movement of shear bands might have been constrained by $MgCu_2$ nano-particles. As shown in Figures 4-12 and 4-13, the width of the Mg-Cu amorphous matrix is about 5 nm. The results of high-resolution TEM observation approximately match the sizes of the pop-in effects, indirectly proving shear bands is able to be stopped by the crystalline phases.

Comparing the mechanical properties of pure Mg and Cu, Table 5-1 compiles the Young's modulus of the Mg-Cu co-sputtered film lies between pure Mg and Cu. It is worthy to note that the Young's modulus of 100-150, 100-100, and 100-50 is close to that of Cu thin film due to the contribution of the structure of the Mg-Cu composites. Moreover, compared with Zr-, Pd-, Mg- and Cu-based BMGs, the 100-150, 100-100, and 100-50 exhibit high Young's modulus, close to those of the Zr-, Pd-, Mg- and Cu-based BMGs.

Concluding speaking, Young's modulus and hardness have a slight relation with the composition. Then, comparing Zr-, Pd-, Mg-, and Cu-based BMGs, the 100-150, 100-100, and 100-50 exhibit similar Young's modulus to Zr-, Pd-, Cu-based BMGs. In fact, the microstructure in these metallic films is the key point which influences the nano-mechanical properties.

Chapter 6 Conclusion

(1) $Mg_{1-x}Cu_x$, where x is from 38 to 82, thin films which consist of the nanocrystalline $MgCu_2$ and Mg-Cu amorphous phases are able to be fabricated by co-sputtering. In addition to liquid quenching, sputtering provides another possible path to fabricate amorphous alloys in the form of thin film.

(2) The composition variation is strongly related to the competition of the momentum and kinetic energy between Mg and Cu elements. Mg set at the RF gun provides a slower deposition rate but a compact structure, and Cu set at the DC gun provides the surface diffusion and the low-temperature continuous annealing near the localized region around the surface of the as-deposition films. Hence, Mg and Cu atom can mix each with other very well.

(3) Unbalanced competition of the momentum and kinetic energy between Mg and Cu elements would cause the irregular composition variation due to the “re-sputtering”. Besides, the absence of the surface diffusion would occur at a low power, inducing the separated nano-grains of Mg and Cu. However, the high contact surface of the nanocrystalline phase would speed up the oxidation of the film in air.

(4) In multilayered films, the first formed phase in Mg-Cu multilayered thin film is always Mg_2Cu, the most stable phase, due to a poor solubility between Mg and Cu, at any annealing temperatures.

(5) At the thick thickness of the individual layer, the thickness is unconcerned with the formation of Mg_2Cu. As the thickness of the individual layer decreases, an increasing interface energy speeds up the solid-state reaction of Mg and Cu to induce the formation of Mg_2Cu.

(6) For the Mg-Cu co-sputtering system, 100-100 ($Mg_{23.5}Cu_{76.5}$) exhibit a higher Young's modulus than 100-150 ($Mg_{17.7}Cu_{82.3}$) and 100-50 ($Mg_{40.4}Cu_{59.6}$) due to the partial amorphous structure. Moreover, the pop-in effects with a smaller size occurs of the 100-100 sample in a higher frequency than of the 100-150 and 100-50 samples. The small pop-in effects in the 100-100 sample approximate match the width of amorphous matrix via the HRTEM observation.

(7) The Mg-Cu co-sputtered thin films with the nanocrystalline $MgCu_2$ and amorphous Mg-Cu phases exhibit good nano-mechanical properties. The measured Young's modulus of 100-150, 100-100, and 100-50 is about 90~100 GPa, very close to the Zr-, Pd-, Cu-based BMGs.

References

[1] A.C. Lund, and C.A. Schuh, J. Appl. Phys., 2004, 95, 4815-4822

[2] A. Inoue, A. Kato, T. Zhang, S.G. Kim, and T. Masumoto, Mater. Trans., JIM, 1991, 32, 606-609

[3] J. Schroers, and N. Paton, Adv. Mater. Processes, 2006, 61-63

[4] P. Sharma, W. Zhang, K. Amiya, H. Kimura, and A. Inoue, Nanoscience and Nanotech., 2005, 5, 416-420

[5] T. Fukushige, S. Hata, and A. Shimokohbe, J. Microelectromech. Syst., 2005, 14, 243-253

[6] A. Inoue, Mater. Sci. Eng. A, 2001, 304-306, 1-10

[7] A. Inoue, Acta Metar., 2000, 48, 279-306

[8] F.W. Zhu, Z.G. Zhai, and G.H. Yu, J. Univ. Sci. Technol. Beijing, 2003, 10, 1-8

[9] S. Bysakh, P.K. Das, and K. Chattopadhyay, Philos. Mag. A, 2001, 81, 2689-2704

[10] R.B. Schwarz, and W.L. Johnson, Phys. Rev. Lett., 1983, 51, 415-418

[11] S. Hata, K. Sato, and A. Shimokohbe, Proc. SPIE, 1999, 3892, 97-108

[12] J.P. Chu, C.T. Liu, T. Mahalingam, S.F. Wang, M.J. O'Keefe, B. Johnson, and C.H. Kuo, Phys. Rev. B, 2004, 69, 1333410-1 - 113410-4

[13] Y. Liu, S. Hata, K. Wada, and A. Shimokohbe, Jpn. J. Appl. Phys., 2001, 40, 5382-5388

[14] A. Paesano, E.Y. Honda, M.A. Rocha, J.B.M.d. Cunha, and B. Hallouche, Thin Solid Films, 2004, 458, 165-172

[15] E. Magni, and G.A. Somorjai, Appl. Surf. Sci., 1995, 89, 187-195

[16] W.J. DeSisto, and R.L. Henry, J. Cryst. Growth, 1991, 109, 314-317

[17] T.J. Zhu, L. Lu, and X.B. Zhao, Mater. Sci. Eng., B, 2006, 129, 96-99

[18] C.B. Eom, M.K. Lee, J.H. Choi, L. Belenky, X. Song, L.D. Cooley, M.T. Naus, S. Patnaik, J. Jiang, M. Rikel, A. Polyanskii, A. Gurevich, X.Y. Cai, S.D. Bu, S.E. Babcock, E.E. Hellstrom, D.C. Larbalestier, N. Rogado, K.A. Regan, M.A. Hayward, T. He, J.S. Slusky, I. K, M.K. Haas, and R.J. Cava, Nature, 2001, 411, 558-660

[19] Y. Harada, T. Takahashi, H. Iriuda, M. Kuroha, Y. Nakanishi, and M. Yoshuzawa, Physica C, 2005, 426-431, 1453-1458

[20] K. Higuchi, H. Kajioka, K. Toiyama, H. Fujii, S. Orimo, and Y. Kikuchi, J. Alloys Compd., 1999, 293~295, 484-489

[21] K. Higuchi, K. Yamamoto, H. Kajioka, K. Toiyama, M. Honda, S. Orimo, and H. Fujii, J. Alloys Compd., 2002, 330~332, 526-530

[22] B. Darriet, M. Pezat, A. Hbika, and P. Hagenmulifr, Int. J. Hydrogen Energy, 1979, 5, 173-178

[23] P. Selvam, B. Viswanathan, C.S. Swamy, and V. Srinivasan, Int. J. Hydrogen Energy, 1985, 11, 169-192

[24] W. Klement, R.H. Willens, and P. Duwez, Nature, 1960, 187, 869-870

[25] H.S. Chen, and D. Turnbull, Acta Metar., 1969, 17, 1021-1031

[26] H.S. Chen, Acta Metar., 1974, 22, 1050-1511

[27] E.J. Cotts, W.J. Meng, and W.L. Johnson, Phys. Rev. Lett., 1986, 57, 2295-2298

[28] H.W. Kui, A.L. Greer, and D. Turnbull, Appl. Phys. Lett., 1984, 45, 615-616

[29] Q.M. Chen, Y.D. Fan, and H.D. Li, Mater. Lett. , 1988, 6, 311-315

[30] J. Dudonis, R. Brucas, and A. Miniotas, Thin Solid Films, 1996, 275, 164-167

[31] J. Sakurai, S. Hata, and A. Shimokohbe, International Conference on Advanced Technology in Experimental Mechanics 2003, 2003, 10-12

[32] G.P. Zhang, Y. Liu, W. Wang, and J. Tan, Appl. Phys. Lett., 2006, 88, 013105-1 - 013105-3

[33] G.P. Zhang, Y. Liu, and B. Zhang, Scripta Mater., 2006, 54, 897-901

[34] R. Yamauchu, S. Hata, J. Sakurai, and A. Shimokohbe, Mater. Res. Soc, Symp. Proc., 2006, 894, 0894-LL02-05.1-0894-LL02-05.5

[35] S. Hata, T. Fukushige, and A. Shimokohbe, Proceedings of CPT2002, 2002, 162-167

[36] G.P. Zhang, Y. Liu, and B. Zhang, Adv. Eng. Mater., 2005, 7, 606-609

[37] A. Blatter, and M.V. Allmen, Phys. Rev. Lett., 1985, 54, 2103-2106

[38] H. Hahn, and R.S. Averback, Phys. Rev. B, 1988, 37, 6533-6535

[39] S.B. Newcomb, and K.N. Tu, Appl. Phys. Lett., 1986, 48, 1436-1438

[40] B.X. Liu, Mater. Lett., 1987, 5, 322-327

[41] Z.Z. Tang, J.H. Hsieh, S.Y. Zhang, C. Li, and Y.Q. Fu, Surf. Coat. Technol., 2005, 198, 110-113

[42] P.F. Ladwig, and Y.A. Chang, J. Appl. Phys., 2003, 94, 979-987

[43] 吳學陞，工業材料, 1999, 149, 154-165

[44] W. Buckel, Z. Phys., 1954, 138, 136

[45] A. Inoue, T. Nakamura, and N. Nishiyama, Mater. Trans., JIM, 1992, 33, 937-945

[46] Z.P. Lu, H. Tan, Y. Li, and S.C. Ng, Scripta Mater., 2000, 42, 667-673

[47] Z.P. Lu, and C.T. Liu, Acta Metar., 2002, 50, 3501-3512

[48] A. Inoue, T. Zhang, and Tsuyoshi, Mater. Trans., JIM, 1989, 30, 965-972

[49] Z.P. Lu, and C.T. Liu, Intermetallics, 2004, 12, 1035-1043

[50] K. Seshan, Handbook of Thin-Film Deposition Processes and Techniques, 2002

[51] D.M. Mattox, Handbook of Physical Vapor Deposition (PVD) Processing, 1998

[52] K. Wasa, and S. Hayakawa, Handbook of Sputter Deposition Technology, 1992

[53] W. Zou, Synthesis of Giant Magnetoresistive Multilayers, 2001

[54] M. Ohring, The Material Science of Thin Films, 1992

[55] S. Hata, J. Sakurai, and A. Shimokohbe, MEMS, 18th IEEE International Conference, 2005, 479-482

[56] G.S. Chen, and S.T. Chen, J. Appl. Phys., 2000, 87, 8473-8482

[57] L. Ding, P.F. Ladwig, X.Y. Yan, and Y.A. Chang, Appl. Phys. Lett., 2002, 80, 1186-1188

[58] H. Bakker, G.F. Zhou, and H. Yang, Prog. Mater. Sci., 1995, 39, 159-241

[59] P.J. Hsieh, J.C. Huang, Y.P. Hung, S.I. Chou, and J.S.C. Jang, Mater. Chem. Phys., 2004, 88, 364-376

[60] G.Y. Yuan, K. Amiya, and A. Inoue, J. Non-Cryst. Solids, 2005, 351, 729-735

[61] J.P. Chu, and C.T. Lo, Appl. Phys. Lett., 2006, 88, 1-3

[62] B. Arcot, S.P. Murarka, L.A. Clevenger, Q.Z. Hong, W. Ziegler, and J.M.E. Harper, J. Appl. Phys., 1994, 76, 5161-5170

[63] J. Rodriguez-Viejo, M. Gonzalez-Silvera, and M.T. Clavaguera-Mora, J. Appl. Phys., 2003, 93, 4447-4453

[64] W.C. Oliver, and G.M. Pharr, J. Mater. Res., 1992, 7, 1564-1583

[65] H. Somekawa, T.G. Neih, and K. Higashi, Scripta Mater., 2004, 50, 1361-1365

[66] X.Y. Chou, Z.D. Jiang, H.R. Wang, and Q. Zhu, J. Phys. Conf. Ser., 2006, 48, 1096-1101

[67] R. Steiner, H.-G. Boyen, M. Krieger, A. Plettl, P. Widmayer, P. Ziemann, F. Banhat, R. Kilper, and P. Oelhafen, Appl. Phys. A, 2003, 76, 5-13

[68] Q.Z. Hong, and F.M. d'Heurle, J. Appl. Phys., 1992, 72, 4036-4040

[69] M. Gonzalez-Silveira, J. Rodriguez-Viejo, G. Garcia, F. Pi, F.J. Ager, J.L. Labar, A. Barna, M. Menyhard, and L. Kotis, J. Appl. Phys., 2006, 100, 113522-1 - 113522-9

[70] R.H. Detendler, J.A. Kovacs, and J.A. Alonso, J. Mater. Sci., 1992, 27, 4935-4939

[71] A.T.W. Kenpen, H. Nitsche, F. sommer, and E.J. Mittemeijer, Metall. Mater. Trans. A, 2002, 33A, 1041-1050

[72] M.S. Ong, Y. Li, D.J. Blackwood, and S.C. Ng, Mater. Sci. Eng. A, 2001, 304-306, 510-514

[73] M. Kaya, and R.W. Smith, J. Mater. Sci, 1992, 27, 2258-2266

[74] Z. Kovacs, A. Castelero, A.L.Greer, J. Lendvai, and M. Baricco, Mater. Sci. Eng. A, 2004, 387-389, 1012-1017

[75] D. Wang, Y. Li, B.B. Sun, M.L. Sui, K. Lu, and E. Ma, Appl. Phys. Let., 2004, 84, 4029-4031

[76] H. Men, W.T. Kim, and D.H. Kim, J. Non-cryst. Alloys, 2004, 337, 29-35

[77] L. Charleux, S. Gravier, M. Verdier, M. Fivel, and J.J. Blandin, J. Mater. Res., 2007, 22, 525-532

[78] A.L. Greer, A. Castellero, S.V. Madge, I.T. Walker, and J.R. Wilde, Mater. Sci. Eng. A, 2004, 375-377, 1182-1185

[79] A. Castellero, S.J. Lloyd, S.V. Madge, Z. Kovacs, J.F. Loffler, M. Baroccp, and A.L. Greer, J. Alloys Compd., 2007, 434-435, 48-51

[80] A. Concustell, G. Alcala, S. Mato, T.G. Woodcock, A. Gebert, J. Eckert, and M.D. Baro, Intermetallics, 2005, 13, 1214-1219

[81] J.H. Zhao, Y. Du, M. Morgen, and P.S. Ho, J. Appl. Phys., 2000, 87, 1575-1577

[82] X. Deng, C. Cleveland, T. Karcher, M. Koopman, N. Chawla, and K.K. Chawla, J. Mater. Eng. Perform., 2005, 14, 417-423

Table 1-1 Functional properties and application fields of bulk amorphous and nanocrystalline alloys [6].

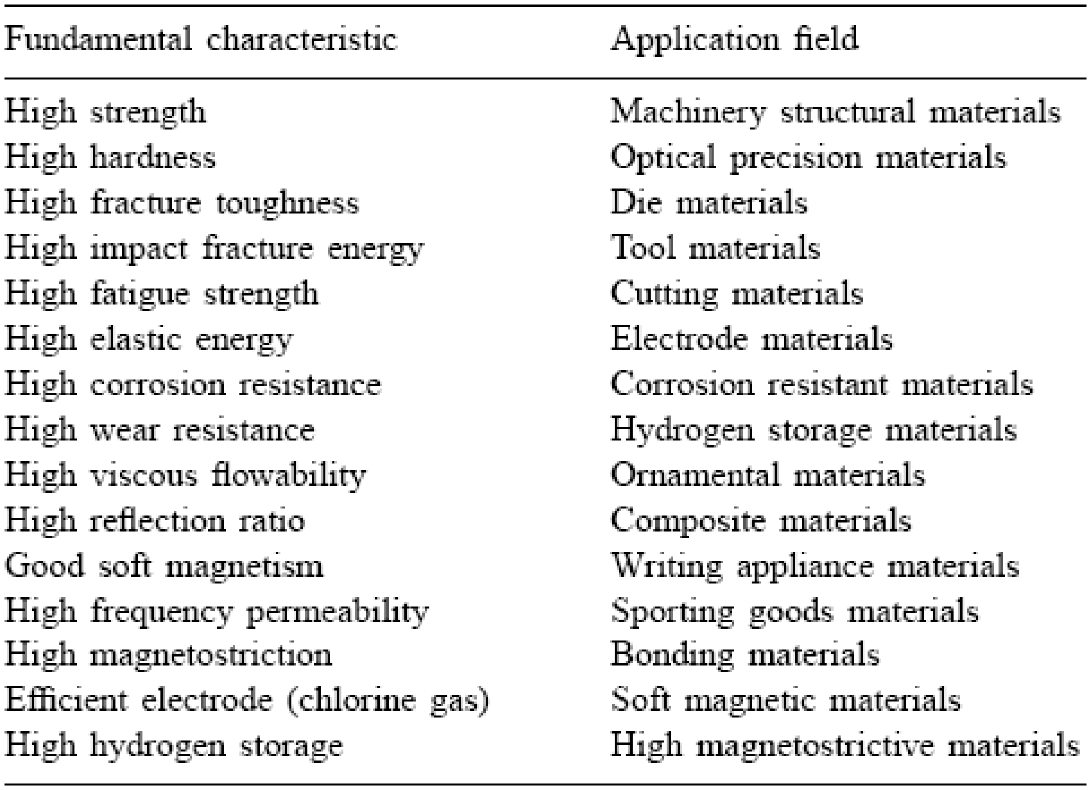

Fundamental characteristic	Application field
High strength	Machinery structural materials
High hardness	Optical precision materials
High fracture toughness	Die materials
High impact fracture energy	Tool materials
High fatigue strength	Cutting materials
High elastic energy	Electrode materials
High corrosion resistance	Corrosion resistant materials
High wear resistance	Hydrogen storage materials
High viscous flowability	Ornamental materials
High reflection ratio	Composite materials
Good soft magnetism	Writing appliance materials
High frequency permeability	Sporting goods materials
High magnetostriction	Bonding materials
Efficient electrode (chlorine gas)	Soft magnetic materials
High hydrogen storage	High magnetostrictive materials

Table 2-1 The classification of amorphous alloy systems [7].

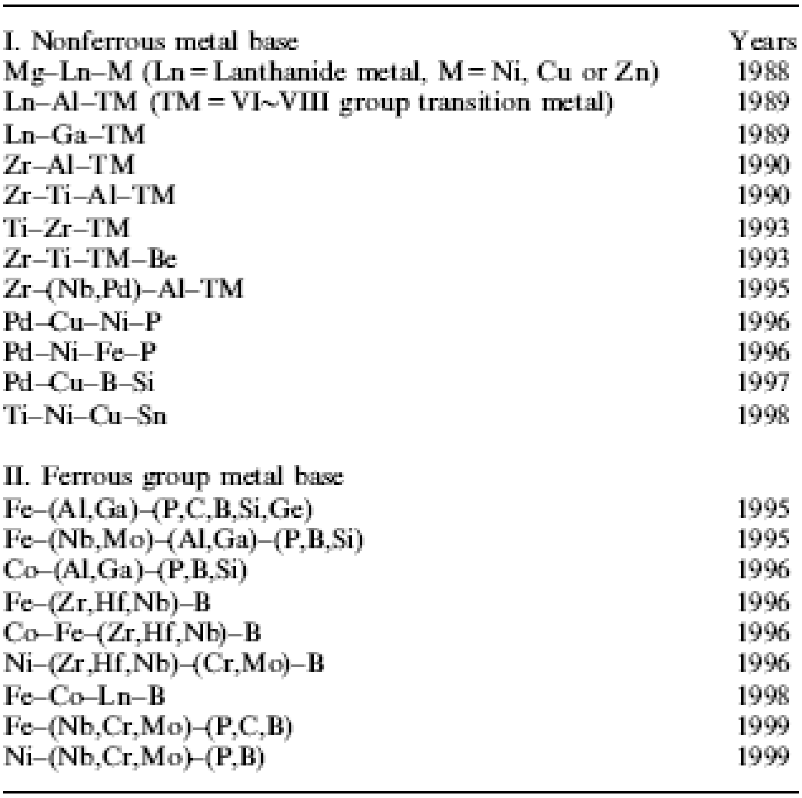

I. Nonferrous metal base	Years
Mg–Ln–M (Ln = Lanthanide metal, M = Ni, Cu or Zn)	1988
Ln–Al–TM (TM = VI~VIII group transition metal)	1989
Ln–Ga–TM	1989
Zr–Al–TM	1990
Zr–Ti–Al–TM	1990
Ti–Zr–TM	1993
Zr–Ti–TM–Be	1993
Zr–(Nb,Pd)–Al–TM	1995
Pd–Cu–Ni–P	1996
Pd–Ni–Fe–P	1996
Pd–Cu–B–Si	1997
Ti–Ni–Cu–Sn	1998
II. Ferrous group metal base	
Fe–(Al,Ga)–(P,C,B,Si,Ge)	1995
Fe–(Nb,Mo)–(Al,Ga)–(P,B,Si)	1995
Co–(Al,Ga)–(P,B,Si)	1996
Fe–(Zr,Hf,Nb)–B	1996
Co–Fe–(Zr,Hf,Nb)–B	1996
Ni–(Zr,Hf,Nb)–(Cr,Mo)–B	1996
Fe–Co–Ln–B	1998
Fe–(Nb,Cr,Mo)–(P,C,B)	1999
Ni–(Nb,Cr,Mo)–(P,B)	1999

Table 2-2 The classification of amorphous alloy systems [7].

I	ETM (or Ln) + Al + LTM	Zr-Al-Ni, Zr-Al-Cu, Zr-Al-Ni-Cu, Zr-Ti-Al-Ni-Cu, Zr-Nb-Al-Ni-Ln, Zr-Ga-Ni
		Ln-Al-Ni, Ln-Al-Cu, Ln-Al-Ni-Cu, Ln-Ga-Ni, Ln-Ga-Nb-B
II	LTM + ETM + Metalloid	Fe-Zr-B, Fe-Hf-B, Fe-Zr-Hf-B, Fe-Co-Ln-B, Co-Zr-Nb-B
III	LTM (Fe) + Al or Ga + Metalloid	Fe- (Al, Ga)- Metalloid
IV	Mg + Ln + LTM	Mg-Ln-Ni, Mg-Ln-Cu
	TM (Zr ot Ti) + Be + LTM	Zr-Ti-Be-Ni-Cu
V	LTM + Metalloid	Pd-Ni-P, Pd-Cu-Ni-P, Pt-Ni-P

Table 2-3 Prediction and observation of metallic glass formation by ion mixing in binary metal systems [40].

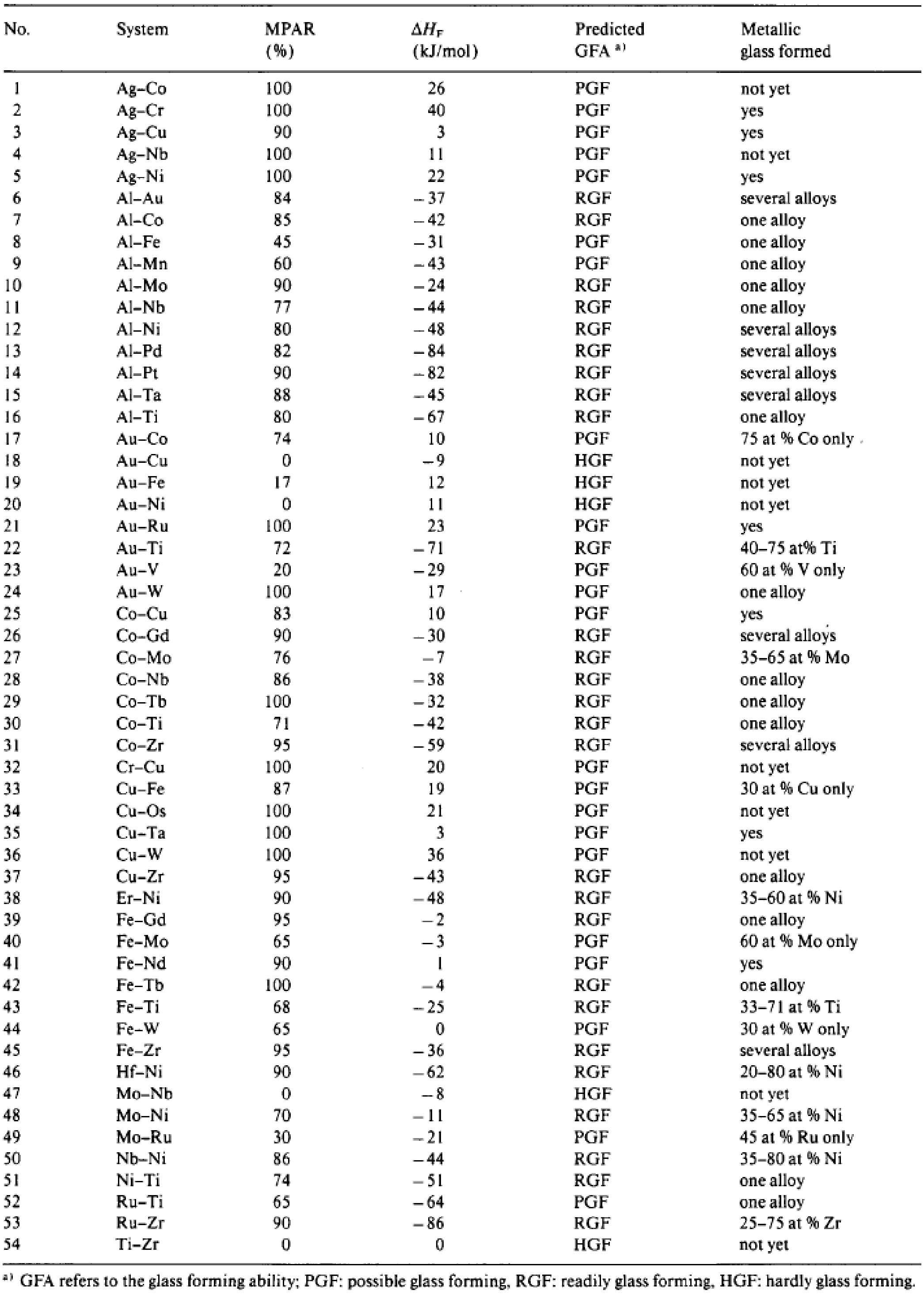

No.	System	MPAR (%)	ΔH_F (kJ/mol)	Predicted GFA [a]	Metallic glass formed
1	Ag–Co	100	26	PGF	not yet
2	Ag–Cr	100	40	PGF	yes
3	Ag–Cu	90	3	PGF	yes
4	Ag–Nb	100	11	PGF	not yet
5	Ag–Ni	100	22	PGF	yes
6	Al–Au	84	−37	RGF	several alloys
7	Al–Co	85	−42	RGF	one alloy
8	Al–Fe	45	−31	PGF	one alloy
9	Al–Mn	60	−43	PGF	one alloy
10	Al–Mo	90	−24	RGF	one alloy
11	Al–Nb	77	−44	RGF	one alloy
12	Al–Ni	80	−48	RGF	several alloys
13	Al–Pd	82	−84	RGF	several alloys
14	Al–Pt	90	−82	RGF	several alloys
15	Al–Ta	88	−45	RGF	several alloys
16	Al–Ti	80	−67	RGF	one alloy
17	Au–Co	74	10	PGF	75 at % Co only
18	Au–Cu	0	−9	HGF	not yet
19	Au–Fe	17	12	HGF	not yet
20	Au–Ni	0	11	HGF	not yet
21	Au–Ru	100	23	PGF	yes
22	Au–Ti	72	−71	RGF	40–75 at% Ti
23	Au–V	20	−29	PGF	60 at % V only
24	Au–W	100	17	PGF	one alloy
25	Co–Cu	83	10	PGF	yes
26	Co–Gd	90	−30	RGF	several alloys
27	Co–Mo	76	−7	RGF	35–65 at % Mo
28	Co–Nb	86	−38	RGF	one alloy
29	Co–Tb	100	−32	RGF	one alloy
30	Co–Ti	71	−42	RGF	one alloy
31	Co–Zr	95	−59	RGF	several alloys
32	Cr–Cu	100	20	PGF	not yet
33	Cu–Fe	87	19	PGF	30 at % Cu only
34	Cu–Os	100	21	PGF	not yet
35	Cu–Ta	100	3	PGF	yes
36	Cu–W	100	36	PGF	not yet
37	Cu–Zr	95	−43	RGF	one alloy
38	Er–Ni	90	−48	RGF	35–60 at % Ni
39	Fe–Gd	95	−2	RGF	one alloy
40	Fe–Mo	65	−3	PGF	60 at % Mo only
41	Fe–Nd	90	1	PGF	yes
42	Fe–Tb	100	−4	RGF	one alloy
43	Fe–Ti	68	−25	RGF	33–71 at % Ti
44	Fe–W	65	0	PGF	30 at % W only
45	Fe–Zr	95	−36	RGF	several alloys
46	Hf–Ni	90	−62	RGF	20–80 at % Ni
47	Mo–Nb	0	−8	HGF	not yet
48	Mo–Ni	70	−11	RGF	35–65 at % Ni
49	Mo–Ru	30	−21	PGF	45 at % Ru only
50	Nb–Ni	86	−44	RGF	35–80 at % Ni
51	Ni–Ti	74	−51	RGF	one alloy
52	Ru–Ti	65	−64	PGF	one alloy
53	Ru–Zr	90	−86	RGF	25–75 at % Zr
54	Ti–Zr	0	0	HGF	not yet

[a] GFA refers to the glass forming ability; PGF: possible glass forming, RGF: readily glass forming, HGF: hardly glass forming.

Table 2-4 Zone structures in thick evaporated and sputtered coating [51].

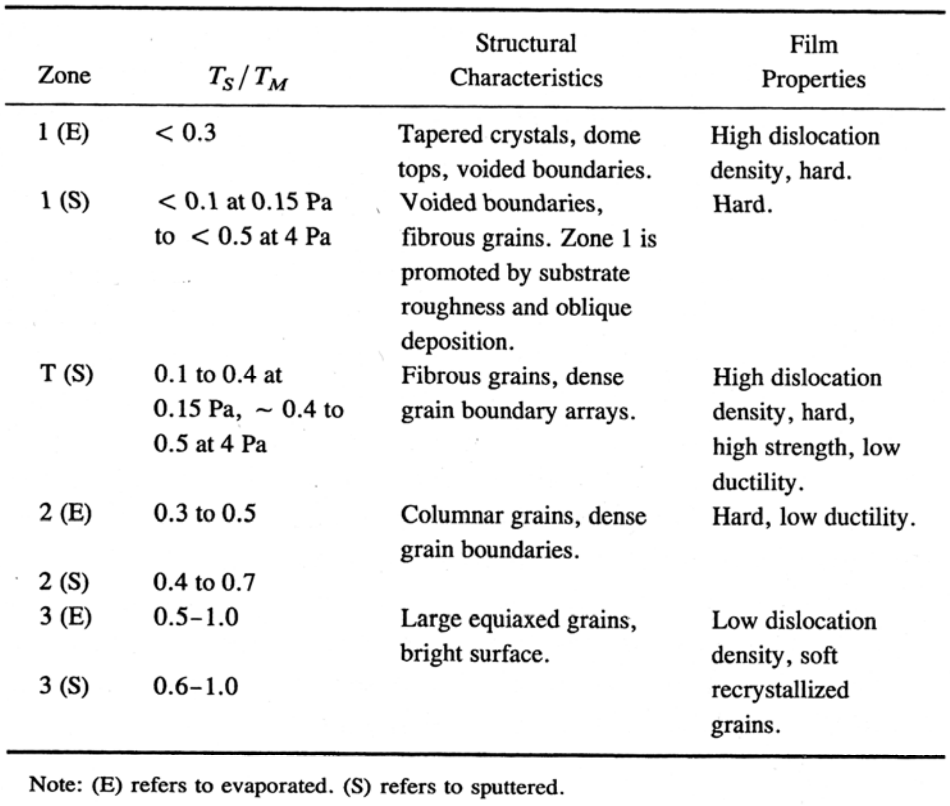

Zone	T_S / T_M	Structural Characteristics	Film Properties
1 (E)	< 0.3	Tapered crystals, dome tops, voided boundaries.	High dislocation density, hard.
1 (S)	< 0.1 at 0.15 Pa to < 0.5 at 4 Pa	Voided boundaries, fibrous grains. Zone 1 is promoted by substrate roughness and oblique deposition.	Hard.
T (S)	0.1 to 0.4 at 0.15 Pa, ~ 0.4 to 0.5 at 4 Pa	Fibrous grains, dense grain boundary arrays.	High dislocation density, hard, high strength, low ductility.
2 (E)	0.3 to 0.5	Columnar grains, dense grain boundaries.	Hard, low ductility.
2 (S)	0.4 to 0.7		
3 (E)	0.5–1.0	Large equiaxed grains, bright surface.	Low dislocation density, soft recrystallized grains.
3 (S)	0.6–1.0		

Note: (E) refers to evaporated. (S) refers to sputtered.

Table 2-5 Structure phase and ductility of Pd-TFMG made by different types of target at different Ar pressures [13].

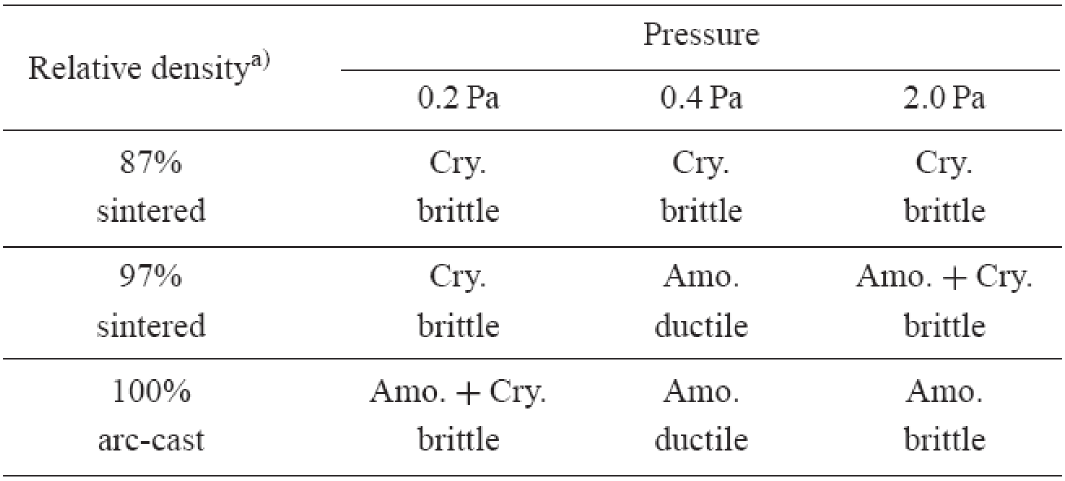

Relative density$^{a)}$	Pressure		
	0.2 Pa	0.4 Pa	2.0 Pa
87% sintered	Cry. brittle	Cry. brittle	Cry. brittle
97% sintered	Cry. brittle	Amo. ductile	Amo. + Cry. brittle
100% arc-cast	Amo. + Cry. brittle	Amo. ductile	Amo. brittle

Table 2-6 T_g, T_x and resistivity of Pd-TFMG made by arc-cast target at different Ar pressures [13].

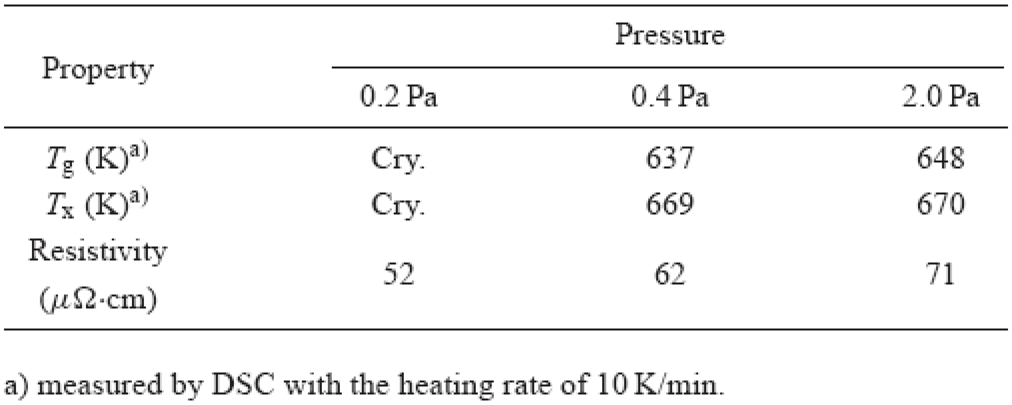

Property	Pressure		
	0.2 Pa	0.4 Pa	2.0 Pa
T_g (K)$^{a)}$	Cry.	637	648
T_x (K)$^{a)}$	Cry.	669	670
Resistivity ($\mu\Omega\cdot$cm)	52	62	71

a) measured by DSC with the heating rate of 10 K/min.

Table 2-7 Properties of Pd-TFMG and bulk metallic glass [13].

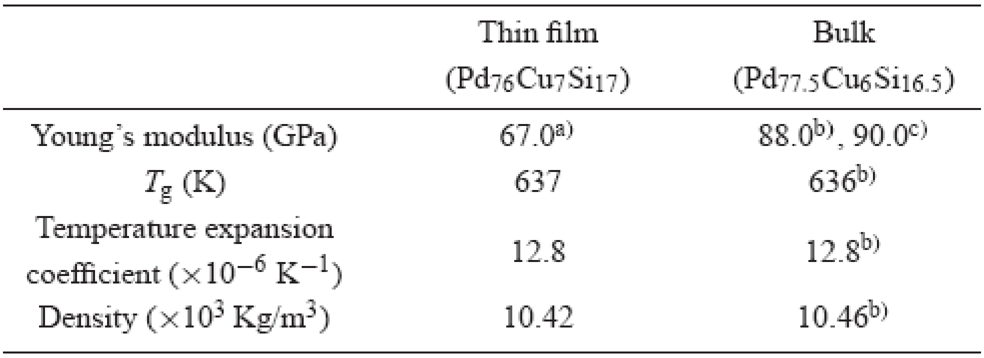

	Thin film ($Pd_{76}Cu_7Si_{17}$)	Bulk ($Pd_{77.5}Cu_6Si_{16.5}$)
Young's modulus (GPa)	67.0[a)]	88.0[b)], 90.0[c)]
T_g (K)	637	636[b)]
Temperature expansion coefficient ($\times 10^{-6}$ K^{-1})	12.8	12.8[b)]
Density ($\times 10^3$ Kg/m^3)	10.42	10.46[b)]

Table 2-8 Electrical resistivity of the thin film metallic glasses and conventional electrical device materials [31].

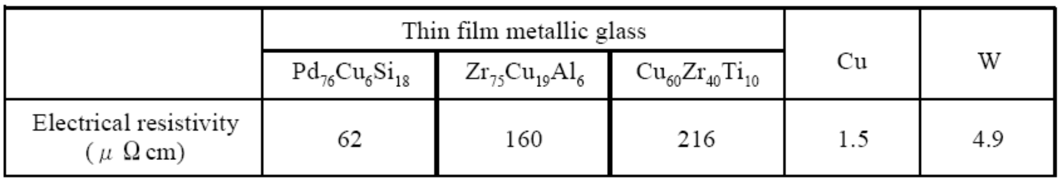

	Thin film metallic glass			Cu	W
	$Pd_{76}Cu_6Si_{18}$	$Zr_{75}Cu_{19}Al_6$	$Cu_{60}Zr_{40}Ti_{10}$		
Electrical resistivity (μ Ωcm)	62	160	216	1.5	4.9

Table 3-1 The details of the co-deposition conditions.

Materials	Mg	Cu
Power	RF power 100 and 50 W	DC power 150, 100, 50, 25, and 15 W
Pre-sputtering time	1 min	
Working pressure	3×10^{-3} torr	
Argon flow rate	30 sccm	

Table 3-2 The details of multilayer sputtering conditions.

Material	Mg individual layer	Cu individual layer
Power	RF 100 W	DC 150 W
Pre-sputtering time	1 min	1 min
Working pressure	3×10^{-3} torr	
Argon flow rate	30 sccm	
Deposition rate	10 nm/min	40 nm/min

Table 3-3 The information of the Mg-Cu multilayered films.

Sample	Thickness of individual layers (nm)				Thickness ratio				Calculated atomic ratio			
20T32	Mg	**150**	Cu	**50**	Mg	**3**	Cu	**1**	Mg	**3**	Cu	**2**
40N32	Mg	**15**	Cu	**5**	Mg	**3**	Cu	**1**	Mg	**3**	Cu	**2**
20T14	Mg	**100**	Cu	**200**	Mg	**1**	Cu	**2**	Mg	**1**	Cu	**4**
40N14	Mg	**10**	Cu	**20**	Mg	**1**	Cu	**2**	Mg	**1**	Cu	**4**

Table 3-4 The information of the Mg-Cu co-sputtered films

	Sample	Deposition condition			
100 series	**100-150**	Mg	**RF 100 W**	Cu	**DC 150 W**
	100-100	Mg	**RF 100 W**	Cu	**DC 100 W**
	100-50	Mg	**RF 100 W**	Cu	**DC 50 W**
	100-25	Mg	**RF 100 W**	Cu	**DC 25 W**
	100-15	Mg	**RF 100 W**	Cu	**DC 15 W**
50 series	**50-150**	Mg	**RF 50 W**	Cu	**DC150 W**
	50-100	Mg	**RF 50 W**	Cu	**DC 50 W**
	50-50	Mg	**RF 50 W**	Cu	**DC 50 W**
	50-25	Mg	**RF 50 W**	Cu	**DC 25 W**

Table 4-1 The composition of the Mg-Cu co-sputtered films

specimen		Composition (at%)					
100 series	**100-150**	Mg	**17.7**	Cu	**82.3**	O	**0**
	100-100	Mg	**23.5**	Cu	**76.5**	O	**0**
	100-50	Mg	**40.4**	Cu	**59.6**	O	**0**
	100-25	Mg	**61.9**	Cu	**38.1**	O	**0**
	100-15	Mg	**39.9**	Cu	**43.5**	O	**16.6**
50 series	**50-150**	Mg	**0**	Cu	**100**	O	**0**
	50-100	Mg	**0**	Cu	**100**	O	**0**
	50-50	Mg	**10.1**	Cu	**89.9**	O	**0**
	50-25	Mg	**15.6**	Cu	**63.9**	O	**20.5**

Table 4-2 Structural and compositional comparison between Mg-Cu co-sputtered and multilayered thin films

Type	Specimen			composition	Situation	Structure	Oxidation
Co-sputtered	50 series	Cu-rich	50-150	Pure Cu	As-deposited	Nanocrystalline Cu	No
			50-100	Pure Cu	As-deposited	Nanocrystalline Cu	No
			50-50	$Mg_{10.1}Cu_{89.9}$	As-deposited	Nanocrystalline Mg and Cu	No
			50-25	$Mg_{15.6}Cu6_{3.9}O_{20.5}$	As-deposited	Nanocrystalline Mg and Cu	Yes
	100 series	Cu-rich	100-150	$Mg_{17.7}Cu_{82.3}$	As-deposited	Amorphous with Nanocrystalline $MgCu_2$	No
					Annealing	Nanocrystalline $MgCu_2$	No
			100-100	$Mg_{23.5}Cu_{76.5}$	As-deposited	Amorphous with Nanocrystalline $MgCu_2$	No
					Annealing	Nanocrystalline $MgCu_2$	No
			100-50	$Mg_{40.4}Cu_{59.6}$	As-deposited	Amorphous with Nanocrystalline $MgCu_2$	No
					Annealing	Nanocrystalline $MgCu_2$	No
		Mg-rich	100-25	$Mg_{61.9}Cu_{38.1}$	As-deposited	Nanocrystalline Mg_2Cu with amorphous	No
					Annealing	Nanocrystalline Mg_2Cu	No
		Mg-rich	100-15	$Mg_{39.9}Cu_{43.5}O_{16.6}$	As-deposited	Nanocrystalline Mg_2Cu	Yes
Multilayered		Cu-rich	20T14 & 40N14		As-deposited	Nanocrystalline Mg and Cu	No
					Annealing	Nanocrystalline Mg_2Cu	No
		Mg-rich	20T32 & 40N32		As-deposited	Nanocrystalline Mg and Cu	No
					Annealing	Nanocrystalline Mg_2Cu	No

Table 5-1 Comparison between thermal properties of Mg-based binary and ternary amorphous alloys.

Alloys	Sample type	Structure	T_g (K)	T_x (K)	ΔT_x (K)
$Mg_{65}Cu_{25}Gd_{10}$ [76]	Bulk	Fully amorphous	408	478	60
$Mg_{65}Cu_{25}Y_{10}$ [76]	Bulk	Fully amorphous	413	473	70
$Mg_{23.5}Cu_{76.5}$	Thin film	Partial amorphous	425	460	35
$Mg_{17.7}Cu_{82.3}$	Thin film	Partial amorphous	428	460	32

Table 5-2 Comparison between Values of Young's modulus and hardness from published nanoindentation works and this study.

Meterials	Sample Type	Young's modulus (GPa)	Hardness (GPa)
$Zr_{41.2}5Ti_{13.75}Cu_{12.5}Ni_{10}Be_{22.5}$ [77]	Bulk	96	7.3
$Zr_{60}Cu_{20}Pd_{10}Al_{10}$ [78]	Bulk	87	5.7
$Pd_{40}Ni_{40}P_{20}$ [78]	Bulk	108	5.5
$Mg_{65}Ni_{20}Nd_{15}$ [78]	Bulk	57	3.4
$Mg_{60}Cu_{30}Y_{10}$ [79]	Bulk	51.5	3.3
$Cu_{60}Zr_{22}Ti_{18}$ [80]	Bulk	104.7	6.6
Pure Mg	Bulk	45^{*}	x
Pure Cu	Thin film	104 [81]	x
Al-SiC multilayer [82]	Thin film	71	2.4
100-150 ($Mg_{17.7}Cu_{82.3}$)	Thin film	100.1	3.6
100-100 ($Mg_{23.5}Cu_{76.5}$)	Thin film	118	4.6
100-50 ($Mg_{40.4}Cu_{59.6}$)	Thin film	96.8	4.3

* The normal Young's modulus value of the Mg bulk.

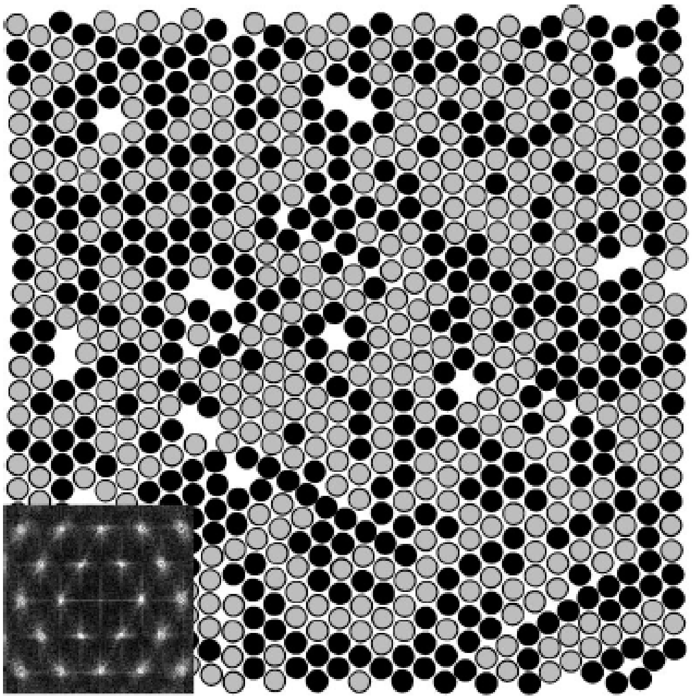

Figure 1-1 A scheme of long-range-ordered structure [1].

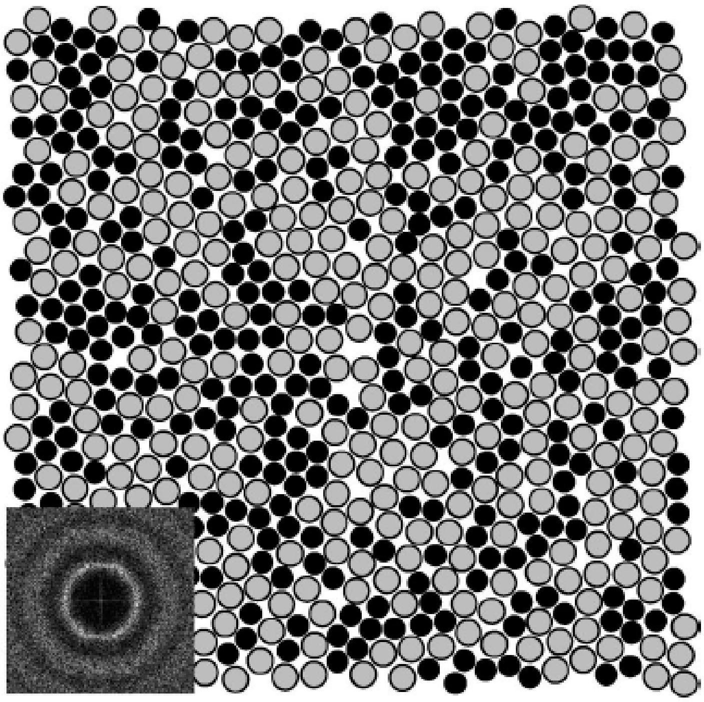

Figure 1-2 A scheme of short-range-ordered structure [1].

Figure 1-3 The frame for the upscale models of the Vertu mobile phone is made of liquid-metal alloy because of its high strength, hardness, and scratch resistance[3].

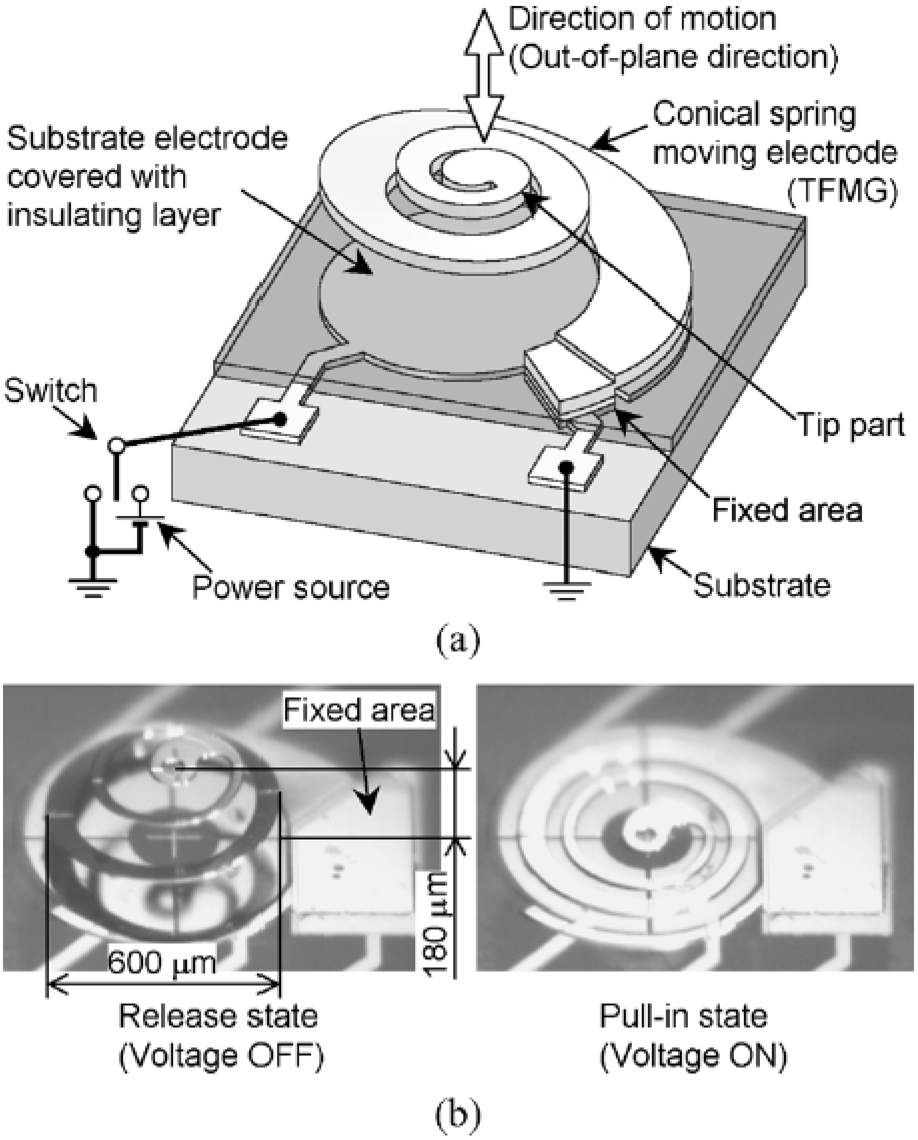

Fig. 1. Conical spring microactuator. (a) Fundamental structure and (b) micrographs.

Figure 1-4 (a) A sketch of conical spring microactuator, and (b) a fundamental structure of micro-switch made by metallic glass thin films [5].

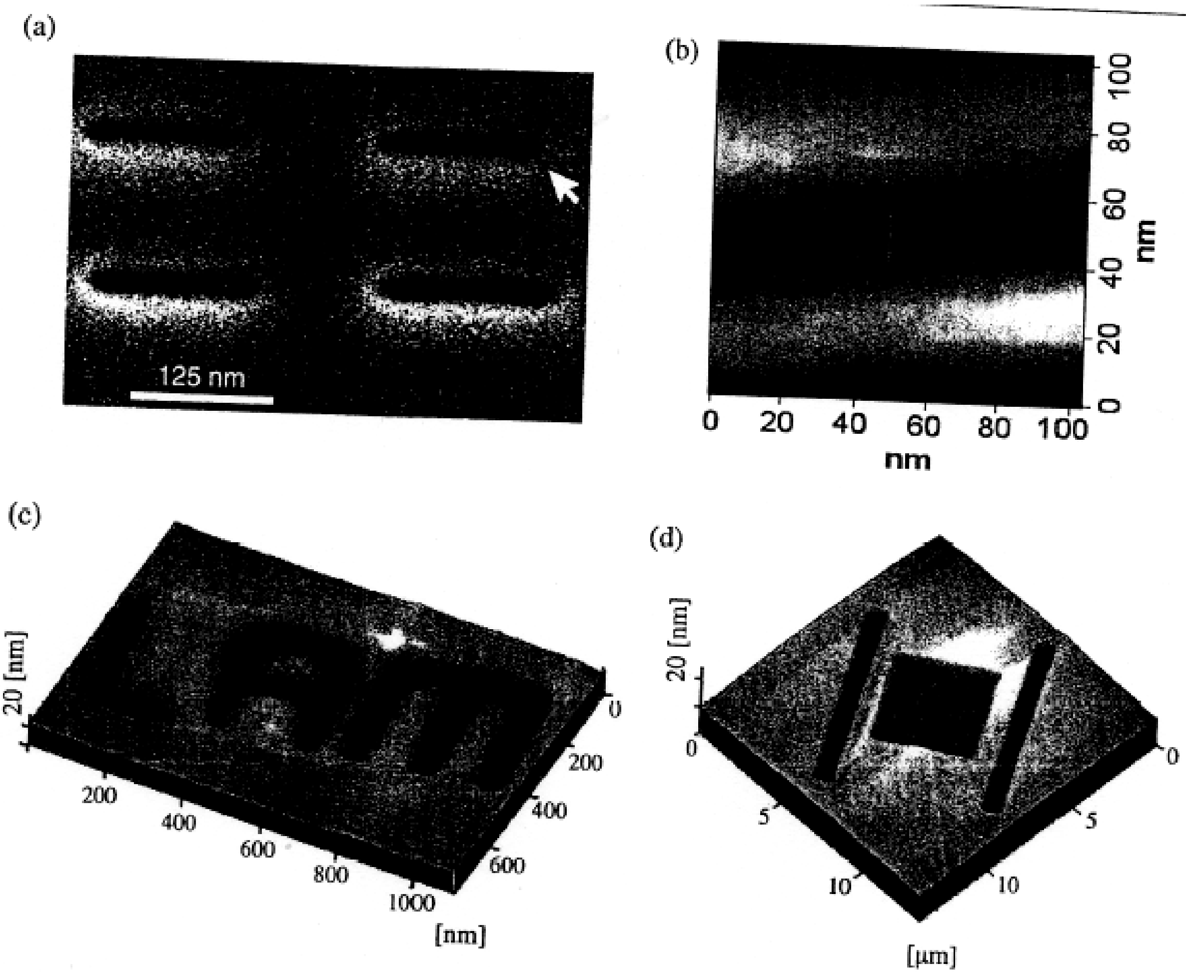

Figure 1-5 FIB nanomold on completely glassy Zr-Al-Cu-Ni thin films [4].

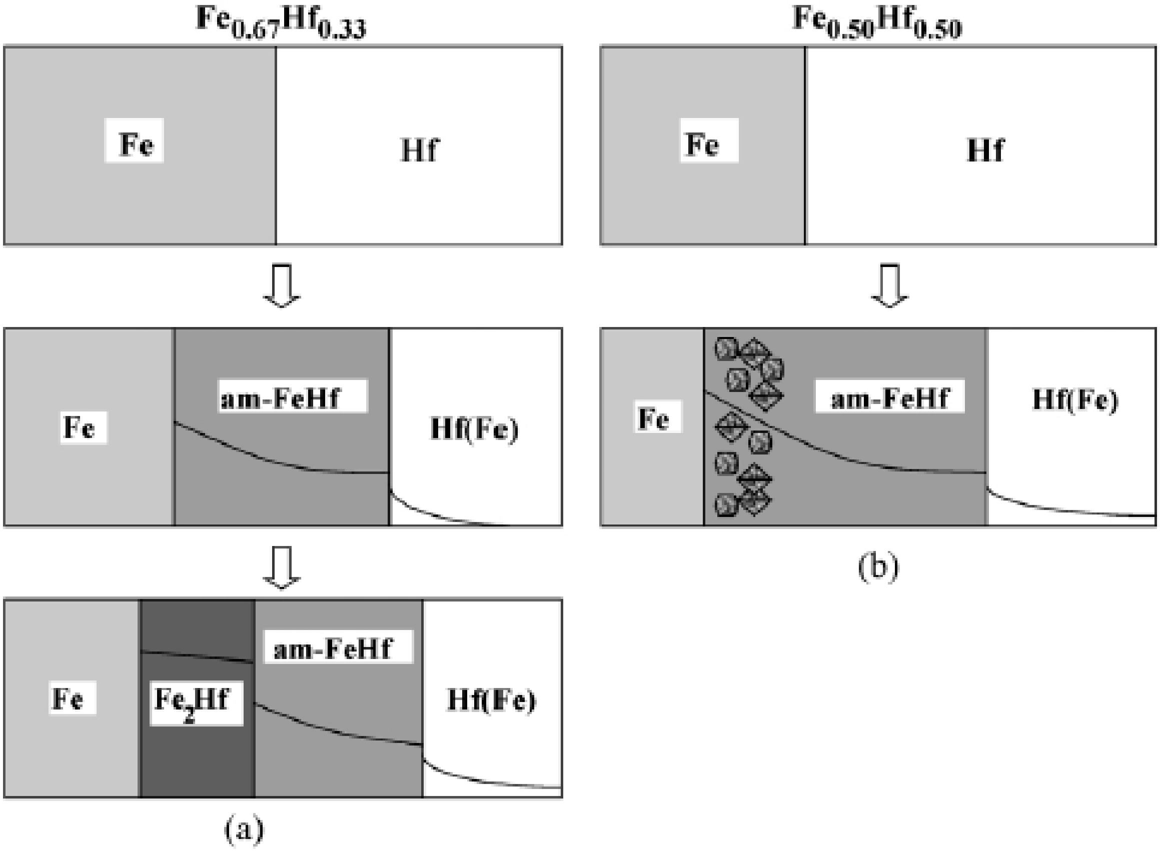

Figure 1-6 Schematic representation of the solid-state reaction at the interface of (a) $Fe_{0.67}Hf_{0.33}$ and (b) $Fe_{0.50}Hf_{0.50}$ films, showing the hypothetical iron profiles, considering a planar growth for every reacted layer [14].

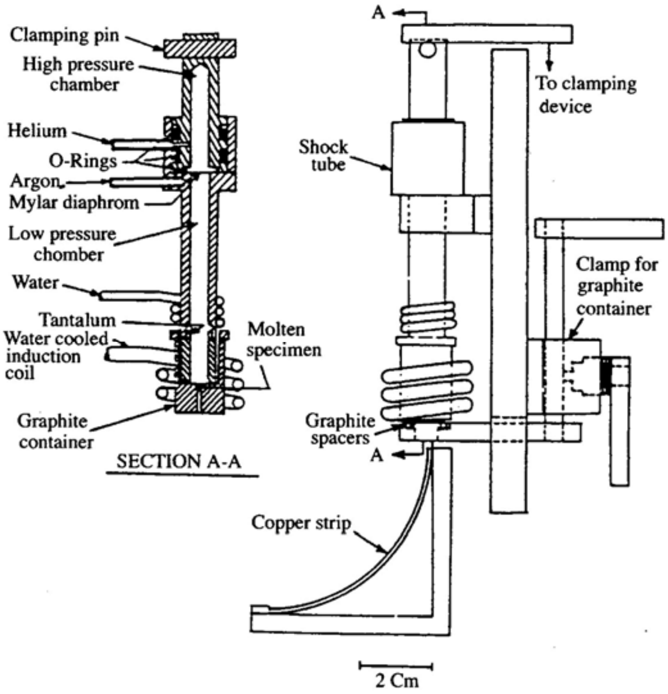

Figure 2-1 A schematic diagram of the splat quenching methods[43].

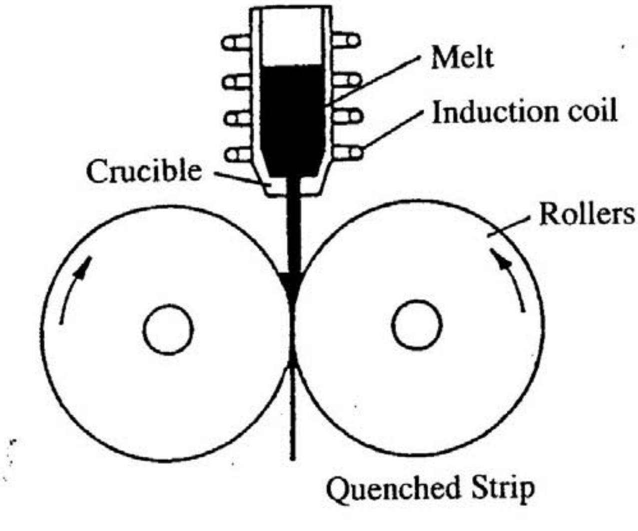

Figure 2-2 A schematic diagram of the two roller quenching method[43].

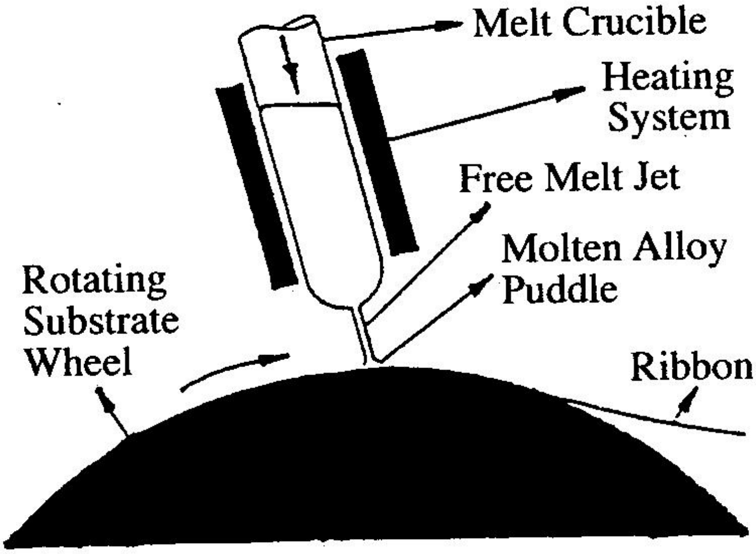

Figure 2-3 A schematic diagram of the chill block melt spinning [43].

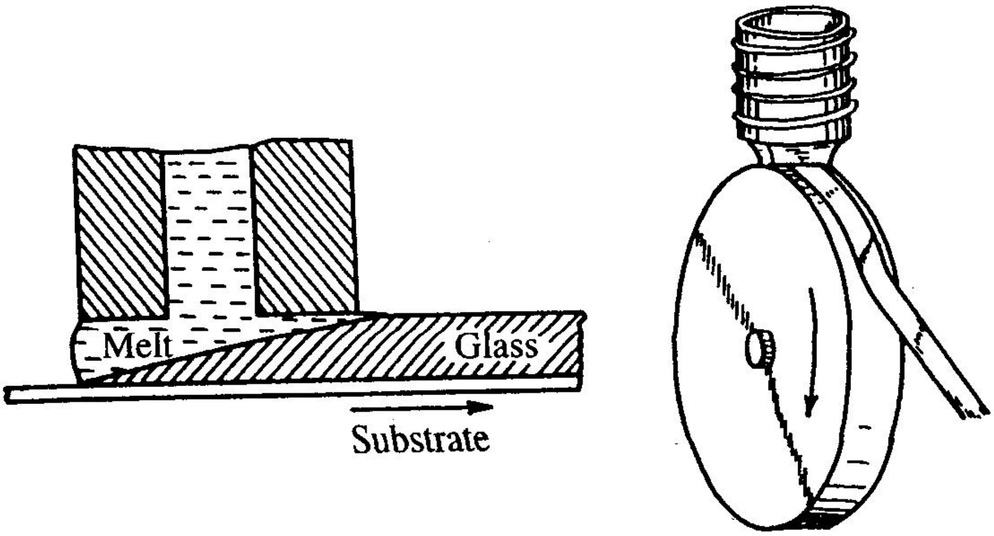

Figure 2-4 A schematic diagram of the planar flow casting process [43].

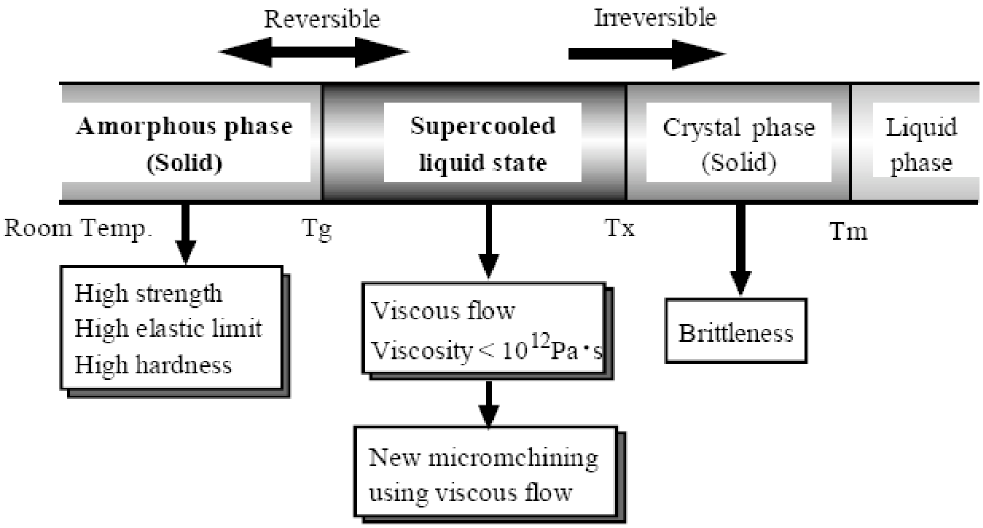

Figure 2-5 Characteristics of metallic glasses [11].

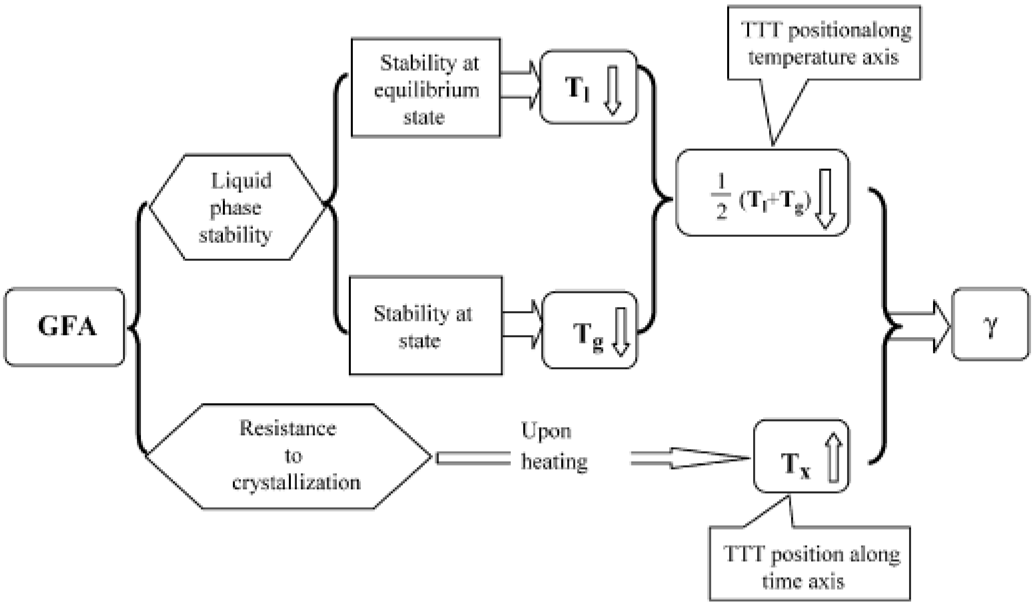

Figure 2-6 New approach for understanding GFA of amorphous materials [49].

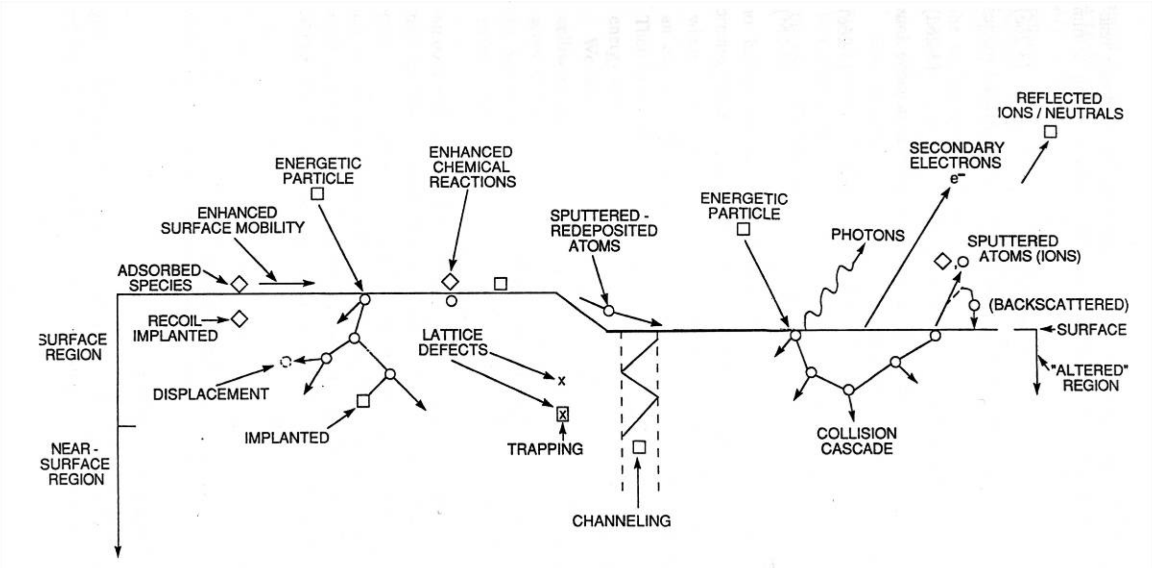

Figure 2-7 Events that occur on a surface being bombarded with energetic atomic-sized particles [51].

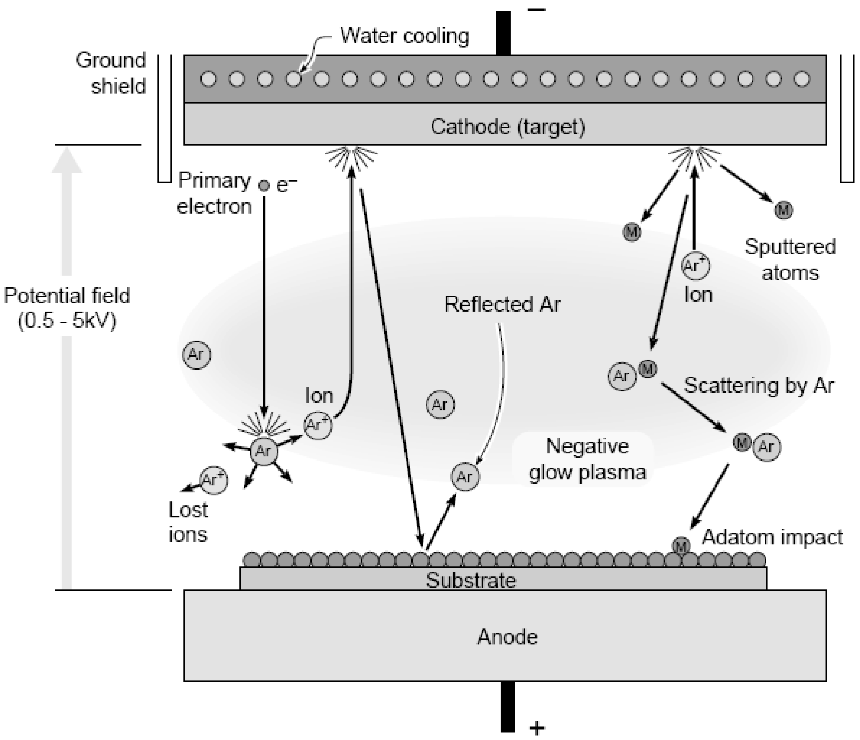

Figure 2-8 A schematic illustration of a DC diode Sputtering System [53].

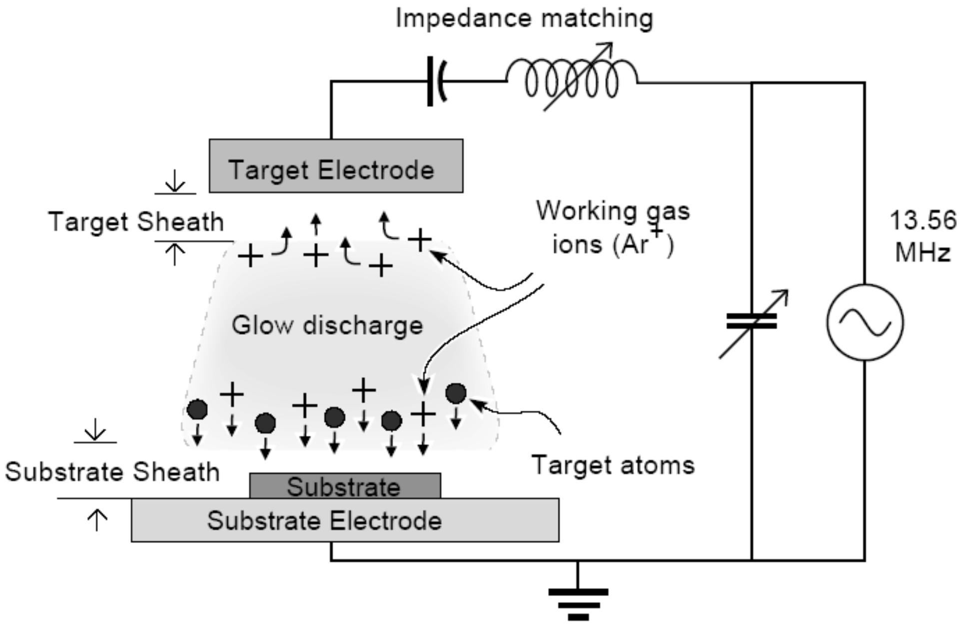

Figure 2-9 A schematic illustration of the RF diode sputtering deposition [53].

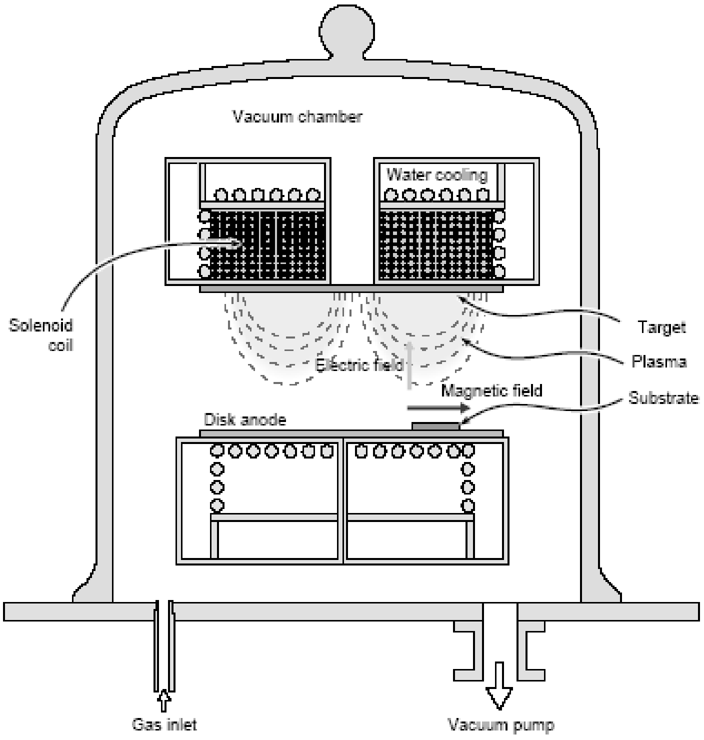

Figure 2-10 A schematic illusion of a planar magnetron sputtering system [53].

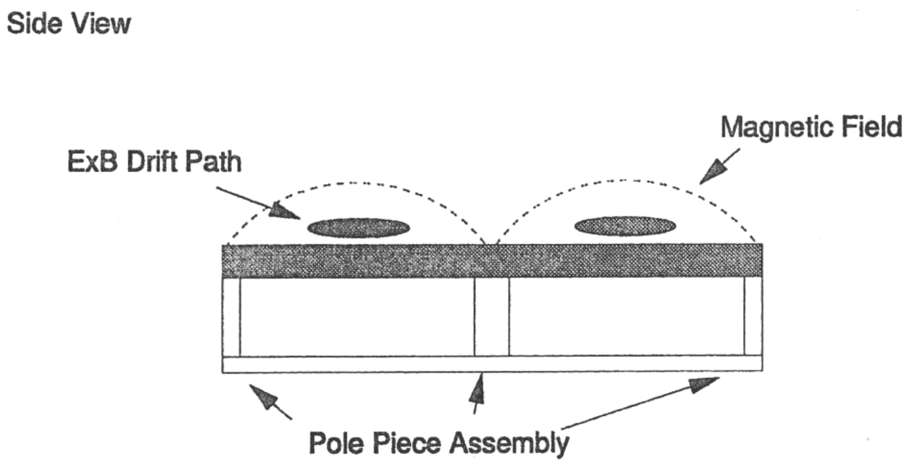

Figure 2-11 The side view of the magnetic field configuration for circular planar magnetron cathode [50].

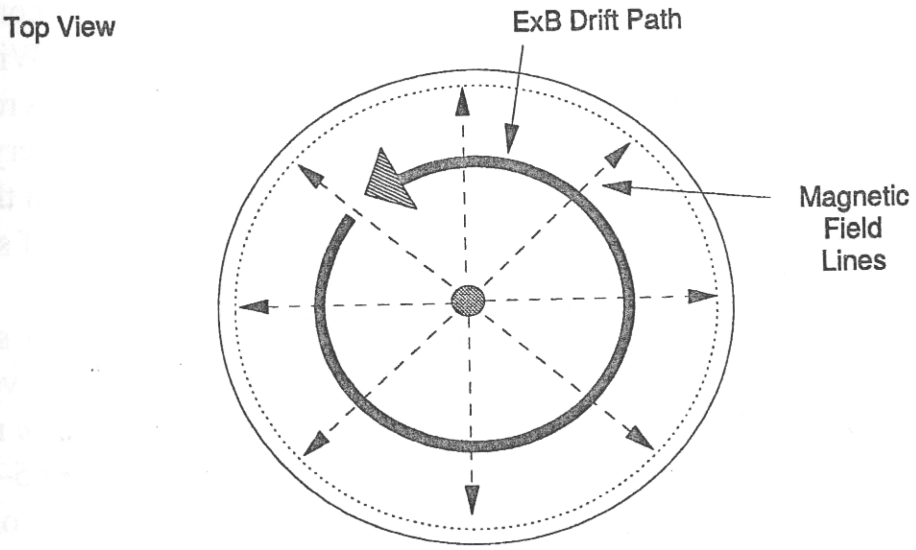

Figure 2-12 The top view of the magnetic field configuration for a circular planar magnetron cathode [50].

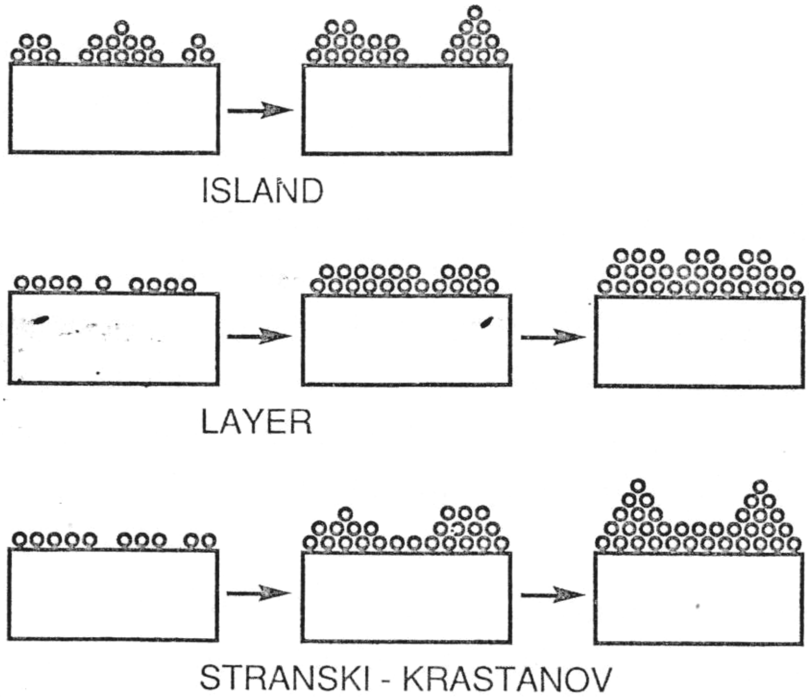

Figure 2-13 Basic modes of thin-film growth [54].

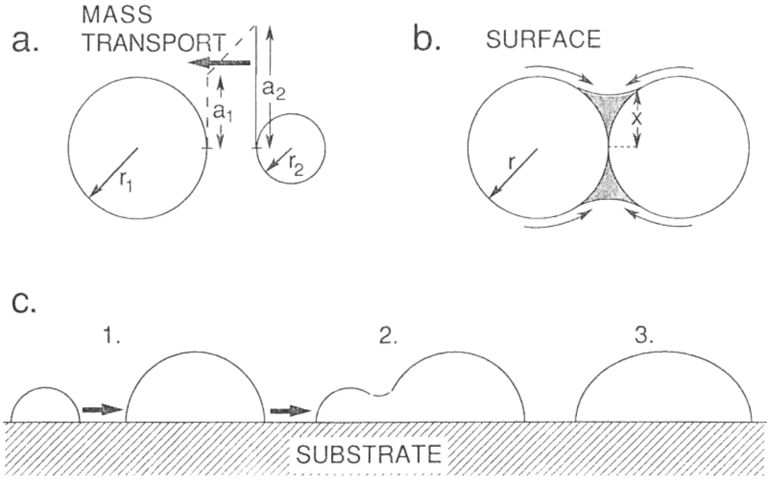

Figure 2-14 Coarsing of islands due to (a) Ostwald ripening, (b) sintering, and (c) cluster migration [54].

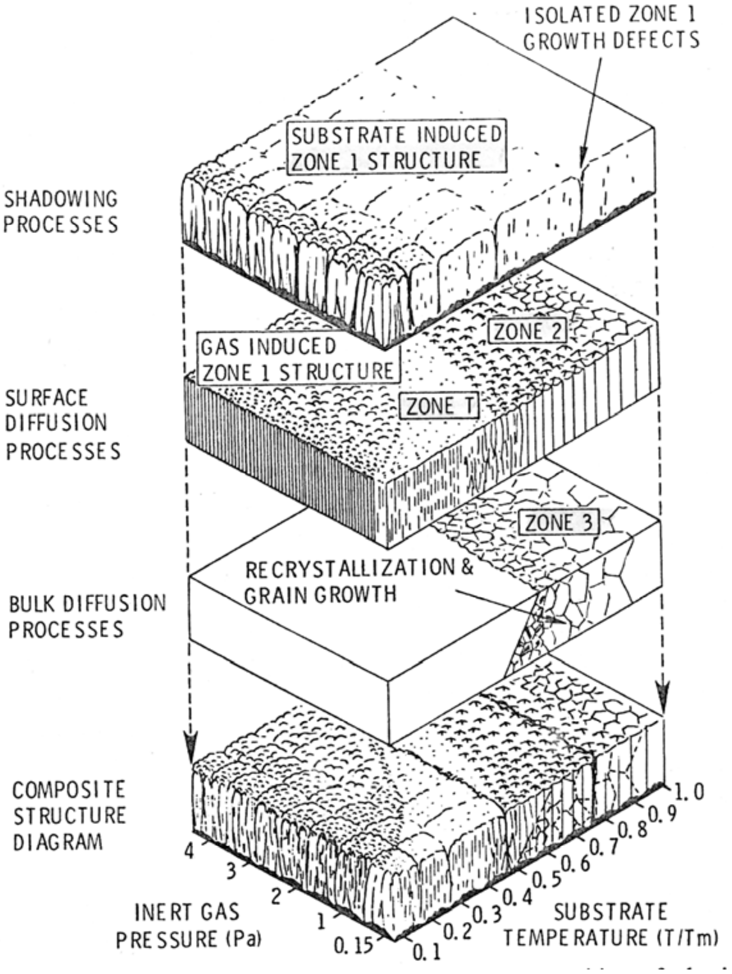

Figure 2-15 A schematic representation showing the superposition of physical process which establishes structural zones [51].

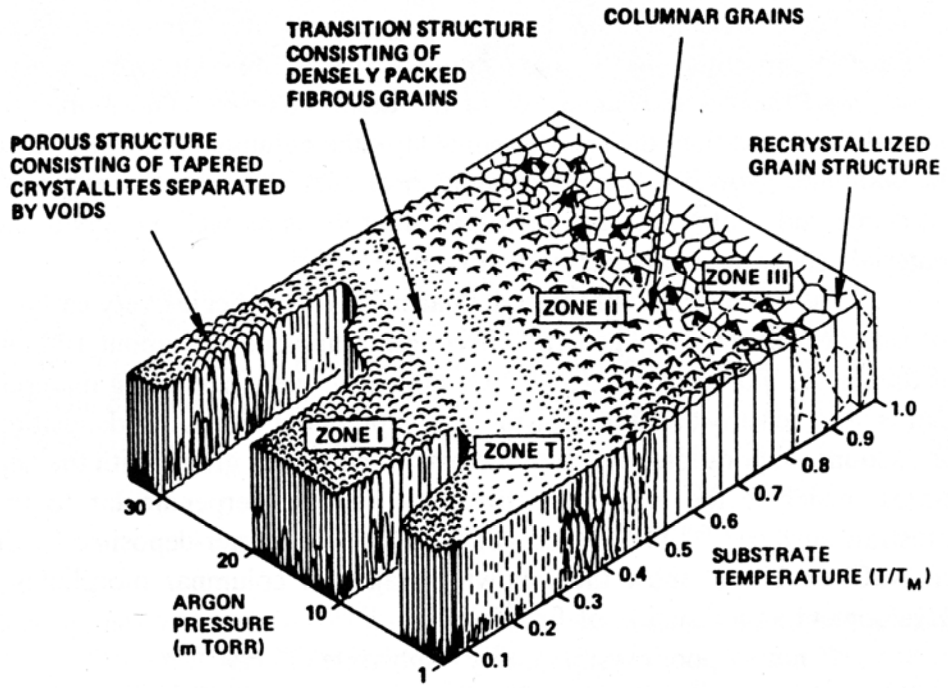

Figure 2-16 Structure zone model of sputtering deposited materials [51].

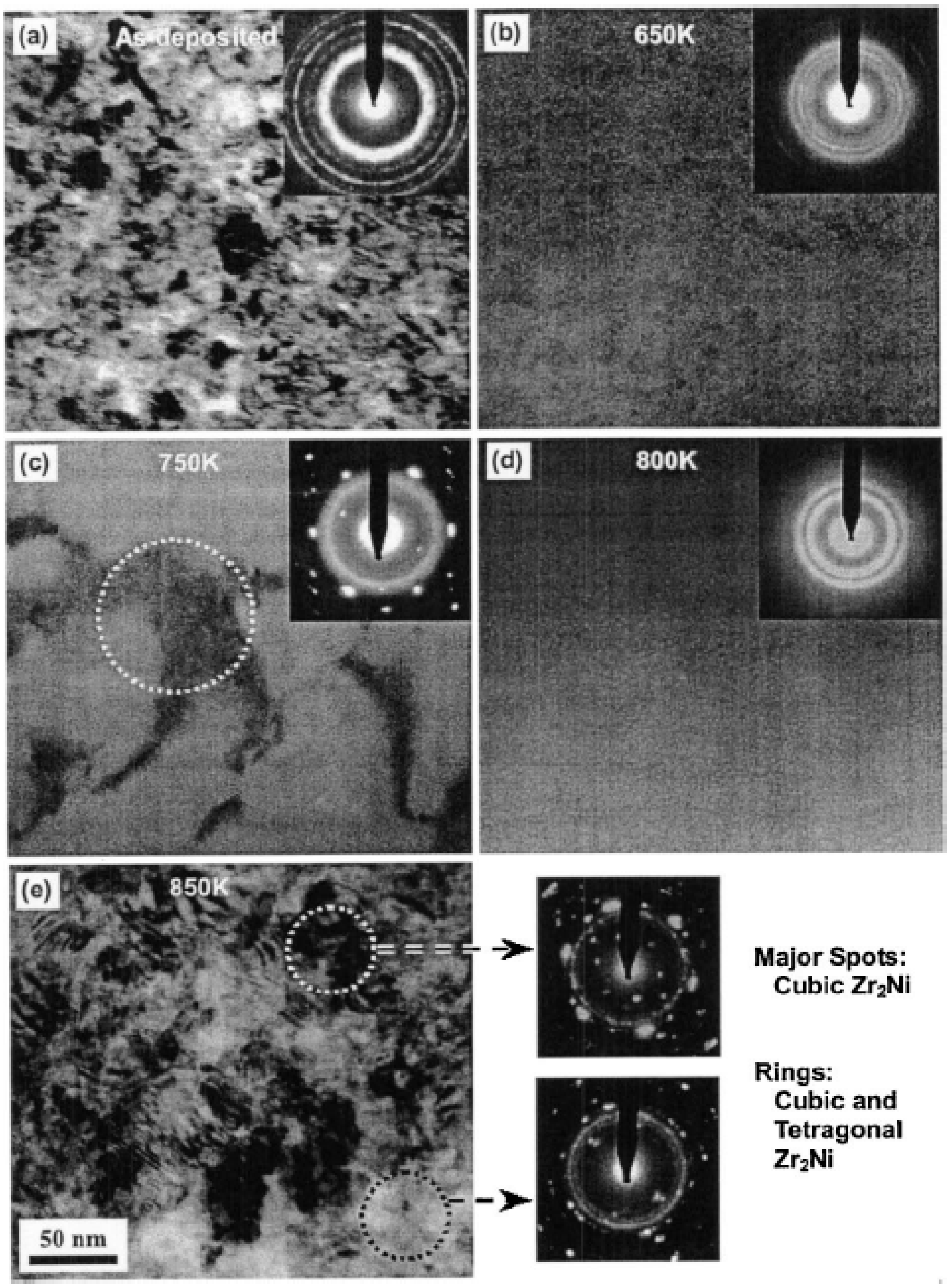

Figure 2-17 Plane-view TEM micrographs and diffraction pattern of the films in (a) as-deposited and annealed conditions at (b) 650, (c) 750, (d) 800, and (e) 850 K. The circled regions indicate the location for obtaining the diffraction patterns [12].

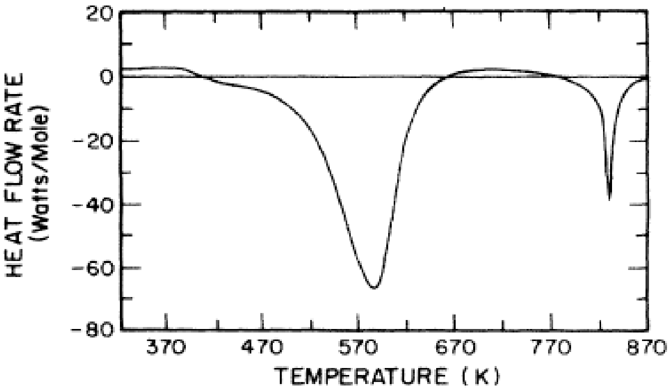

Figure 2-18 The heat-flow rate as a function of temperature for a sputtered, multilayered thin film of the average stoichiometry $Ni_{68}Zr_{32}$ [27].

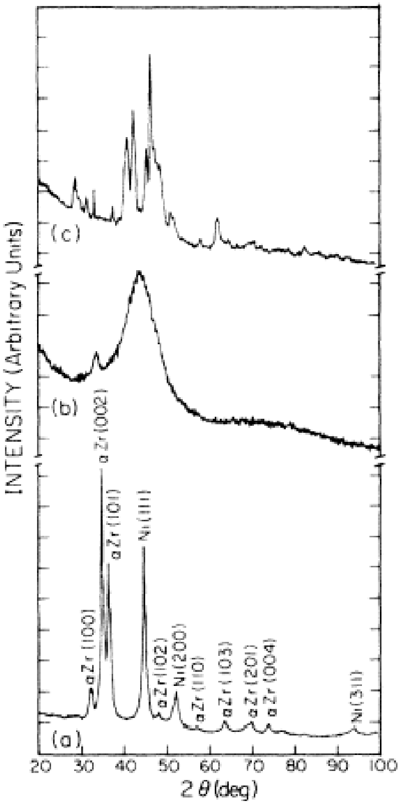

Figure 2-19 X-ray diffraction profile for the Ni-Zr thin film: (a) as deposited, (b) after DSC scan to 670 K and quench to room temperature, (c) after a DSC scan to 870 K [27].

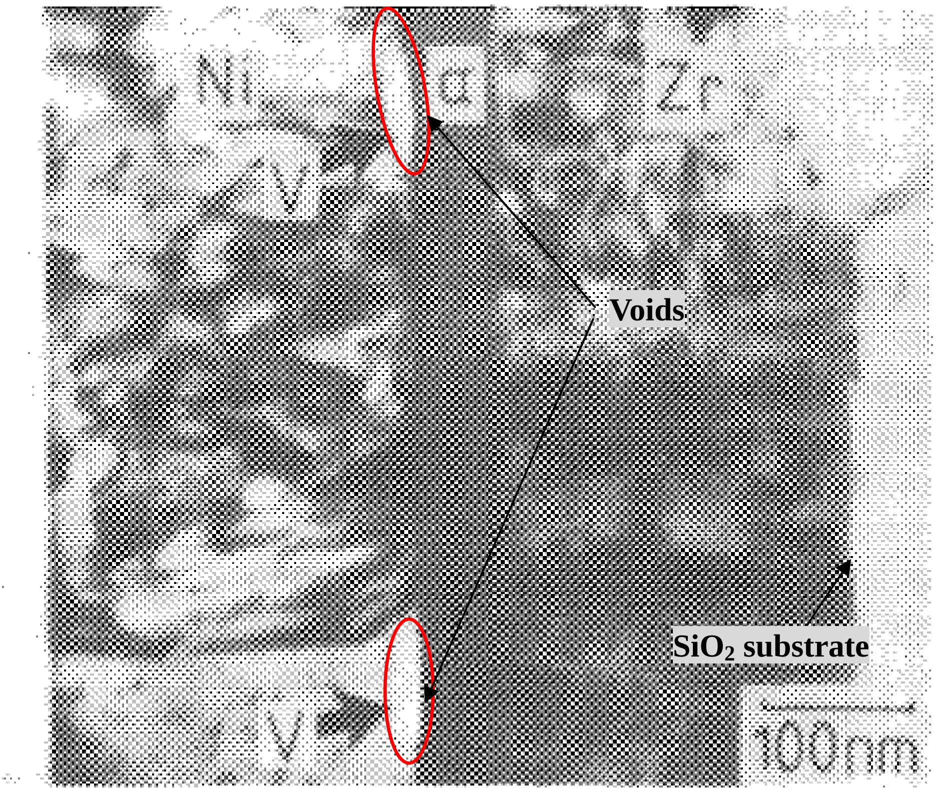

Figure 2-20 Cross-section bright-field TEM micrograph of a Ni/Zr bilayer annealed at 300°C for 60 min. Void may be seen at the Ni/NiZr interface as at V [39].

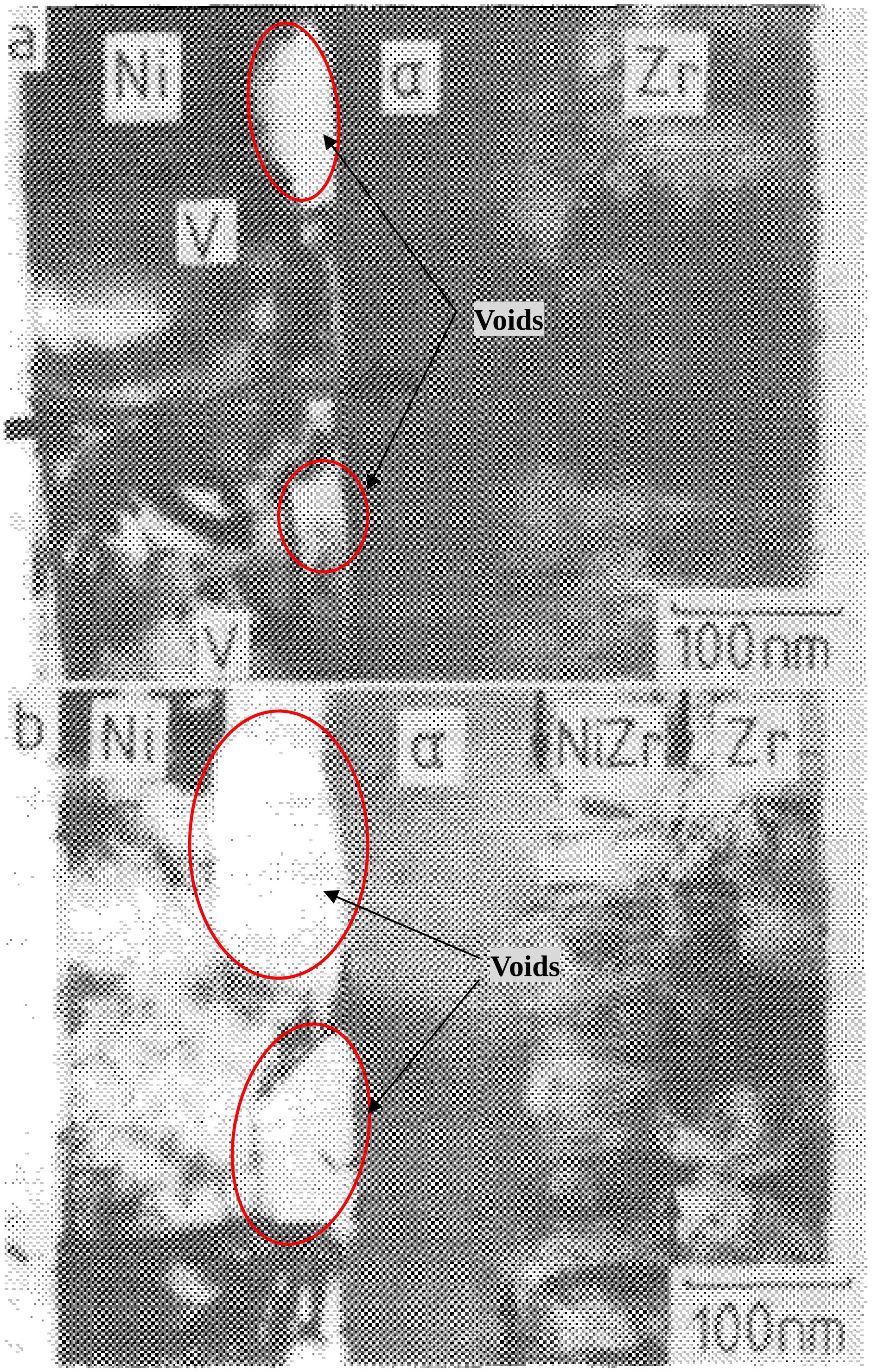

Figure 2-21 Cross-section bright-field TEM micrographs of Ni/Zr bilayer annealed at 300^{o}C for (a) 240 min and (b) 720 min. The growth of the voids can be noted [39].

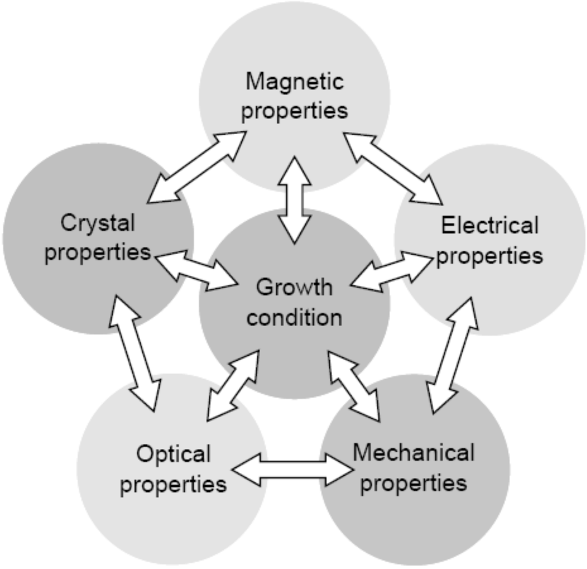

Figure 2-22 Correlations exist between vapor phase growth conditions and many of properties of the resultant thin film [53].

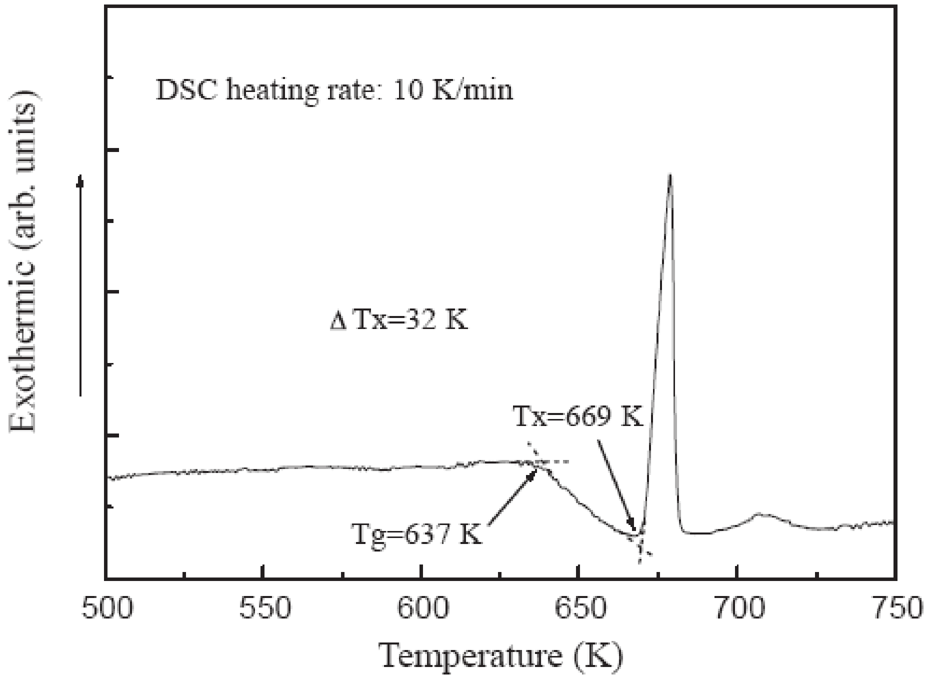

Figure 2-23 The DSC curve of Pd-TFMG [13].

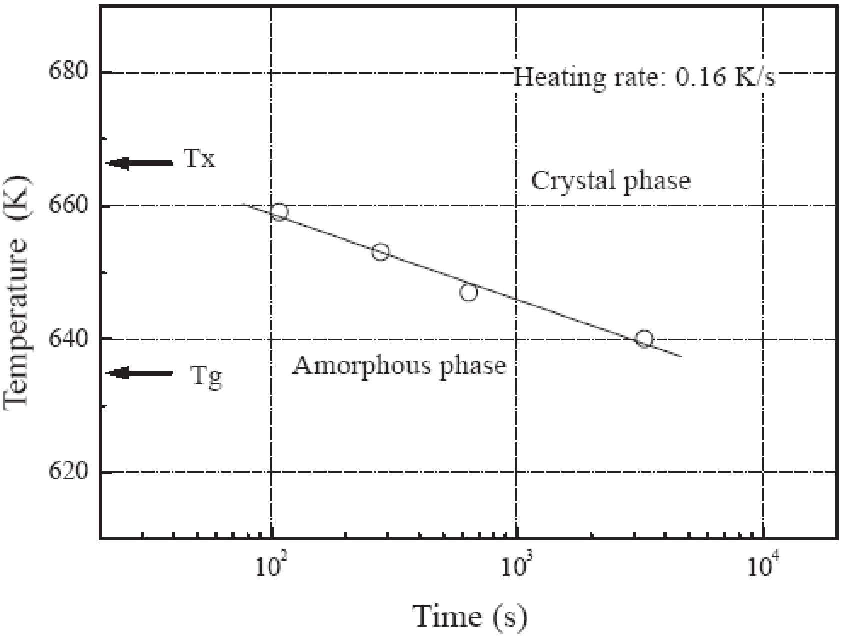

Figure 2-24 TTT diagram for the onset of crystallization of Pd-TFMG [13].

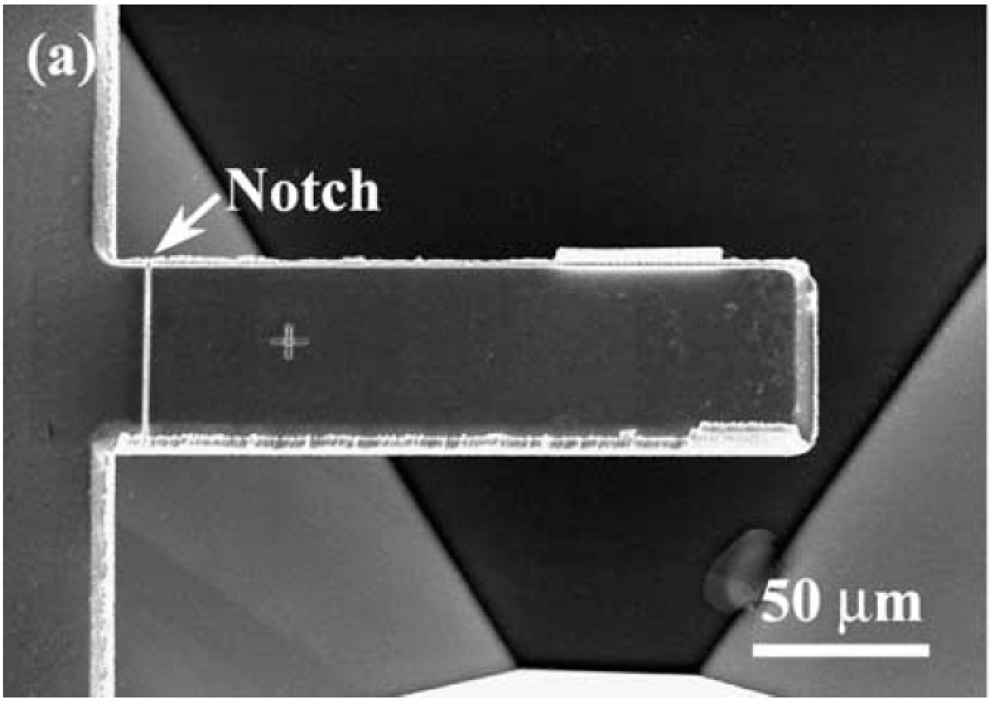

Figure 2-25 SEM image of a Pd-thin-film metallic glass free-standing microbeam with a notch fabricated by FIB [33].

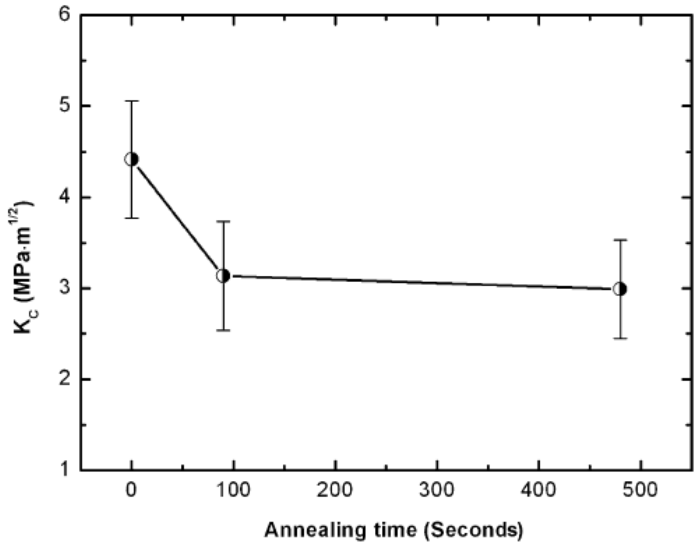

Figure 2-26 Variation of notch fracture toughness (K_C) of Pd-based thin-film metallic glass as a function of annealing time in the supercooled liquid region at 640 K close to T_g = 637 K [33].

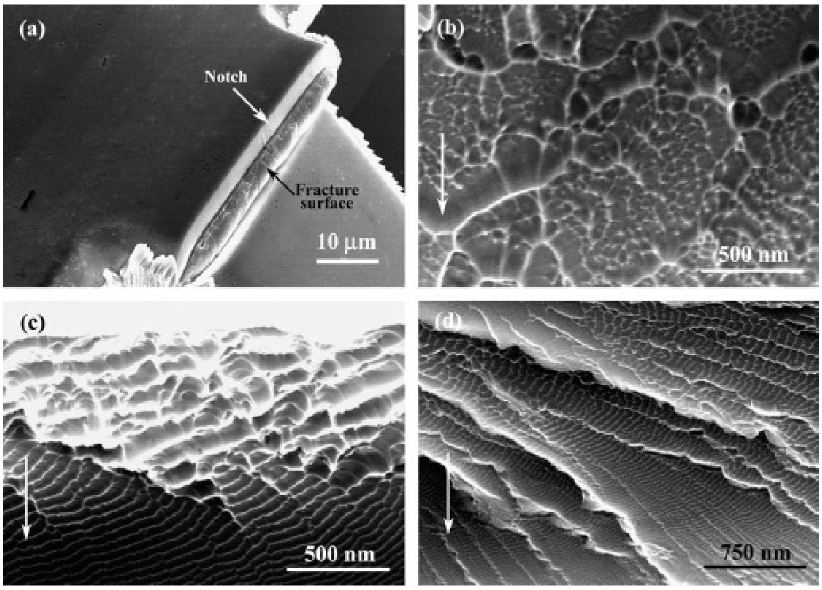

Figure 2-27 SEM micrographs of the fracture behaviors ahead of the notch tips in Pd-based TFMG (a) as-deposited, an overview of the fractured sample, (b) as-deposited, a high magnification observation of the fracture surface, (c) annealed for 90 s and (d) annealed for 480 s [33].

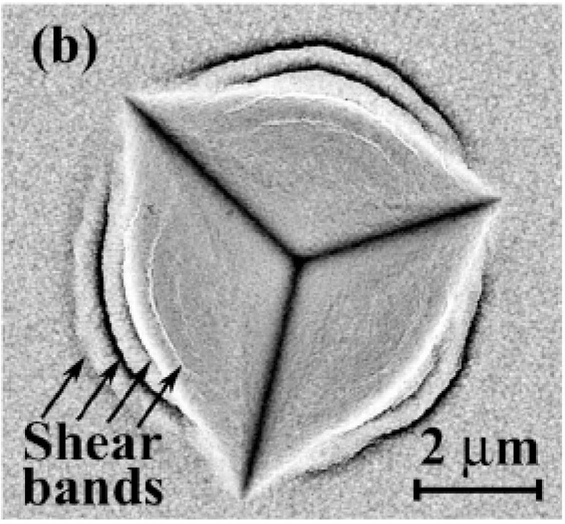

Figure 2-28 The SEM image of the deformation morphologies around the indents in the Au/Cu multilayers with individual layer thicknesses [32].

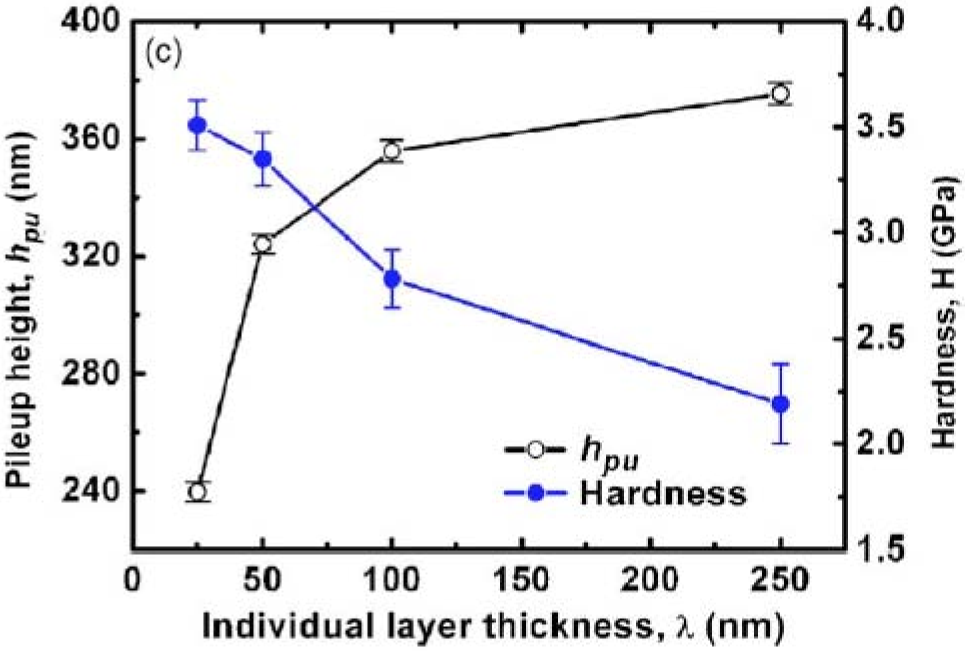

Figure 2-29 The pileup height (h_{pu}) and the hardness (H) as a function of λ. Hardness (H) was measured at the 200 nm indentation depth [32].

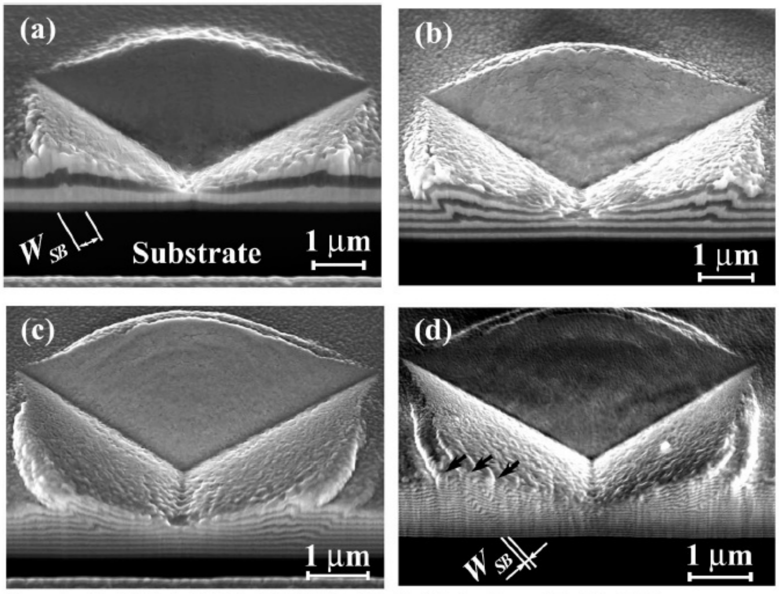

Figure 2-30 FIB cross-sectional views of the indents in the Au/Cu multilayers with individual layer thicknesses (λ) of (a) λ = 250 nm, (b) λ = 100 nm, (c) λ = 50 nm, (d) λ = 25 nm. The bright and dark layers correspond to Au and Cu layers, respecrively. Inhomogeneous shear banding becomes prevalent with the decrease in λ [32].

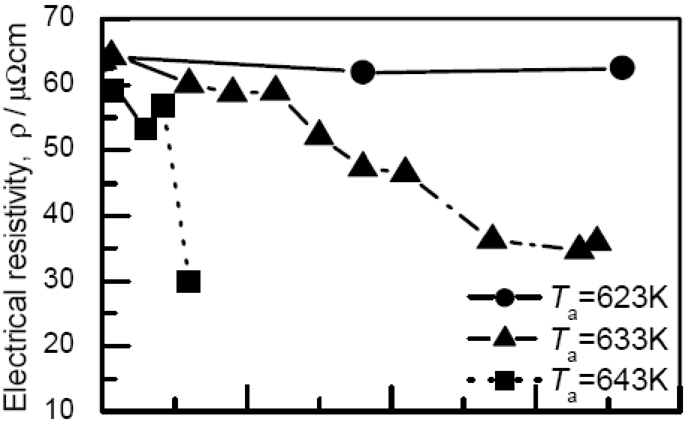

Figure 2-31 Electrical resistivity ρ as a function of annealing time T_a in the $Pd_{76}Cu_6Si_{18}$ thin film metallic glasses annealed at various temperatures [31].

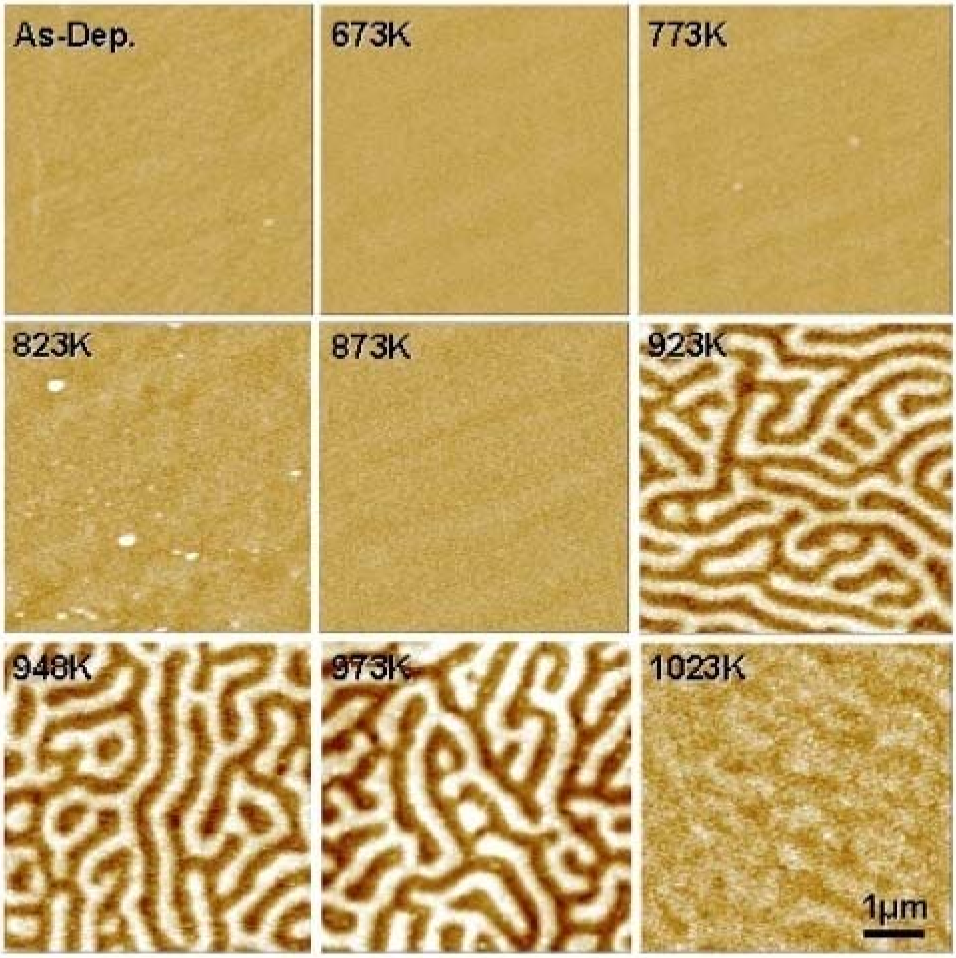

Figure 2-32 Magnetic force microscopy images of films in the as-deposited and annealed conditions [61].

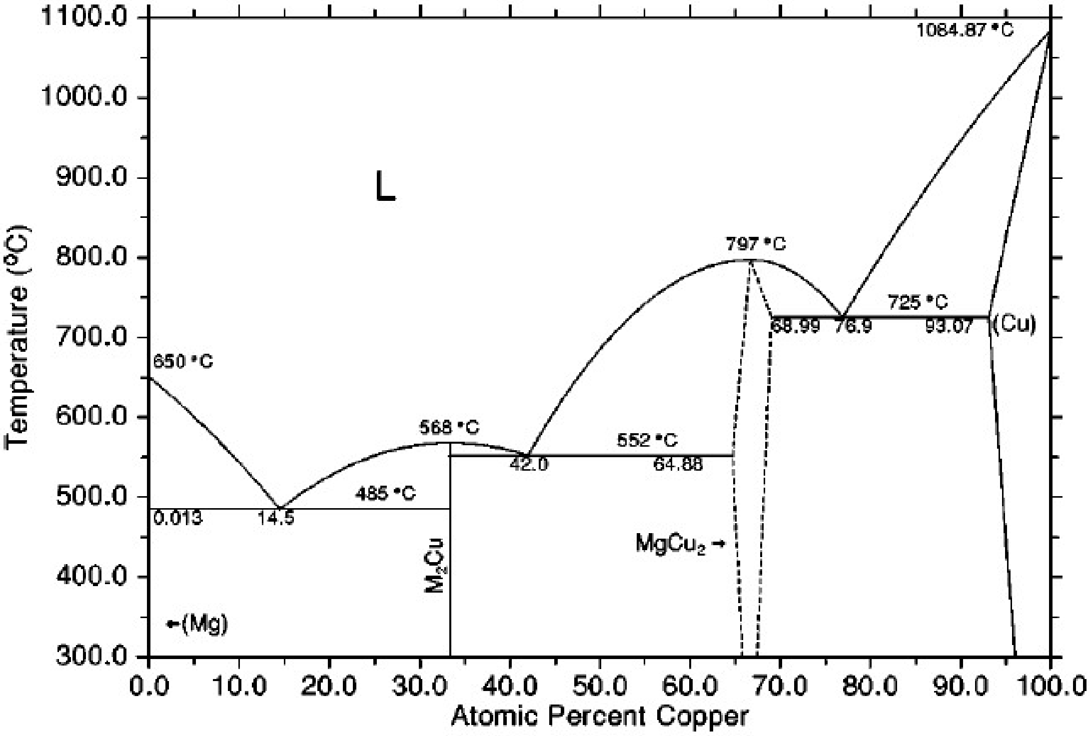

Figure 3-1 Mg-Cu binary phase diagram.

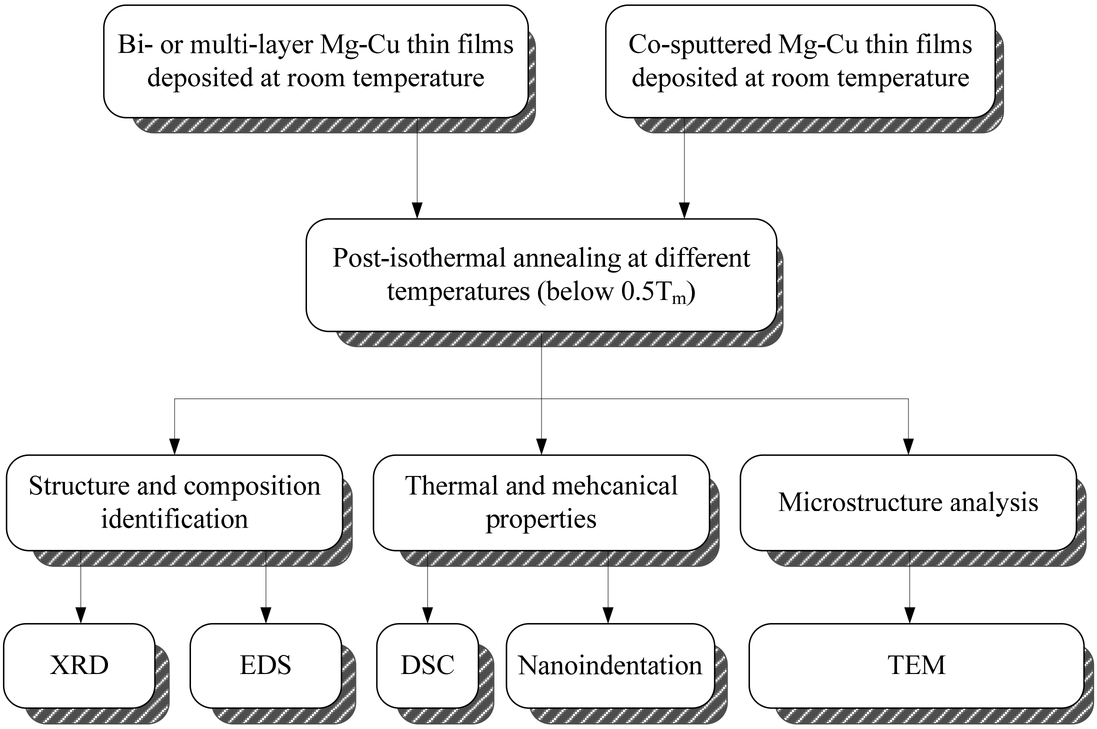

Figure 3-2 Flow chart of the experimental procedures.

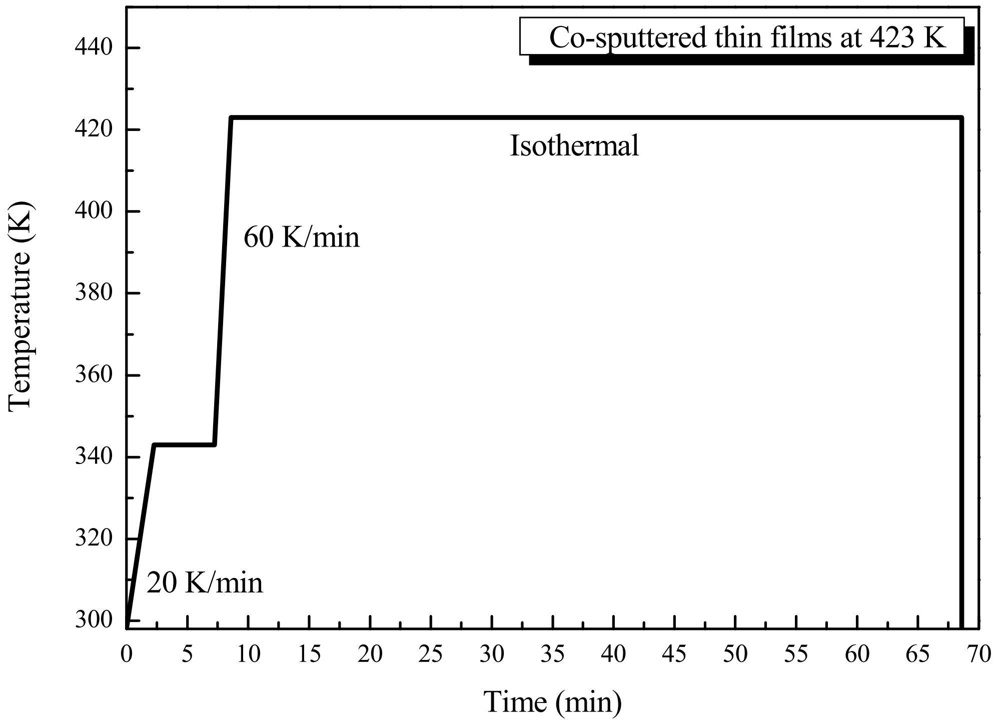

Figure 3-3 Temperature profile of the isothermal heat-treatment at 423 K of the co-sputtered thin films.

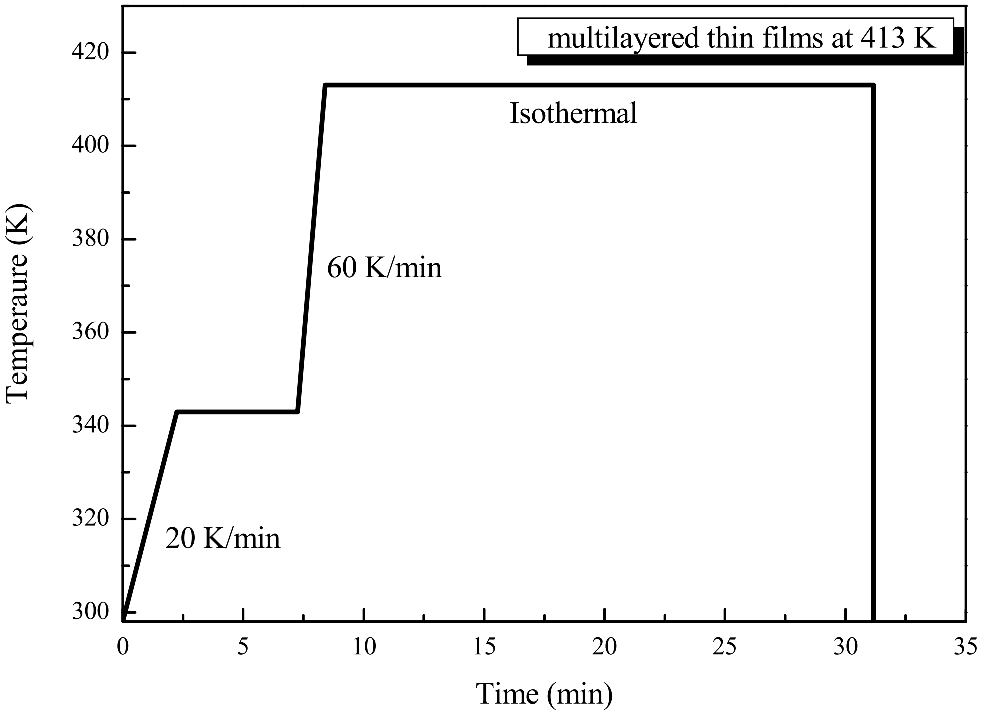

Figure 3-4 Temperature profile of the isothermal heat-treatment at 413 K of the multilayered 20T32 and 40N32 films.

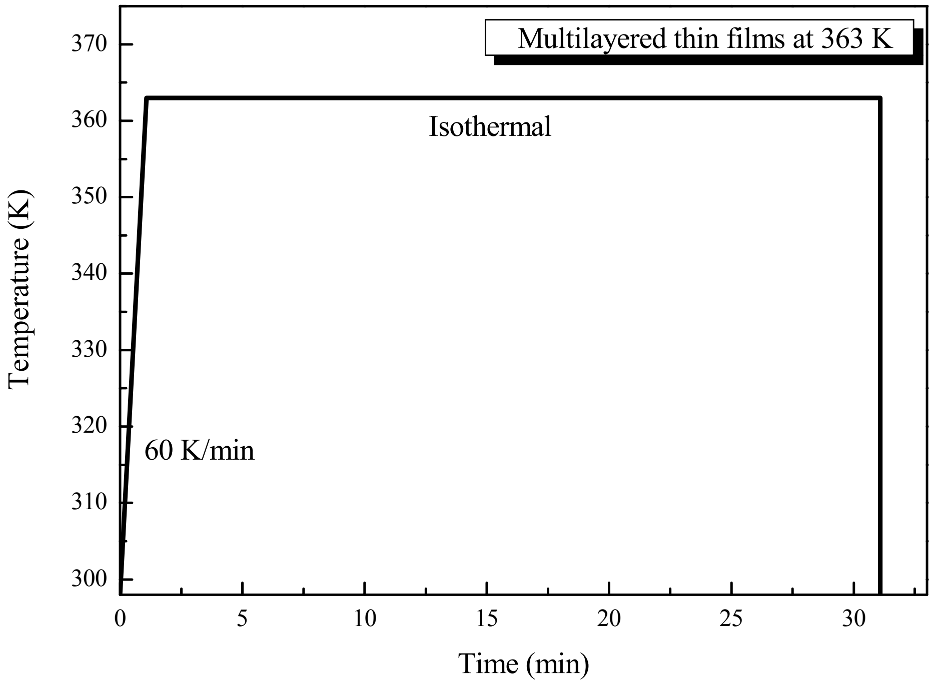

Figure 3-5 Temperature profile of the isothermal heat-treatment at 363 K of the multilayered 20T14 and 40N14.

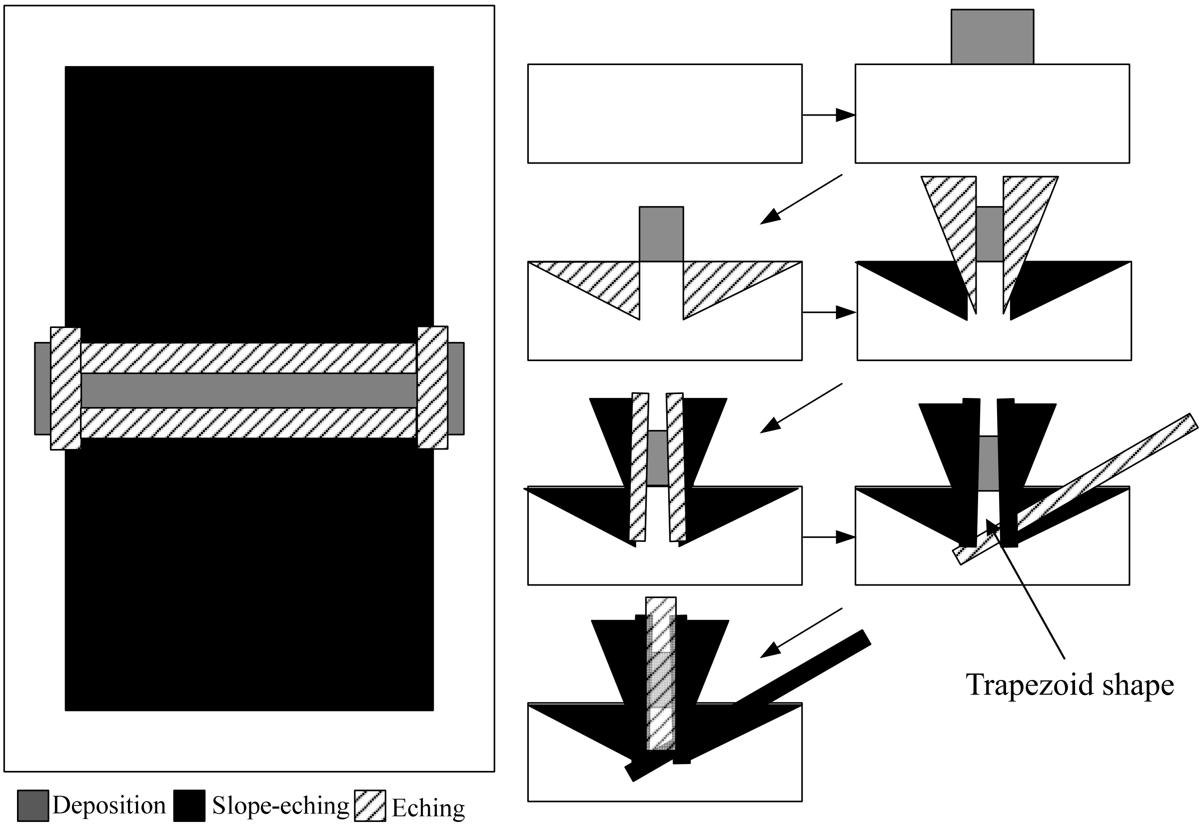

(a) (b)

Figure 3-6 Schematic illustrations of (a) Top-view and (b) Side-view of preparation of XTEM-specimen by focus ion beam (FIB).

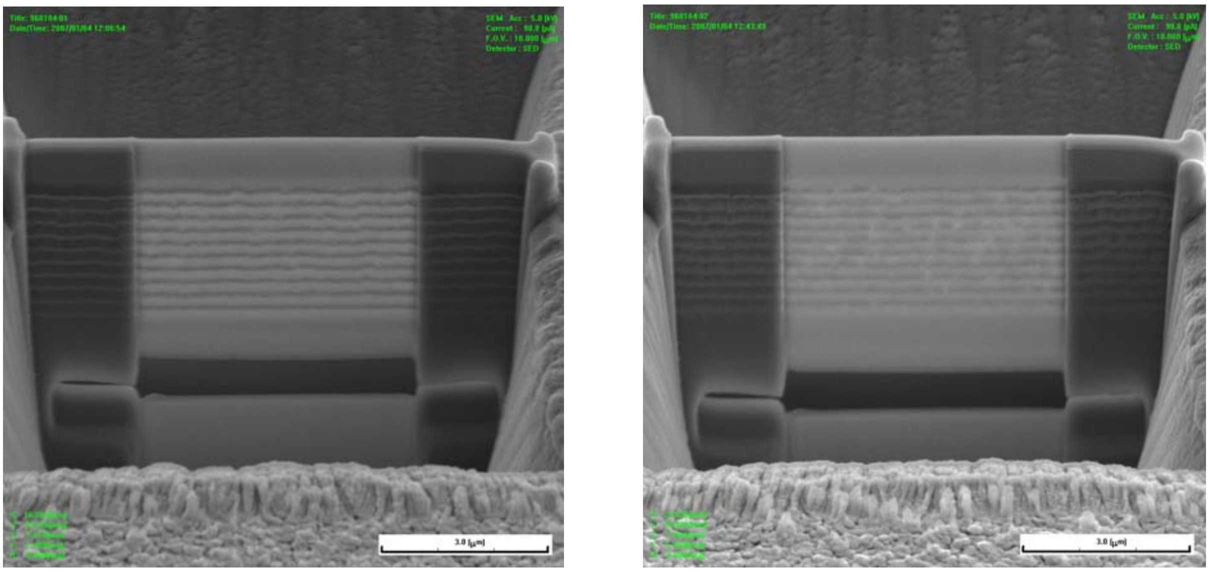

(a) (b)

Figure 3-7 Cross-section images of 20T32 and annealed 20T32 specimens during XTEM preparation via FIB technique.

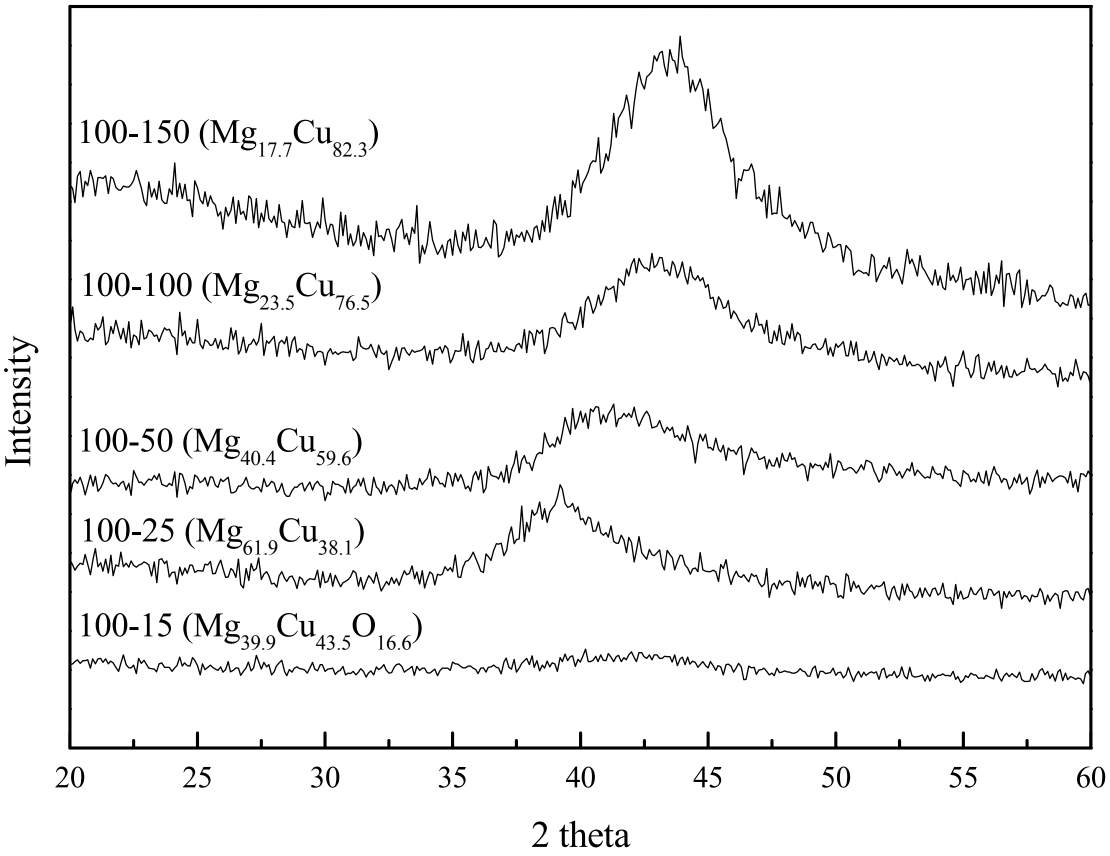

Figure 4-1 XRD patterns of the 100 series.

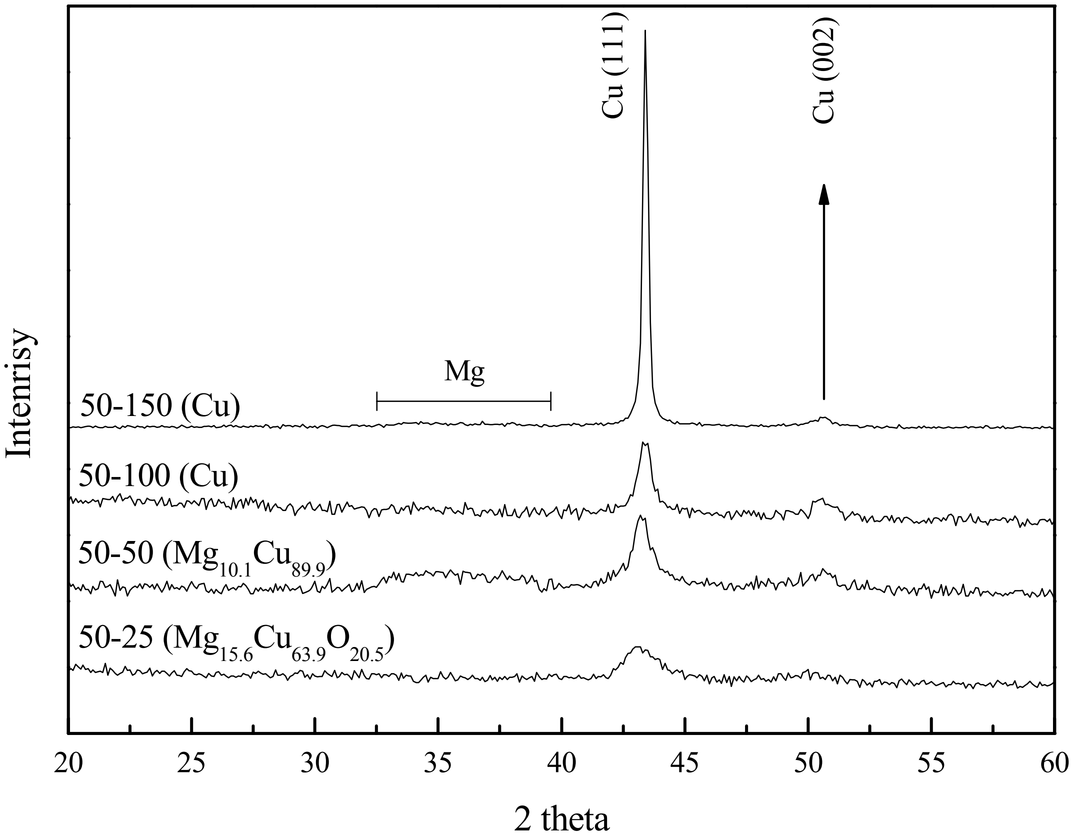

Figure 4-2 XRD patterns of the 50 series.

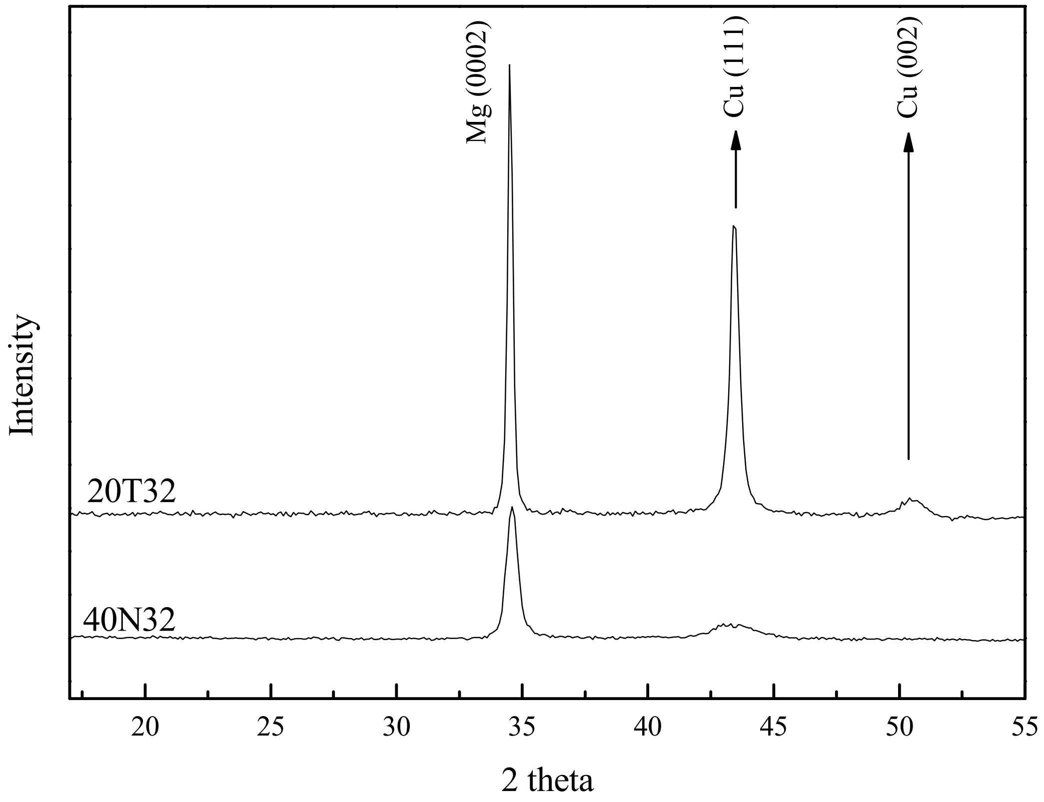

Figure 4-3 XRD patterns of the as-deposited 20T32 and 40N32.

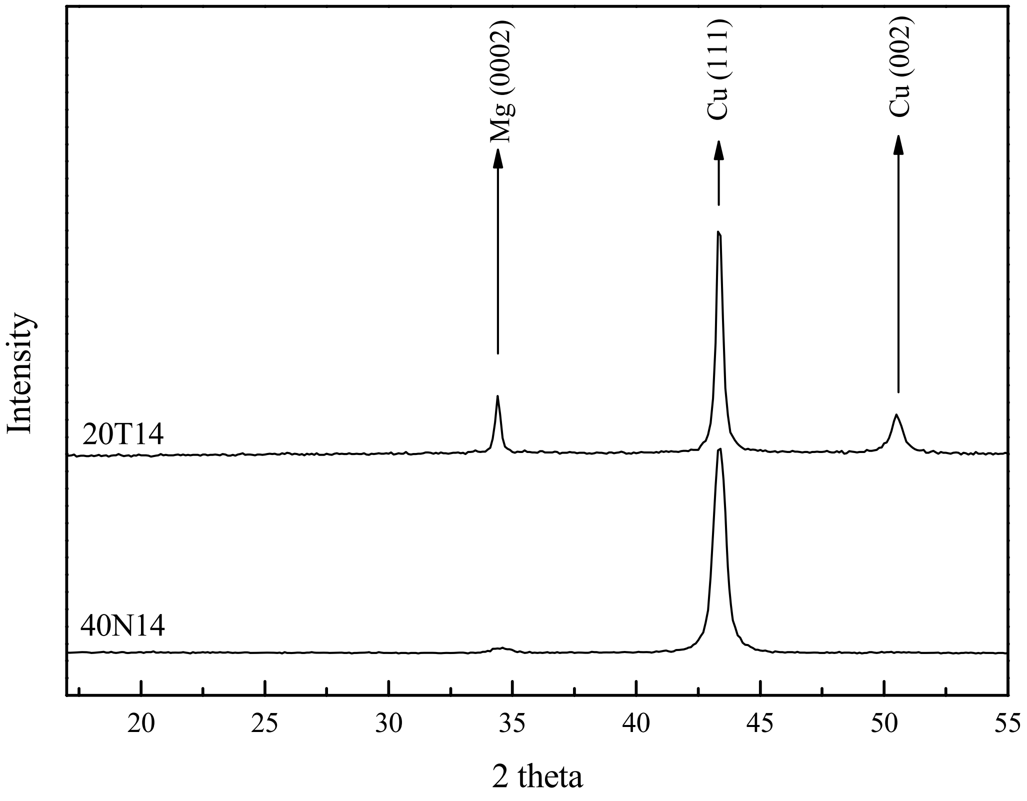

Figure 4-4 XRD patterns of the as-deposited 20T14 and 40N14.

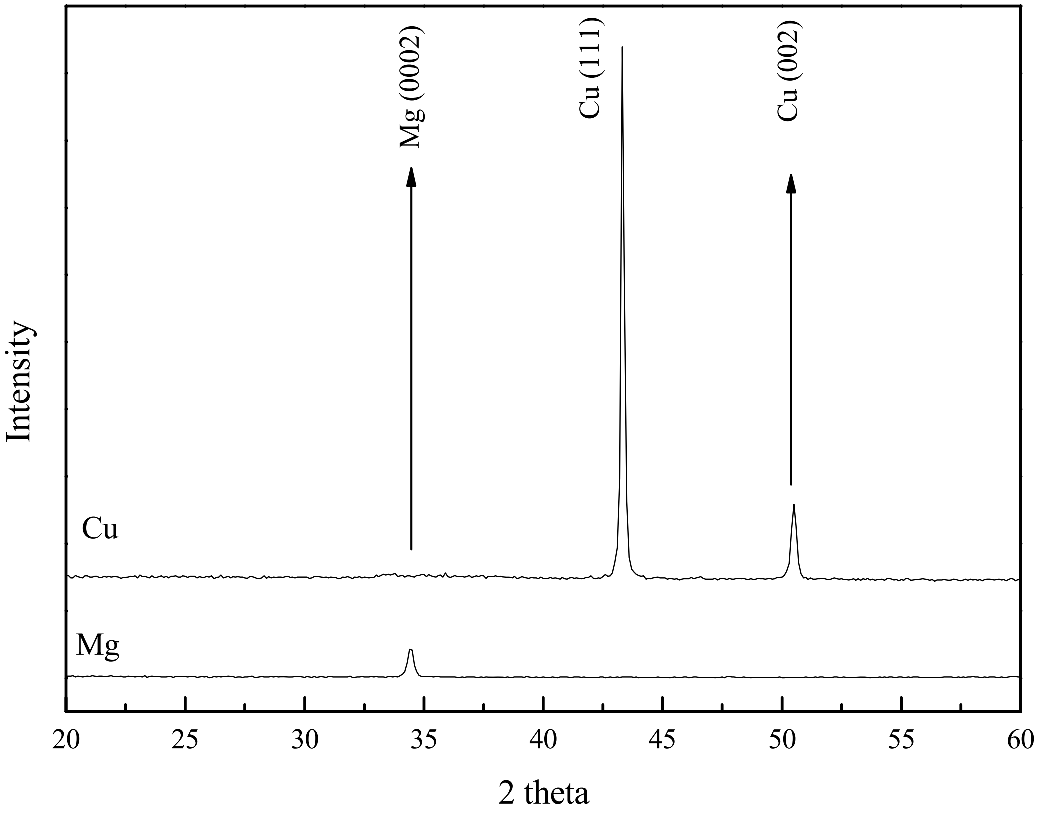

Figure 4-5 XRD patterns of the pure Mg and Cu metallic films.

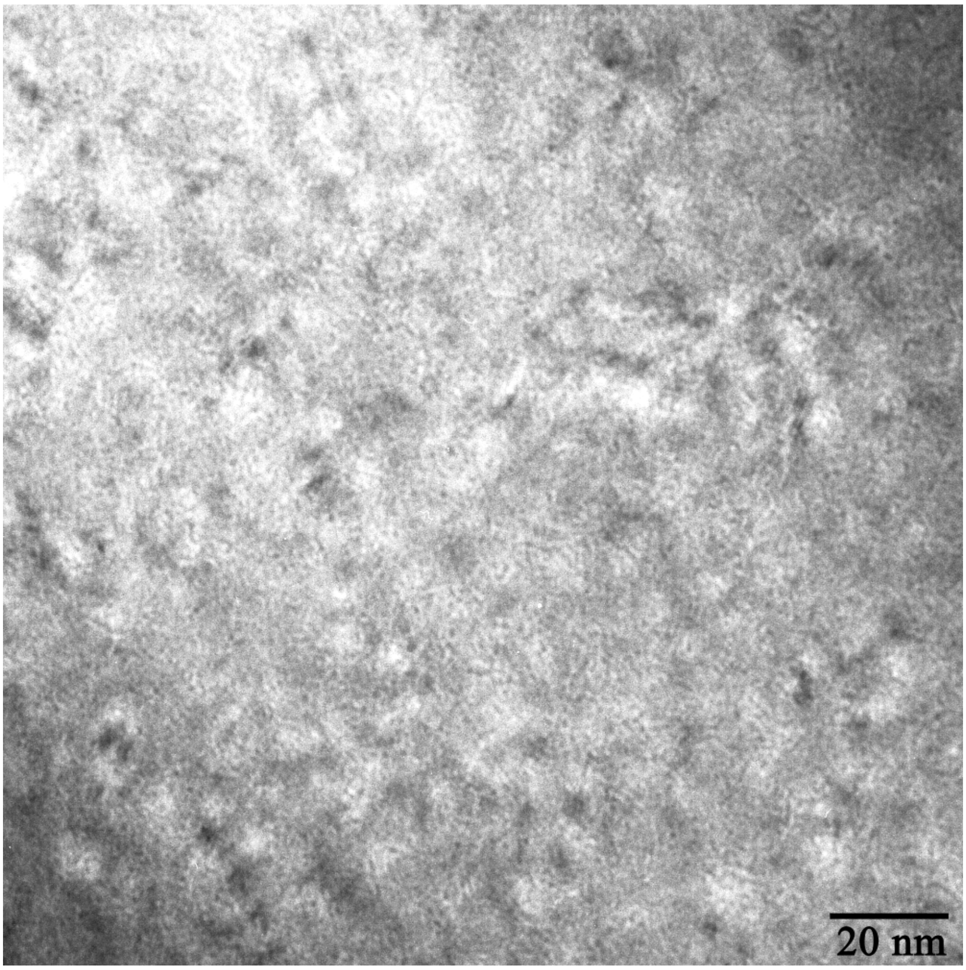

Figure 4-6 TEM plane-view bright-field image of 100-150.

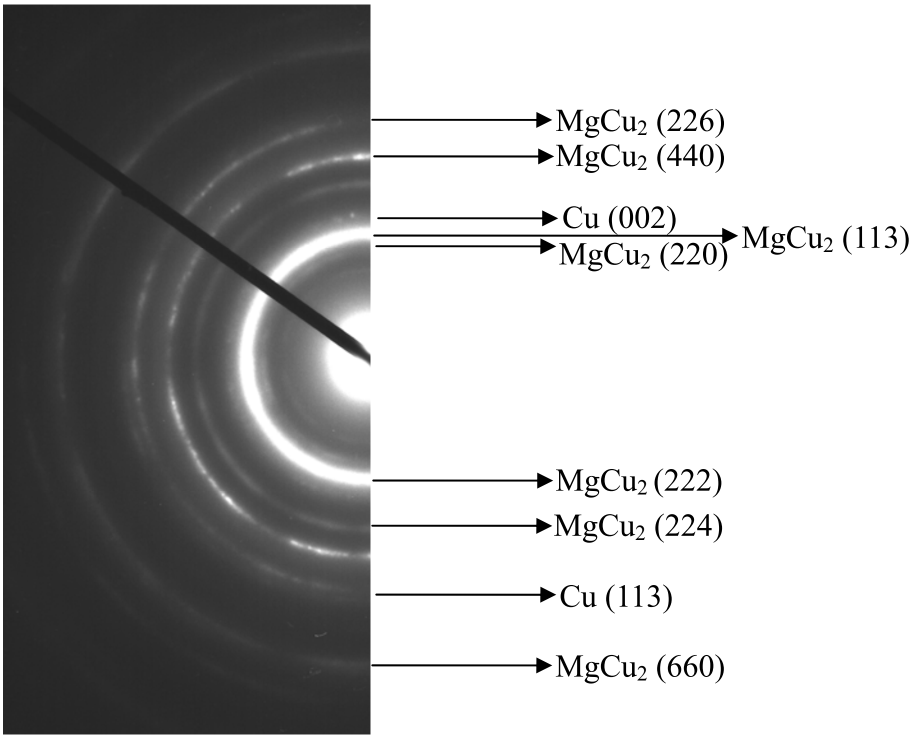

Figure 4-7 Selected area diffraction pattern of 100-150.

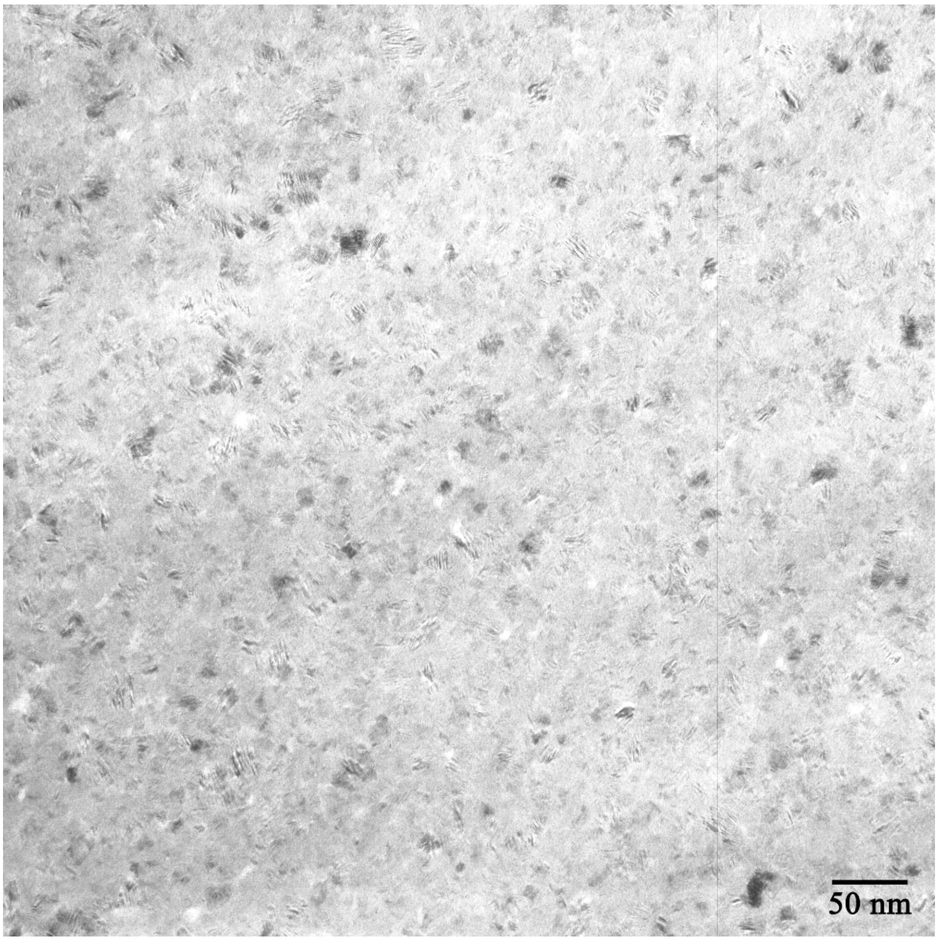

Figure 4-8 TEM plane-view low-magnitude bright-field image of 100-100.

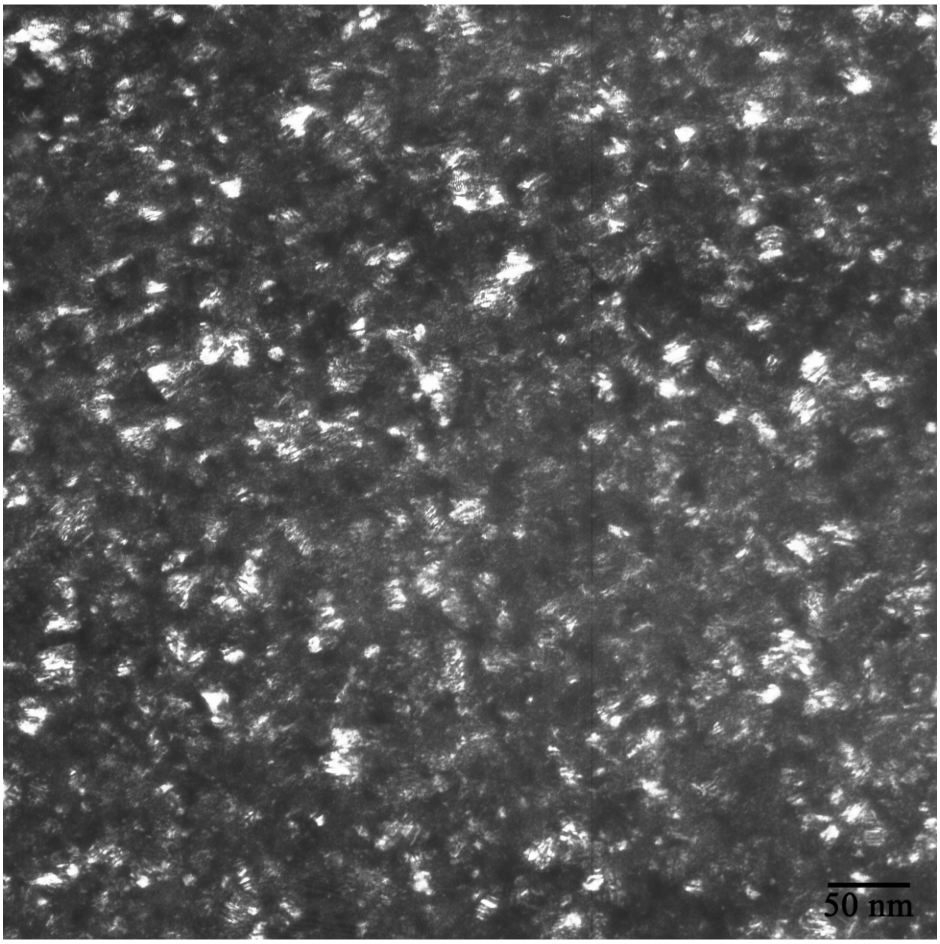

Figure 4-9 TEM plane-view low-magnitude dark-field image of 100-100.

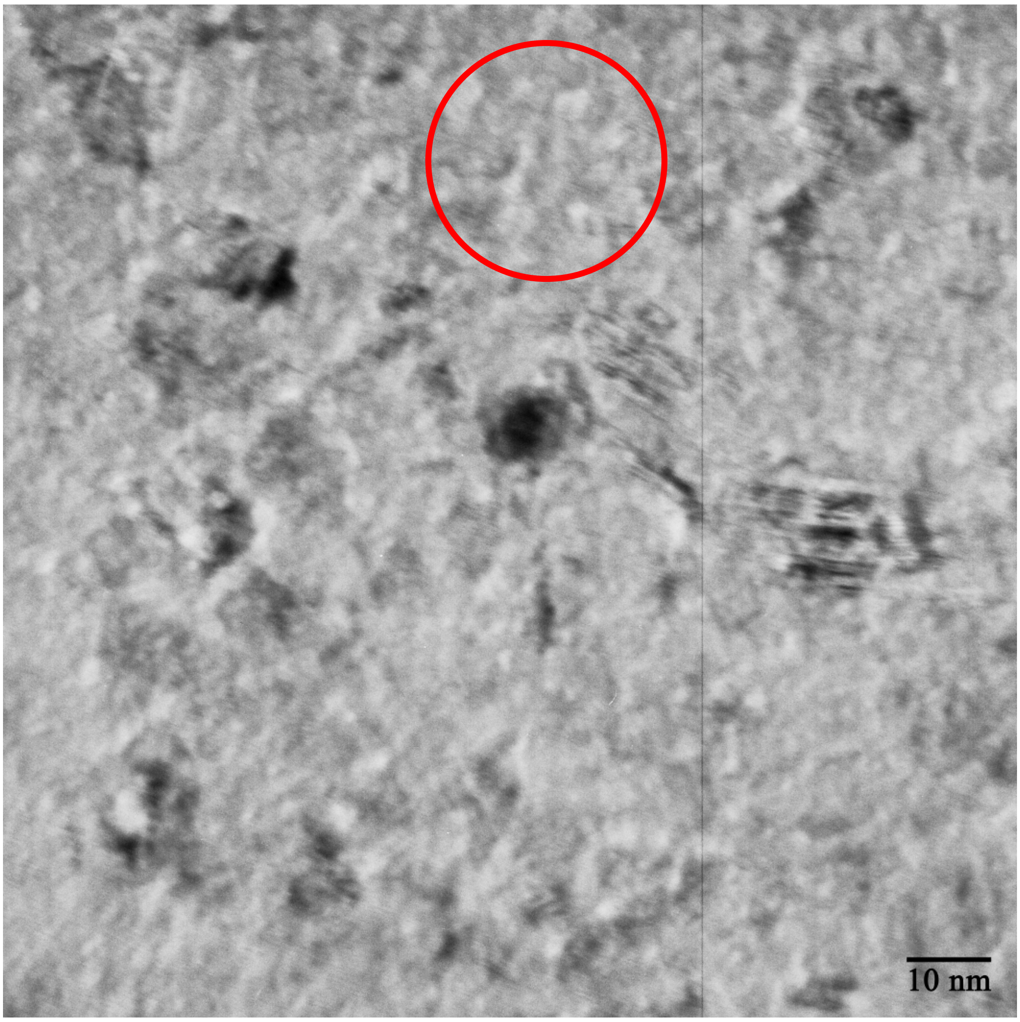

Figure 4-10 TEM plane-view high-magnitude bright-field image of 100-100. In the circle, the typical form indirectly postulated the Mg-Cu amorphous phases in nature.

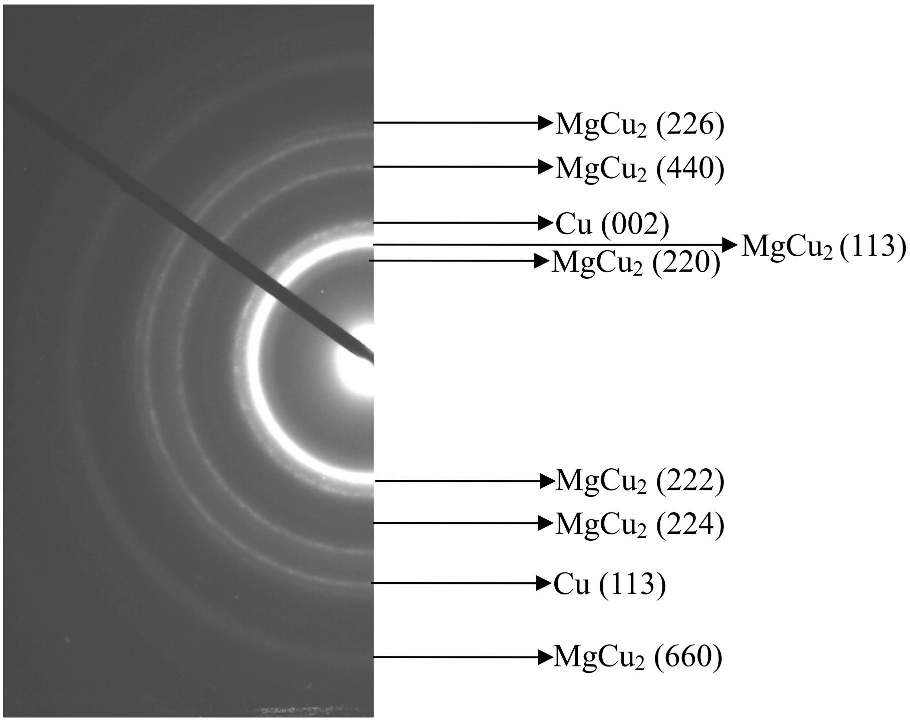

Figure 4-11 Selected area diffraction pattern of 100-100.

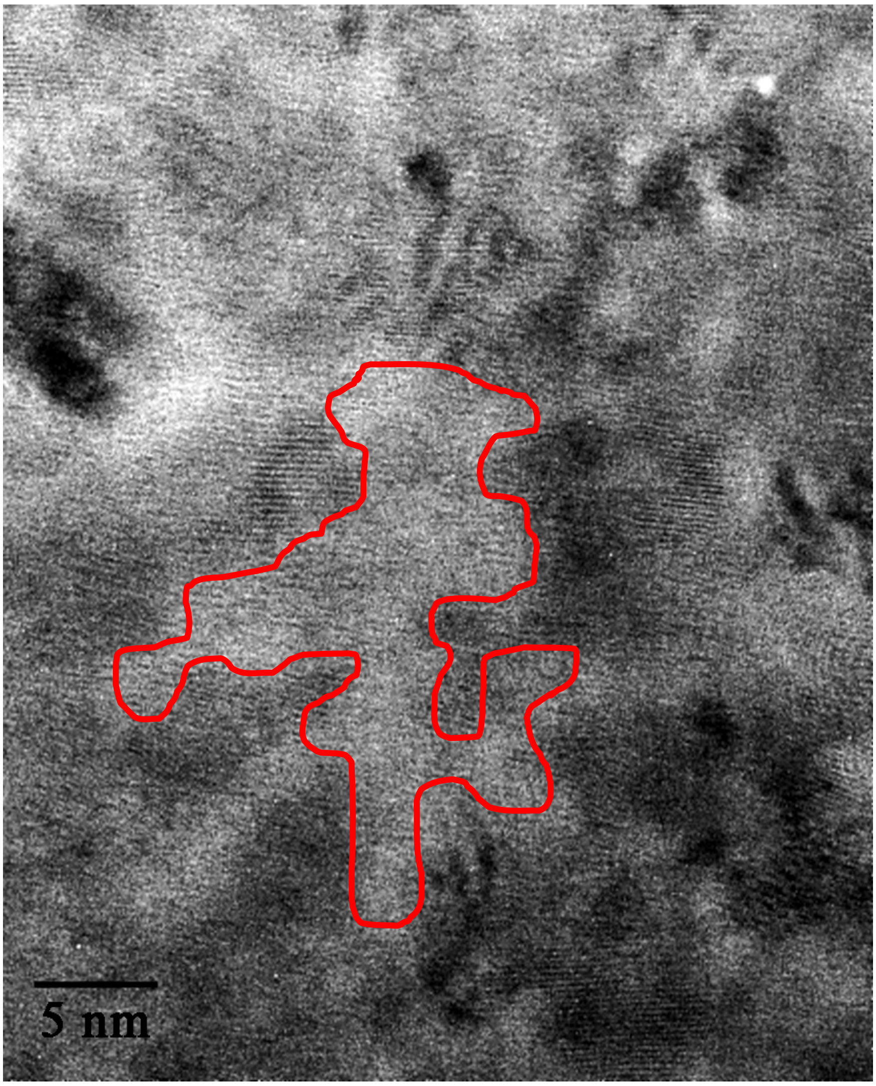

Figure 4-12 High-resolution TEM image of 100-100 with Mg-Cu amorphous/$MgCu_2$ $\{1\bar{1}0\}$ crystalline structure. The marked region is the Mg-Cu amorphous phase.

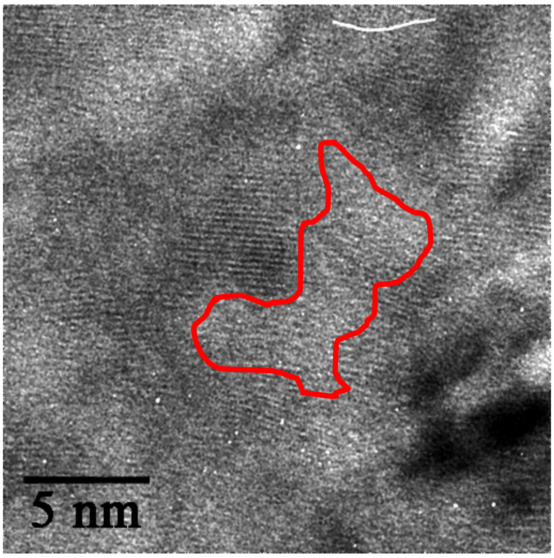

Figure 4-13 High-resolution TEM image of the 100-100 specimen. $MgCu_2$ particles in the $\{1\bar{1}0\}$ are around the Mg-Cu amorphous matrix in the marked region.

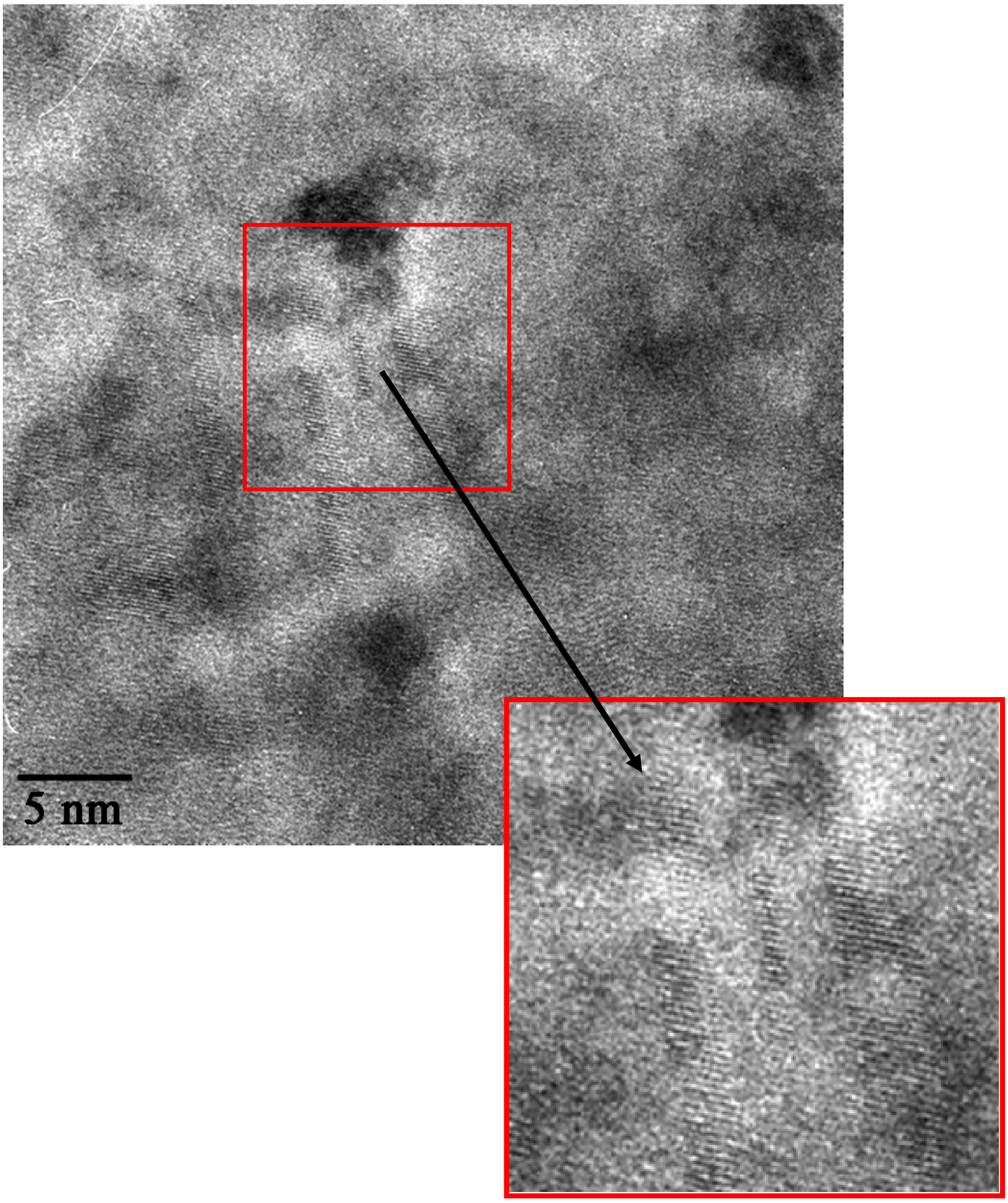

Figure 4-14 High-resolution TEM image of the structure of Mg-Cu amorphous/$MgCu_2$ in the $\{1\bar{1}0\}$ plane in the 100-100 specimen.

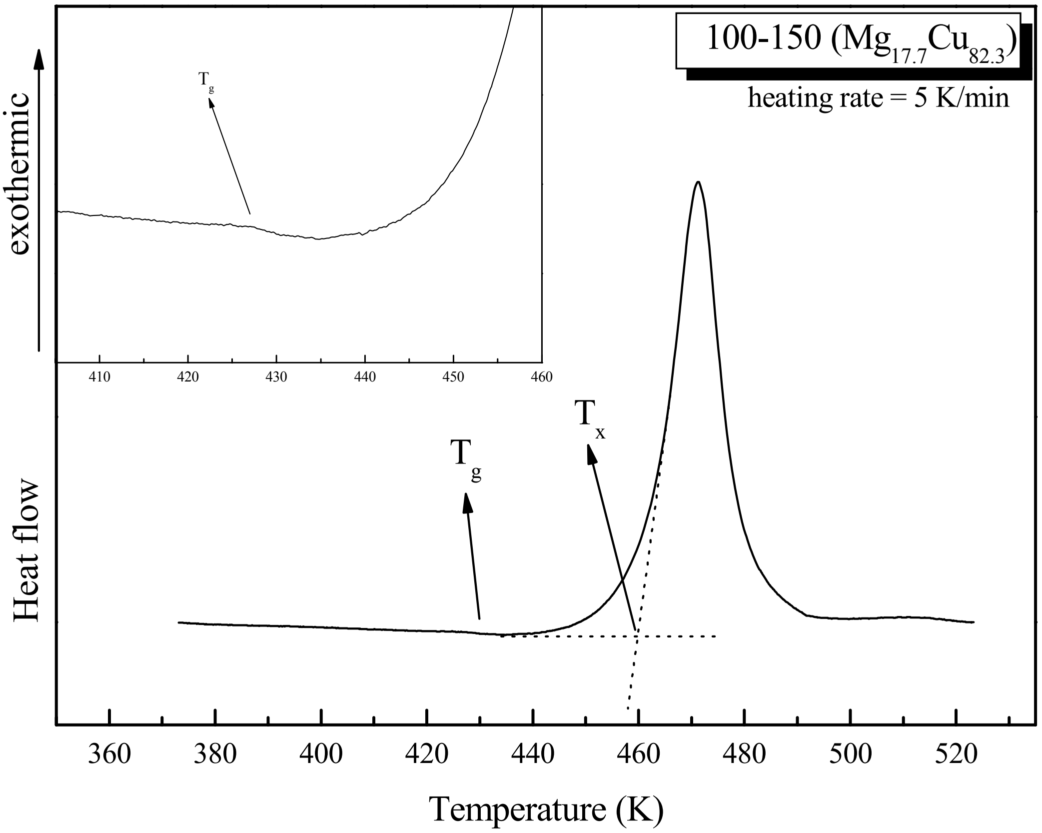

Figure 4-15 Modified non-isothermal DSC curve of 100-150.

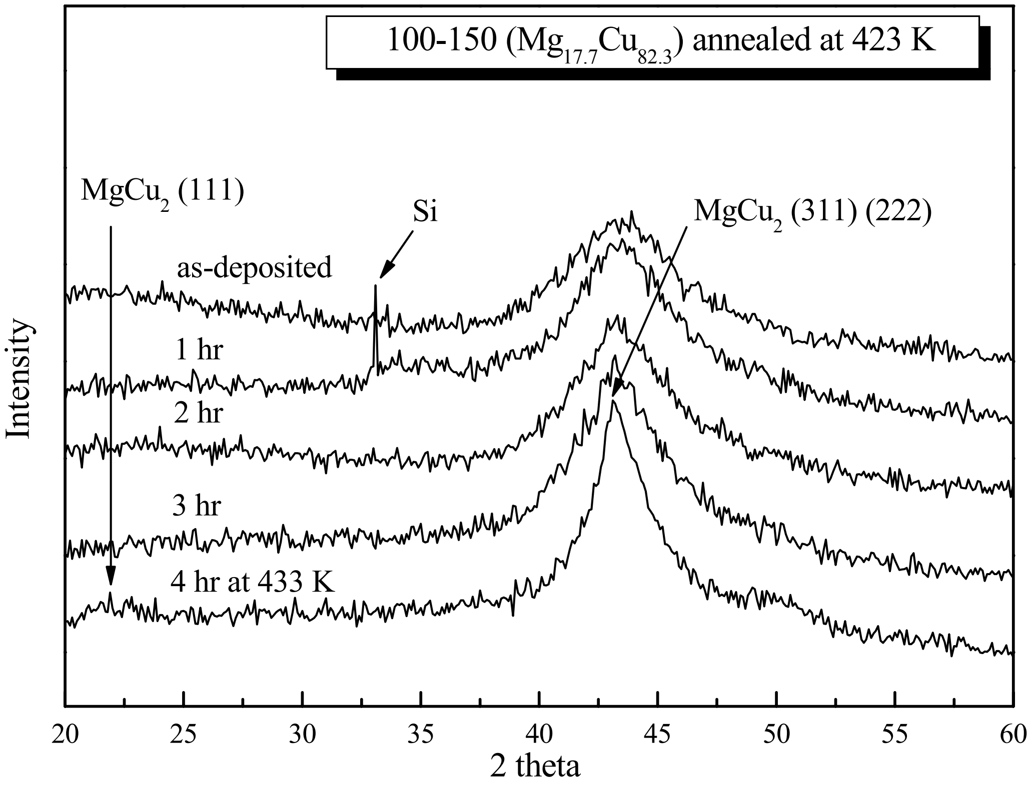

Figure 4-16 The structural transformation of 100-150 at 423 K.

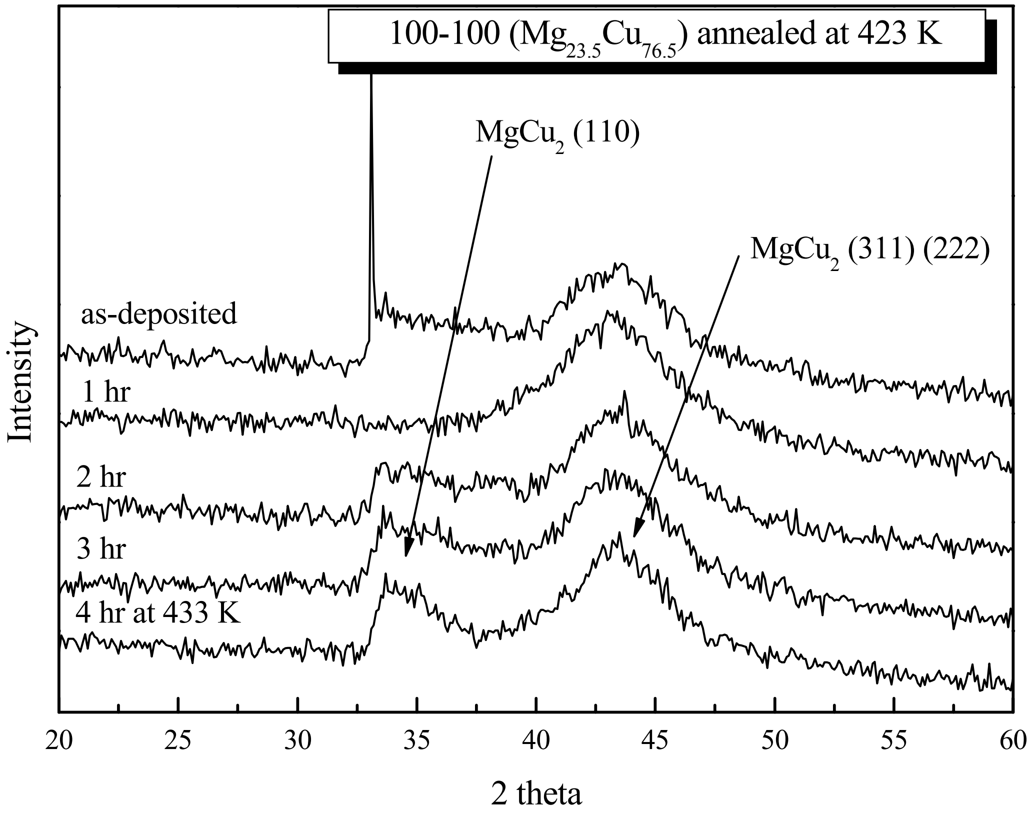

Figure 4-17 The structural transformation of 100-100 at 423 K.

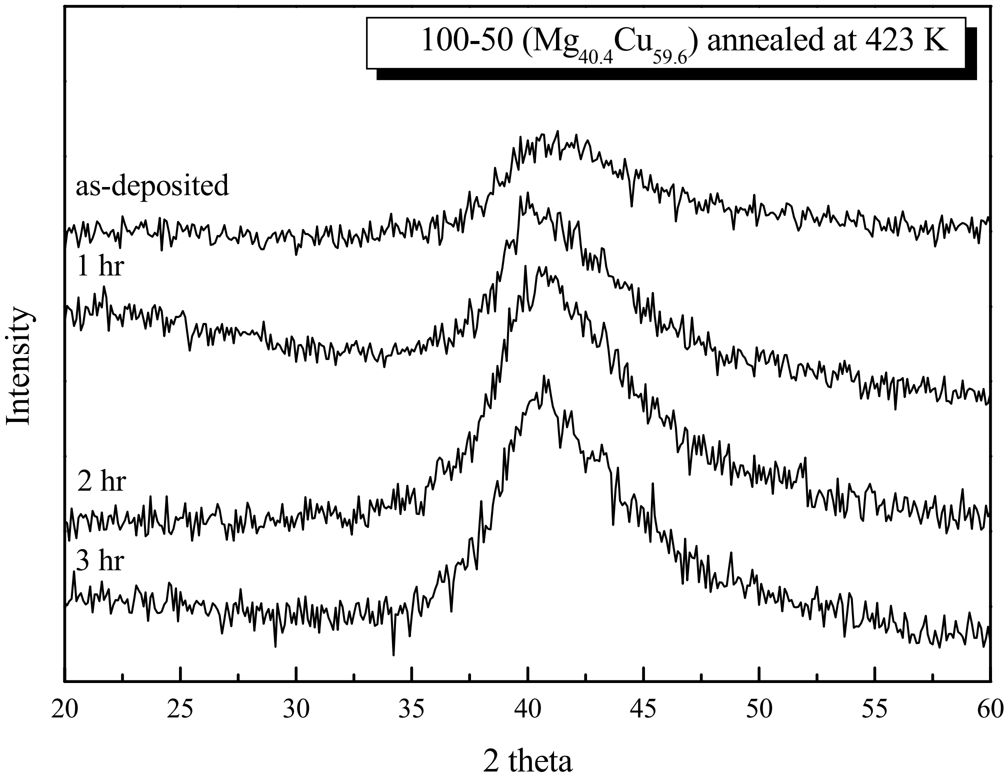

Figure 4-18 The structural transformation of 100-50 at 423 K.

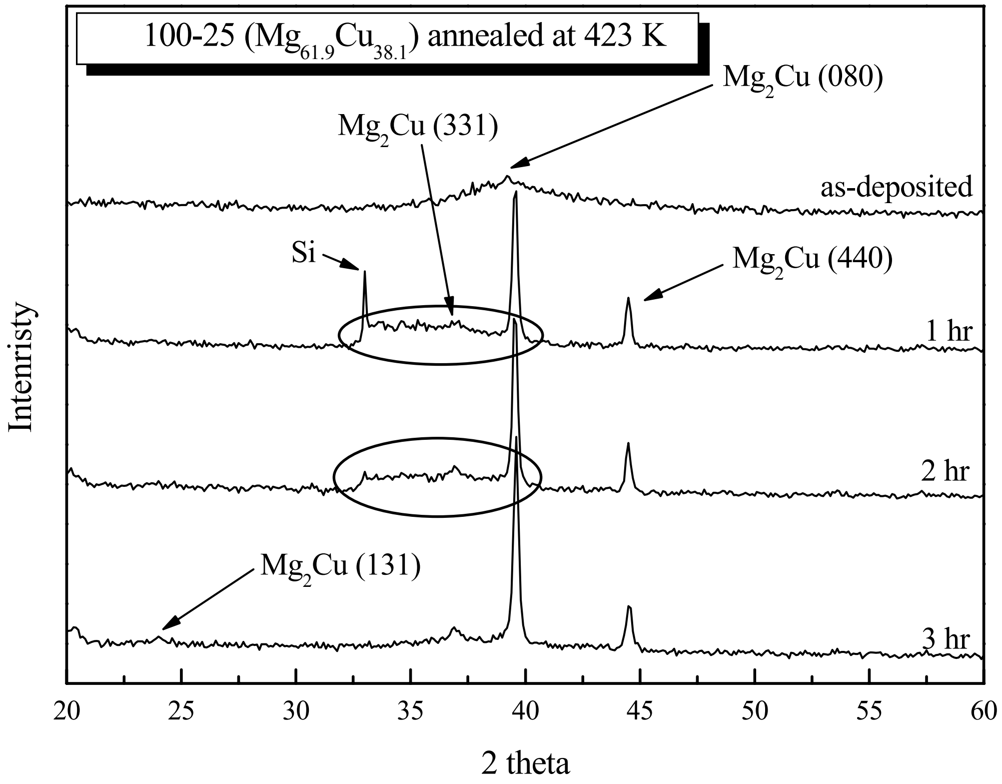

Figure 4-19 The structural transformation of 100-25 at 423 K.

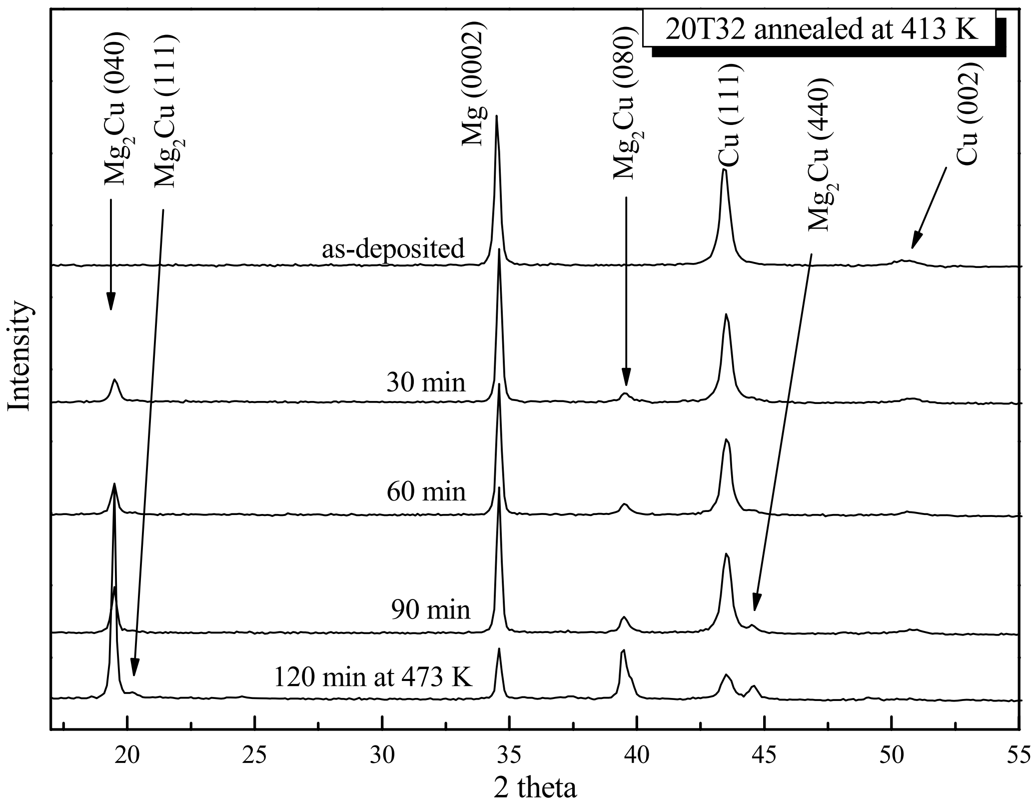

Figure 4-20 The structural transformation of 20T32 at 413 K.

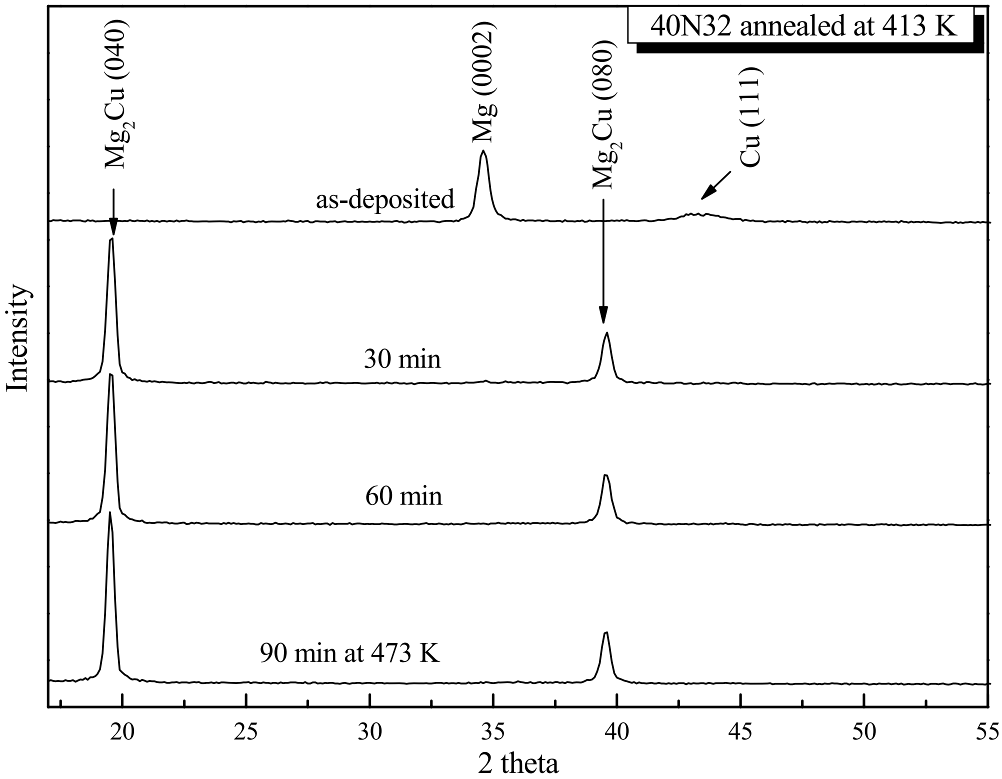

Figure 4-21 The structural transformation of 40N32 at 413 K.

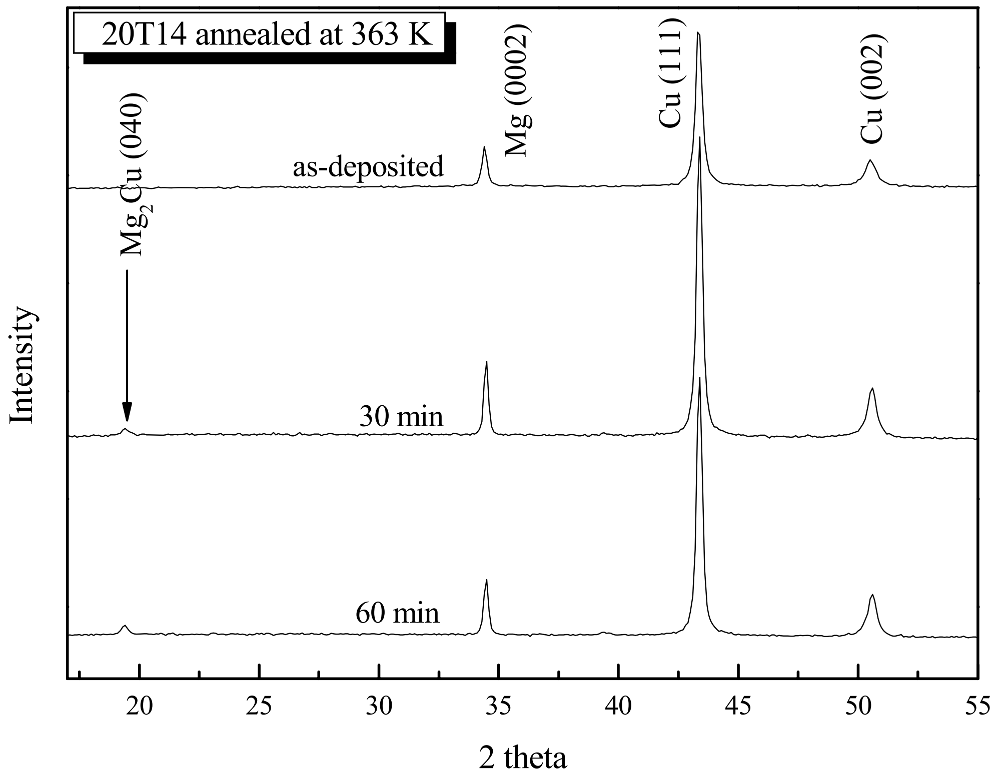

Figure 4-22 The structural transformation of 20T14 at 363 K.

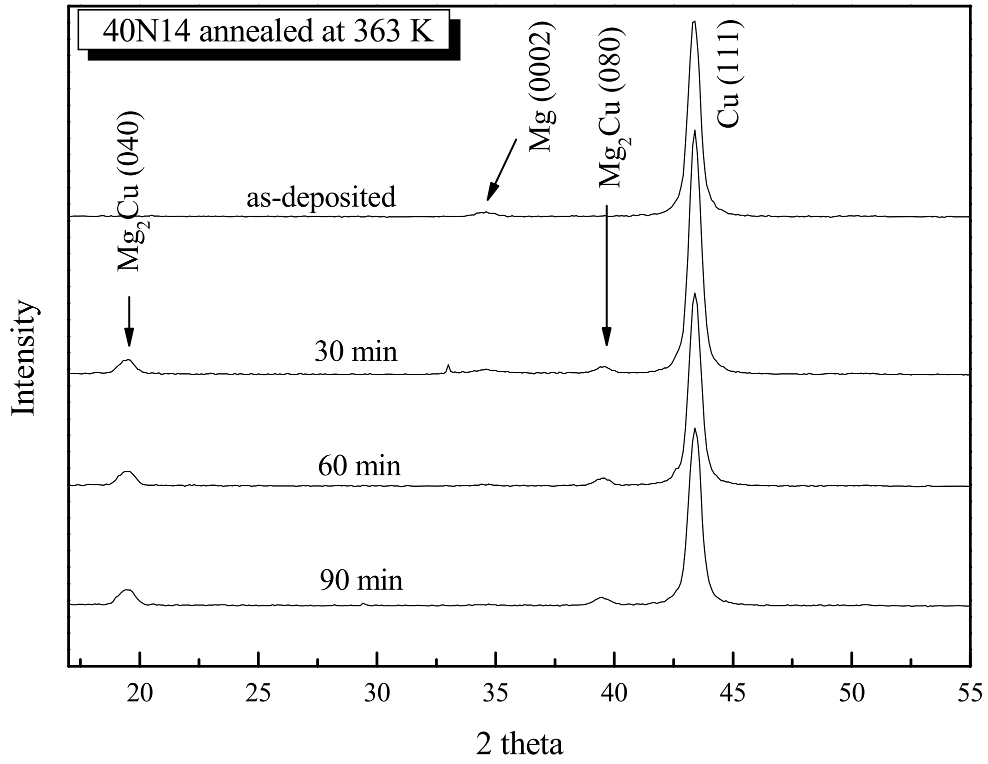

Figure 4-23 The structural transformation of 40N14 at 363 K.

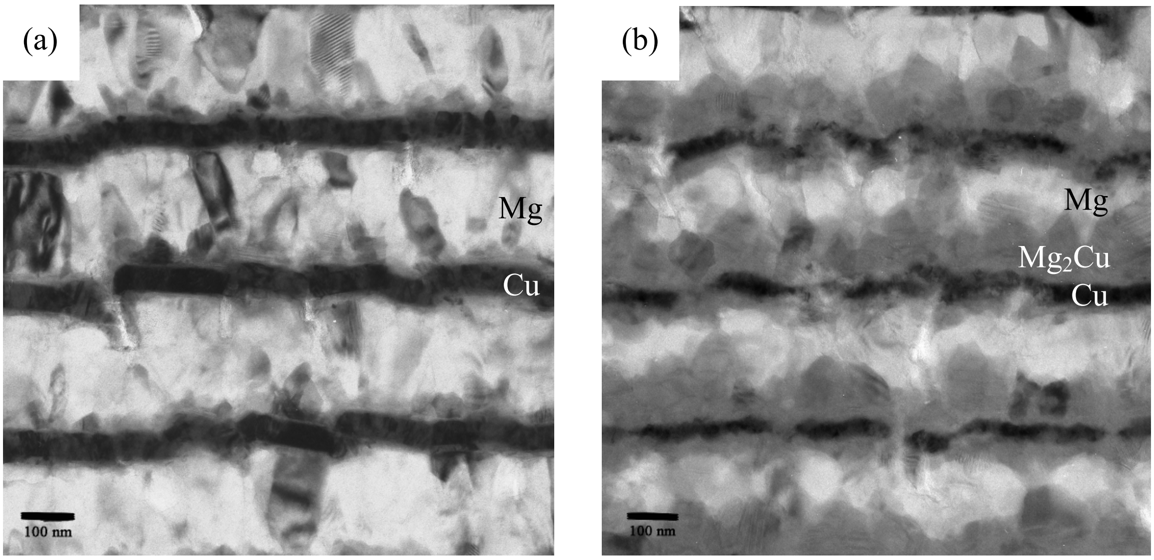

Figure 4-24 (a) TEM bright-field image of the as-deposited 20T32 film with nominally Mg 150-nm-thick and Cu 50-nm-thick individual layers. (b) TEM bright-field image of the 20T32 film annealed at 413 K for 2 hours.

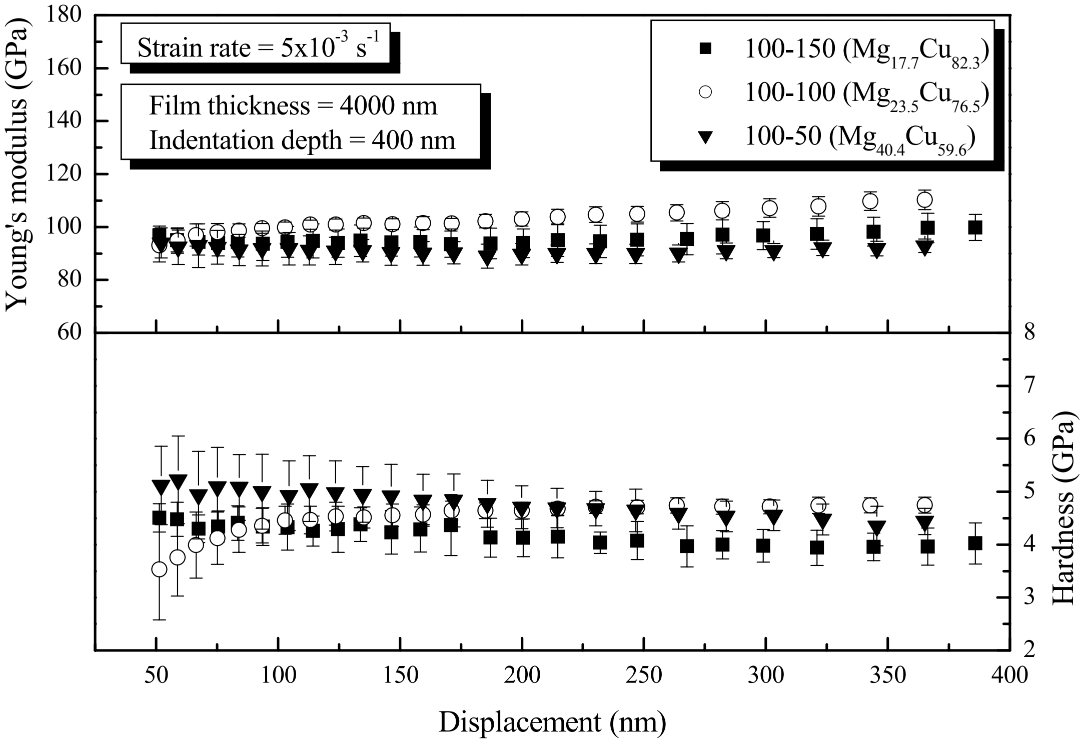

Figure 4-25 Modulus-displacement and hardness-displacement curves of 100-150, 100-100, and 100-50 at the strain rate of 5×10^{-3} s^{-1}.

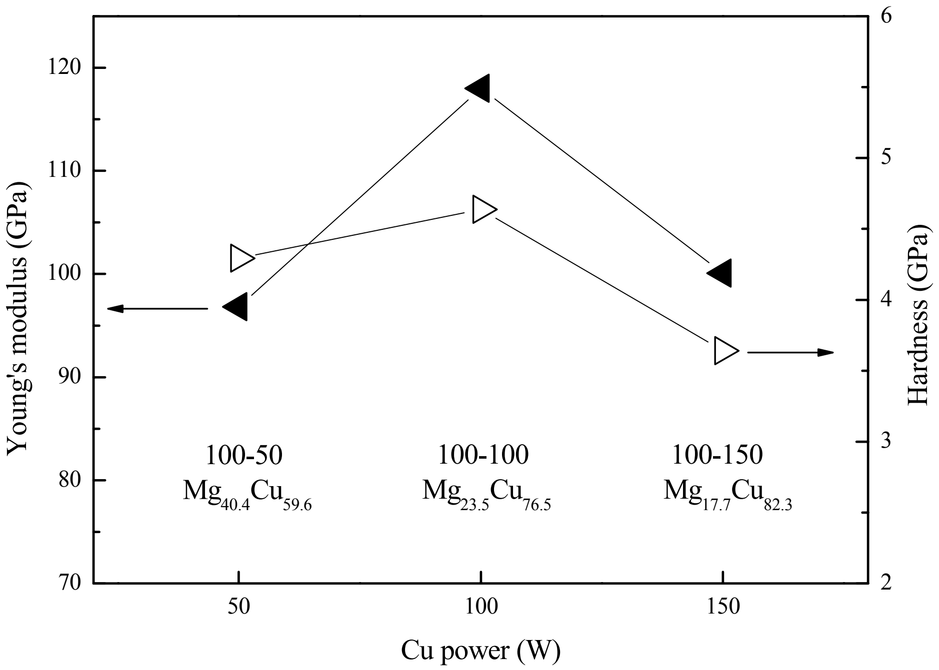

Figure 4-26 The compositional variation of Young's modulus and hardness from the unloading regions compared among 100-150, 100-100, and 100-50.

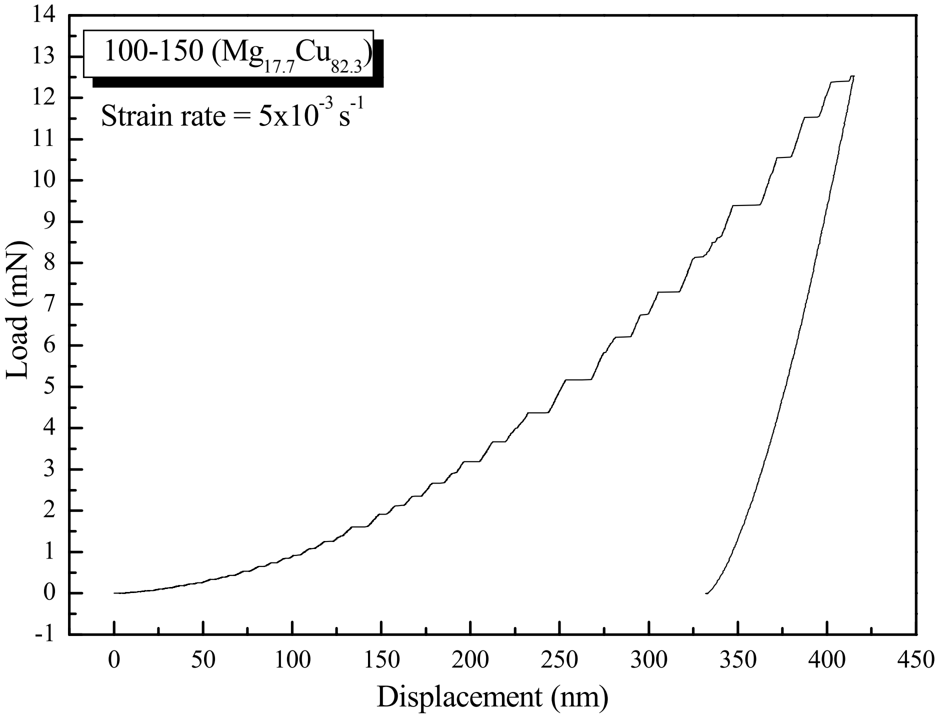

Figure 4-27 Load-displacement curve of 100-150.

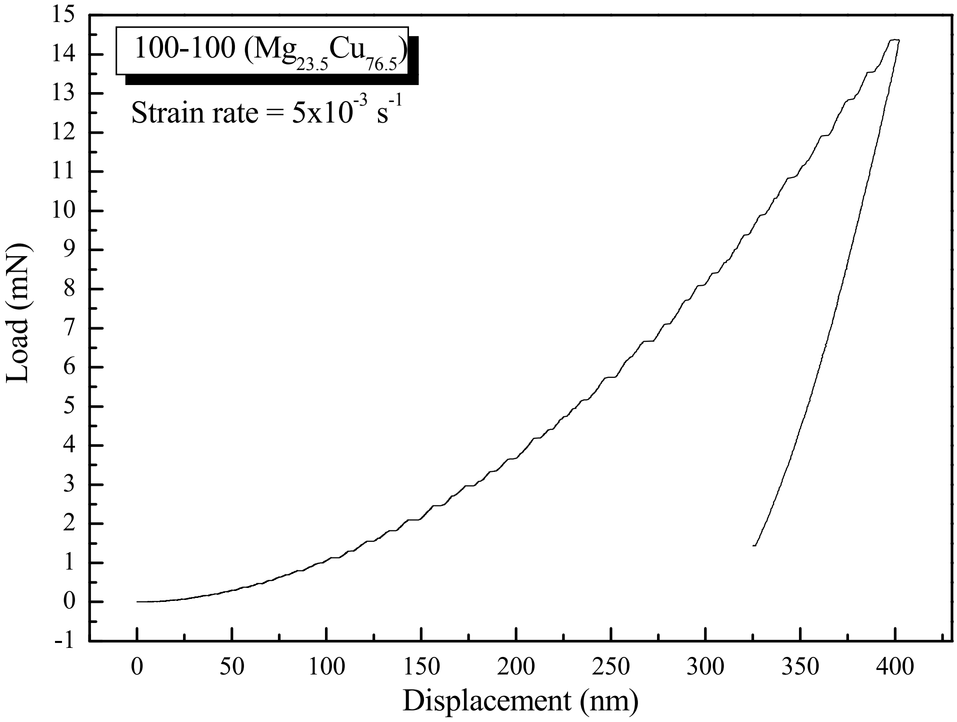

Figure 4-28 Load-displacement curve of 100-100.

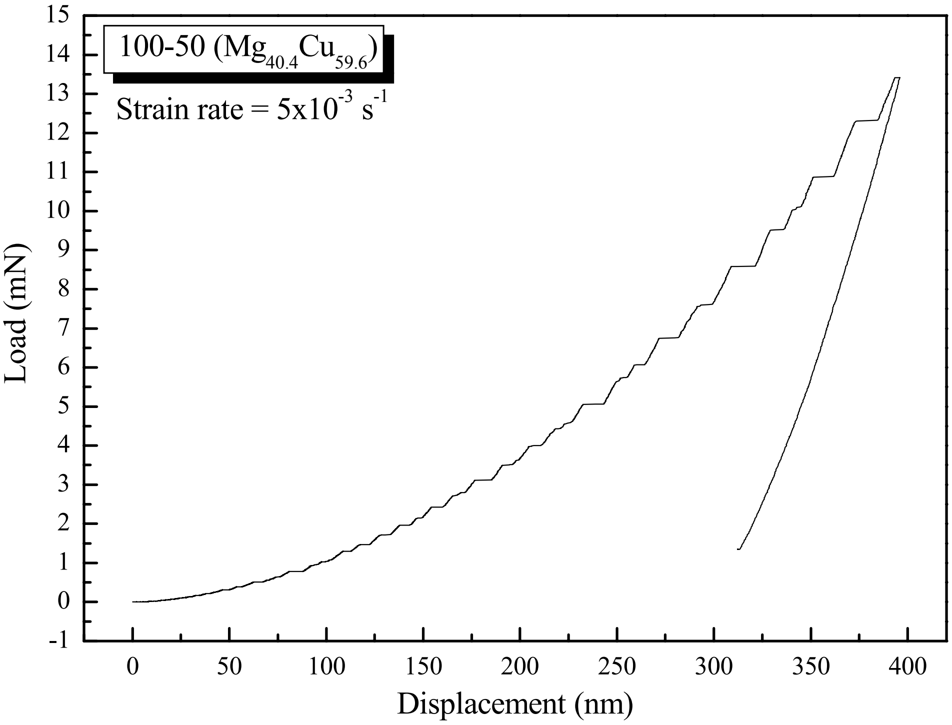

Figure 4-29 Load-displacement curve of 100-50.

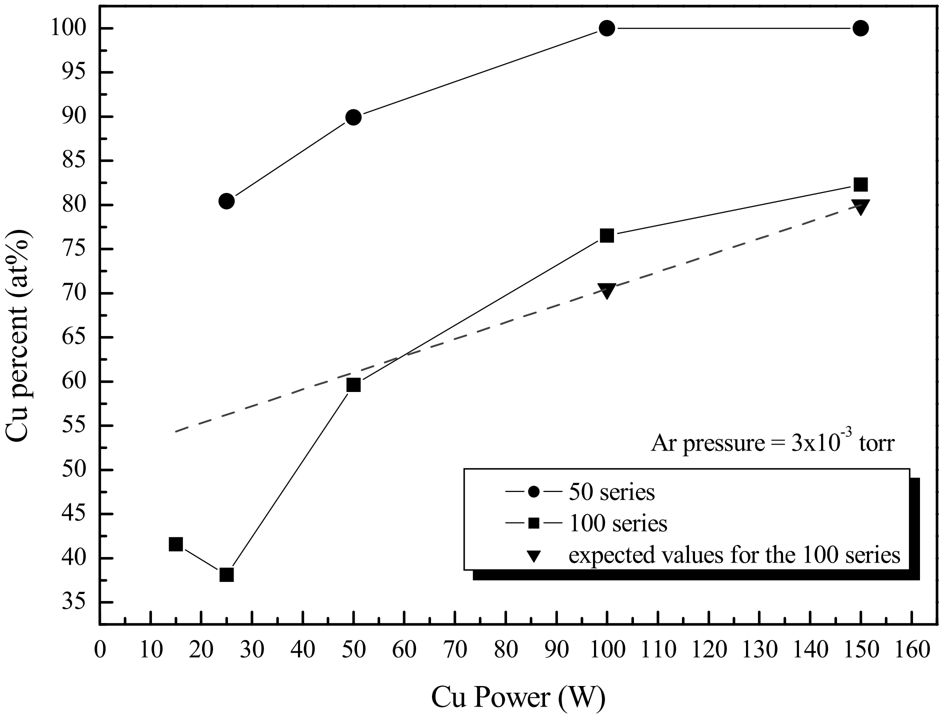

Figure 5-1 Cu content as a function with Cu power in the Mg-Cu co-sputtered films, where the 100 series means the Mg power is RF 100 W, and the 50 series means the Mg power is RF 50 W.

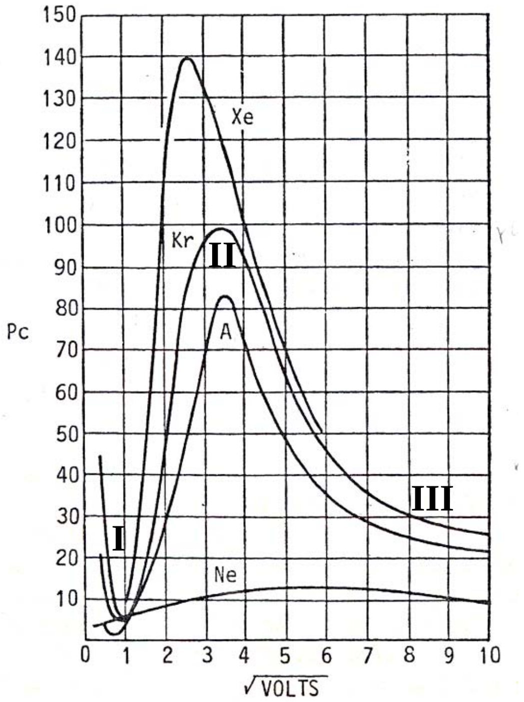

Figure 5-2 Probability of collision in Xe, Kr, Ar, and Ne [52].

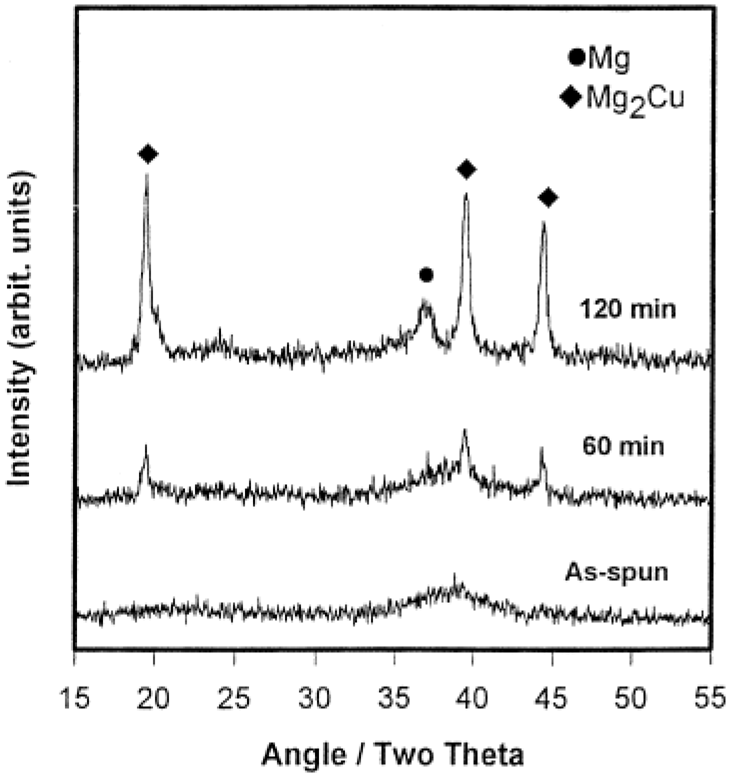

Figure 5-3 The structural transformation of $Mg_{79}Cu_{21}$ amorphous alloy annealed at 363 K [72].

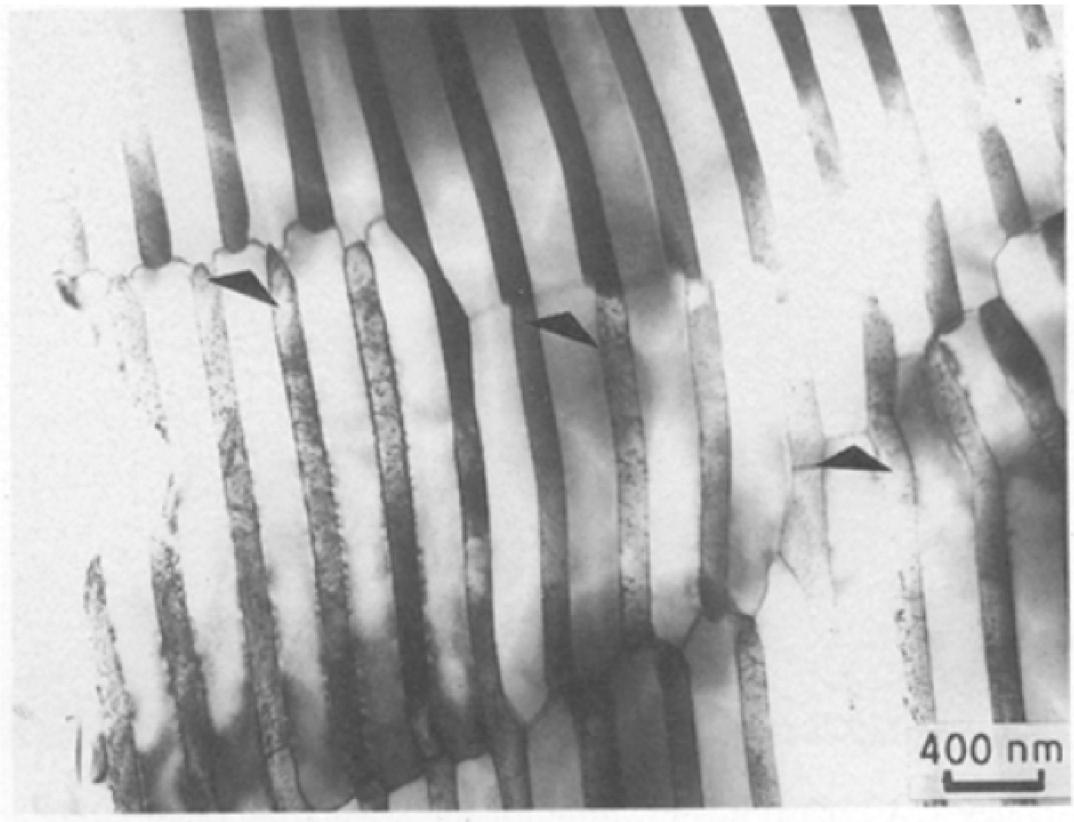

Figure 5-4 A transmission electron micrograph showing the lamellar structure in the eutectic Cu-$MgCu_2$ alloy, where white regions represent Cu crystalline phases, and black regions represent $MgCu_2$ crystalline phases [73].

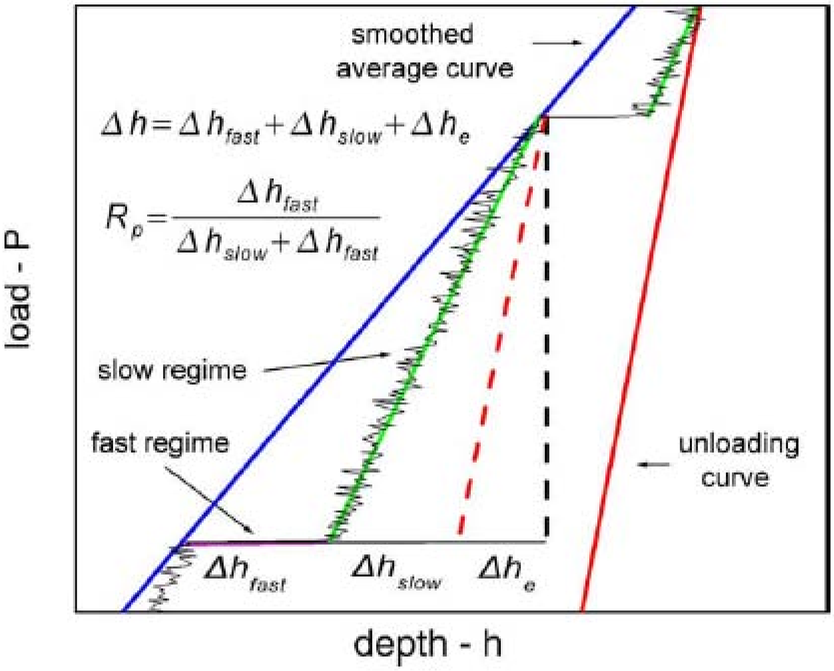

Figure 5-5 The indentation depth increasing from one step to the next is the sum of the elastic (Δh_e) and the slow (Δh_{slow}) and fast (Δh_{fast}) plastic deformations, which can be determined by the slopes of the smoothed average curve, the corrected unloading curve and the slow regime [74].

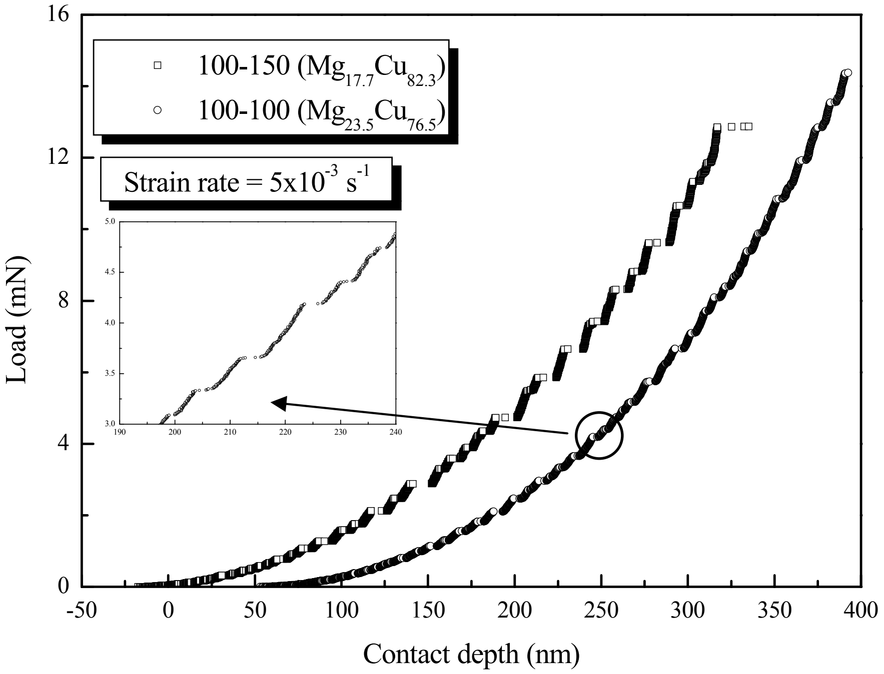

Figure 5-6 Load-contact depth curves of 100-150 and 100-100.